University of Southampton Research Repository

UNIVERSITY OF SOUTHAMPTON

FACULTY OF PHYSICAL SCIENCES AND ENGINEERING

Optoelectronics Research Centre

Novel Microbottle Resonators for Advanced Sensing Applications

by

Mohd Narizee Mohd Nasir

Thesis for the degree of Doctor of Philosophy

October 2016

UNIVERSITY OF SOUTHAMPTON

ABSTRACT

FACULTY OF PHYSICAL SCIENCES AND ENGINEERING

Optoelectronics Research Centre

Doctor of Philosophy

Thesis for the Doctor of Philosophy

NOVEL MICROBOTTLE RESONATORS FOR ADVANCED SENSING APPLICATIONS

Mohd Narizee Mohd Nasir

Optical microresonators supporting whispering-gallery modes (WGMs) have shown great potential towards miniaturization and applications in advanced optical microsystem by confining light to small volumes along with high-quality (Q). A new class of WGM microresonator, known as microbottle resonators (MBRs), have gained much interest in recent years because of their ability to confine light in a true 3D manner and to support WGMs through the smooth deformation of spheroids. Due to MBRs' broken mode degeneracies, strong overlap of different WGM families results in very dense and complex transmission spectra. A systematic study on the effects of microtaper fibre diameters on the spectral characteristics of WGM MBR is presented. Progressively cleaner and simpler spectra of the MBR were observed when the utilized microtaper waist diameter (D_t) was increased from 2 to 10 μm. The maximum transmission depth at resonance varied with different microtaper fibre utilized from ~20 dB $(D_t = 2\ \mu m)$ to ~4 dB $(D_t = 10\ \mu m)$. The loaded Q-factors observed to be unaffected by the increase in D_t with values of $> 10^6$ being measured in all cases. Mode transformation of MBR was also experimentally investigated and compared to a microdisc FDTD simulation by studying near-field images of the output beam at the waist of the tapered fibres. For the first time, experimental observation of mode transformation from LP_{01} to LP_{11} across scanned WGM resonances is reported.

Spectral simplification of MBRs' WGMs was demonstrated by introducing scatterers on the surface of the resonators. Through focused ion-beam (FIB) milling, periodic micro-scars were inscribed along two MBRs' axial and azimuthal paths. High Q-factor value of $> 10^5$

were observed in the MBRs before and after the inscription process. Utilizing a highly discriminating polarization-resolved set-up, MBRs' excited TE- and TM-WGMs were accurately distinguished with clear free-spectral ranges (FSRs) designation. Microtaper excitation arrangement near the MBRs' bottle-neck with TE-polarized input light yielded a single sharp and distinguishable WGM resonance (~ 18 dB and ~ 8 dB) over a broad wavelength range. FDTD simulation performed on a microdisc indicated that two or more WGMs are able to beat together to circumvent the defects introduced by the micro-scars and a maintain strong WGM confinement near the resonator surface.

Since excitation of WGMs microresonators (MRs) is polarization sensitive, the polarization state of the evanescently launched light affects the number, type and strength of each resonance. To understand the MRs performance under TE/TM launching conditions by means of microtaper fibre evanescent coupling, a polarimetric set-up was designed to study the transmission, polarization-cross coupling (PXC) and scattering of a WGM microsphere, milled-MR, microcylinder and scarred-MBR. Experimental results showed that the transmission dip and PXC minima are shifted with respect to the ideally expected input polarization angle. A theoretical model based on Jones matrix attributed the observed shift to residual birefringence of the output part of the tapered fibre. The model demonstrated that the scattered light is not affected by this residual birefringence and therefore is a better metric to ensure precise TE or TM polarization launching. It was also observed that MRs with tighter axial power confinement (milled-MR and scarred-MBR) showed larger cross-polarization coupling efficiencies and are MRs of choice to be utilized as polarization converters. In addition, it is shown that utilizing the TE WGM resonances results in superior cross-polarization performance.

Demonstration of a hybrid plasmonics-MBR with high-*Q* was presented for surface plasmon sensing applications. To excite surface plasmon polaritons (SPPs), a thin gold-metal-film was deposited on the surface of the MBR. The surface curvature of the MBR resulted in deposition of the thin metal-film to half of the resonator surface with a meniscus profile. The meniscus thin metal-film profile created appropriately tapered edges on the two sides of the MBR that facilitated a low-loss adiabatic transformation of the MBR's WGMs to SPPs, and vice versa. Calculated *Q*-factors of the plasmonics TM transmission dips were in the range of 850. Accurate Lorentzian fitting performed on the measured data revealed that each dip is actually a composite resonance comprising three partially overlapping WGMs with high *Q*-factor values in excess of 2500. The excitation strength of the three overlapping resonances varies with the microtaper coupling arrangement relative to the position of the meniscus thin metal-film. In some cases, the generation of a single plasmonic resonance with high excitation strength is demonstrated while supressing the other resonances of the same family group-mode. FDTD simulations performed on a WGM microdisc with a thin metal-gold-film of meniscus profile showed good agreement with the plasmonics-MBR experimental observations. The simulated steady state distribution of the magnetic **H**-field also revealed that plasmonics radiation into air is strongest near the starting-edge of the meniscus thin-metal film, making it the region of interest for surface plasmon sensing.

The performance of MBRs as highly tuneable WGM sources and strain-sensing devices is presented. The *solid* MBRs under study were fabricated by slightly overlapping two SMFs during arc-fusion-splicing. The simplification of the dense MBR-WGMs spectral feature was achieved by evanescently coupling light on the up-taper region of an optical tapered fibre while retaining its *Q*-factor value of $> 10^5$. TE- and TM-WGM resonance shifts corresponding to applied mechanical strains were investigated with the utilization of a highly discriminating polarization-resolved set-up. The TM-resonance shift of the MBR showed a record tunability of an entire FSR (~ 4.1 nm), the highest ever demonstrated by a *solid* WGM optical microresonator, with a TM-/TE-WGM resonance shift ratio of 1.67.

Table of Contents

List of Figures

DECLARATION OF AUTHORSHIP

I, Mohd Narizee Mohd Nasir, declare that this thesis, entitled "*Novel Microbottle Resonators for Advanced Sensing Applications,*" and the work presented in it are my own and has been generated by me as the result of my own original research.

I confirm that:

1. This work was done wholly or mainly while in candidature for a research degree at this University;
2. Where any part of this thesis has previously been submitted for a degree or any other qualification at this University or any other institution, this has been clearly stated;
3. Where I have consulted the published work of others, this is always clearly attributed;
4. Where I have quoted from the work of others, the source is always given. With the exception of such quotations, this thesis is entirely my own work;
5. I have acknowledged all main sources of help;
6. Where the thesis is based on work done by myself jointly with others, I have made clear exactly what was done by others and what I have contributed myself;
7. Parts of this work have been published as: [please see list of publications].

Signed: ....

Date: ....

Acknowledgements

بسم الله الرحمن الرحيم

This thesis and all of its work would not have been possible without the kind assistance and support of the organizations and people around me. My deepest and sincere gratitude goes towards my main supervisor, Professor Michalis N. Zervas, for his support and encouragements throughout the course of my work. It has been a real privilege to work under his guidance here in the Optoelectronics Research Centre. I would also like to express my deep gratitude to my second supervisor, Dr. Senthil G. Murugan, for all of his help and tips with my experimental laboratory works. His works in optical microresonators have been a real inspiration to me.

I would like to show deep appreciation to my colleague, Mr. Shahab B. Gorajoobi, for his plentiful of help in my FDTD modelling work, MATLAB programming, and also for providing me with his fabricated microresonators to study in some part of my research. I would also like to thank Dr. Ming Ding who had helped me in the early parts of my research by providing me the required microtaper fibres, and also with her help in inscribing micro-scars by FIB-milling in the cleanroom.

I would also like to express my gratitude to Professor James S. Wilkinson for all of the fruitful discussion during the group meetings. His earnest in my work opened up plenty of new research opportunities.

I would also like to extend my thanks towards my group members, Dr. Jonathan Butement, Vinita Mittal, Amy Tong, Dr. Dave Rowe, Dr. Ping Hua, Dr. Alina Karabchevsky, Neil Session, Zilong Wang, and of course, Dr. Armen Aghajani, for keeping the work in the labs a real fun and of great experience.

The financial support from Malaysia government body of Majlis Amanah Rakyat (MARA) is gratefully acknowledged towards the course of my Ph.D.

And finally, I would like to thank my parents and the rest of my family for their love and tremendous support not only during my life as a postgraduate student here in the University of Southampton, but also my life entirely. Thank you.

Nomenclature

WGM	Whispering gallery mode
MR	Microresonator
MBR	Microbottle resonator
FSR	Free spectral range
Q	Quality
D_t	Microtaper waist diameter
2D	Two dimensions
3D	Three dimensions
Cw	Continuous wave
DFB	Distributed feed-back
C-QED	Cavity quantum electro-dynamics
FWHM	Full width at half maximum
FIB	Focused ion-beam
LP	Linearly polarized
SMF	Single mode fibre
CCD	Charged-coupled device
TLS	Tuneable laser source
MMF	Multi-mode fibre
FDTD	Finite-difference time-domain
SEM	Scanning electron microscope
TE	Transverse electric
TM	Transverse magnetic
SP	Surface plasmon
SPP	Surface plasmon polariton
ND	Neutral density

List of symbols

n, m, l	Sphere mode numbers
m, p, q	Bottle mode numbers
$\psi_r(r)$	Sphere field in the radial direction
$\psi_\phi(\phi)$	Sphere field in the azimuthal direction
$\psi_\theta(\theta)$	Sphere field in the angular direction
N_s	Normalization constant of sphere volume integral
$j_n(x)$	Spherical Bessel function of x of order n
$J_n(x)$	Bessel function of x of order n
$H_N(x)$	Hermite polynomial of x of order N
k	Wavenumber
n_s	Refractive index of sphere
n_0	Refractive index of outside medium
α_s	Decay constant of the field in the sphere
β_l	Propagation constant parallel to the surface of the sphere
κ	Coupling factor
β_f	Tapered optical fibre mode propagation constant
β_m	Microsphere mode propagation consant
n_f	Tapered optical fibre core index
n_{cl}	Tapered optical fibre cladding index
n_{eff}	Effective refractive index of light propagating in a channel waveguide
(z, ρ, φ)	Cylindrical coordinates
E	Electric field
H	Magnetic field
$\|a_1\|^2$	Total power circulating in a resonator
$\|b_1\|^2$	Transmission in a waveguide past resonator coupling point
ω_0	Optical frequency
c	Speed of light
$\Delta\nu_q$	MBR axial free spectral range
$\Delta\nu_m$	MBR azimuthal free spectral range
$\mathcal{F}$	Finesse
V_{mode}	Mode volume of microsphere
V_Q	Integration volume for microsphere
$\epsilon(\vec{r})$	Dielectric material constant at $\vec{r}$
$V_{m,q}$	Mode volume of MBR
$I_{m,q}/I_{m,q}^{max}$	Normalized intensity distribution of MBR

In loving memory of Mohd Nasir Mohd Nor

Chapter 1: Introduction

1.1 Optical whispering-gallery mode microcavities

Whispering gallery modes (WGMs) were initially explained by Lord Rayleigh in the form of *acoustical* waves based on the phenomenon observed in St. Paul's cathedral in London [1,2]. The smooth curved gallery of the cathedral's dome (with radius R) permits the reflection of sound waves (with resonance wavelength λ_{res}) on its surface with an integer fraction m of the circumference: $\lambda_{res} \cdot m = 2\pi R$. Prior to the application of WGMs in electromagnetic waves, optical microcavities which confine light by repeated reflection for a long period of time took the form of either linear-cavities, such as VSCEL, DFB and Fabry-Pérot [3-5], or circular-cavities as in an all fibre ring structure [6]. The resonator's light confining properties are determined by its mode volume *V* and quality factor *Q*. A great number of optical microcavities applying the principles of WGMs have been demonstrated since the concept was transferred into the electromagnetic waves domain by Richtmyer in order to achieve high *Q/V* ratio [7]. Pioneering work on optical WGMs was demonstrated by utilizing a spherical Sm:CF_2 structure and coupling it to a free-space maser [8]. *High-quality* (*Q*) resonators with *Q*s in the range of 10^8 – 10^9 were later demonstrated by melting fibre tips of fused silica (SiO_2) in order to produce optical WGM microspheres of high purity and uniformity [9,10]. The simplest form of optical WGM resonators are cylinders, which can be made by stripping-off the polymer coating of conventional single-mode fibres (SMFs) [11]. However, due to their longitudinal degree of freedom, they suffer from high-loss and low-*Q*s as the coupled light into the resonator's WGMs spreads along the cylinder and leak out. A significant performance improvement has been demonstrated with the introduction of microdisk/microtoroid WGM resonators. Since high surface roughness would induce scattering losses and limit a microresonator *Q*-factor, laser reflow was implemented in the fabrication of microtoroids to ensure smooth surface yielding *Q* of up to 10^8 [12]. Additionally, the geometrical shape of microdisk/microtoroid resonators has made them the most suitable candidates for on-chip integration [13]. Recently, the fabrication of WGM microdiscus resonators by "squashing" microspheres under high temperature conditions has been reported with *Q* in the range of 10^5 [14].

A new class of optical WGM microresonators which has gained much interest in recent years is represented by the microbottle resonators (MBRs). The concept of MBRs primarily relies on the survival of WGMs through smooth deformation of spheroids. While most of the WGM microresonators mentioned earlier trap light by 2D confinement along their circumference, MBRs are able to support true 3D light confinement through the combination of WG-ring and WG-bouncing-ball principles [15]. Strong light field enhancements associated with two distinctive MBR turning points define the area of WGM modal confinement [16]. As such, MBRs sustain non-degenerate WGMs with a free-spectral range (FSR) a magnitude-order smaller than microspheres with the same diameter [17]. The dense WGM generation is easily accessible since a variation of the MBR radius even at the nanoscale is capable to trap light close to its surface [18]. The initial MBR fabrication method involved “heat-and-pull” process on two-sections of a microtaper with homogenous diameter in order to produce a bulge on the fibre [19-21]. The fabrication of MBRs was later simplified and improved with the thermo-mechanical process of “soften-and-compress” where a section of a standard optical fibre is heated and compressed in order to create a pronounced bulge with parabolic profile [17]. The intrinsic *Q*-factors of MBRs were calculated to be in the range of 10^8 [22] with experimental values of 10^7 being successfully demonstrated [23].

1.2 Motivations and key achievements

Optical WGM microresonators are able to confine light to small volumes and long period of time by means of resonant circulation. Additionally, distinctive WGM spectral properties (i.e. high stability/consistency, tunability, narrow linewidth) held by WG-resonators are of great potential for various applications. To name a few, optical WGM cavities have found their way in cavity-QED studies, optical filters, bio/chemical/environmental/mechanical sensing, micro-lasers, and plasmonic devices [24-26]. Through unique light confinement, WGM MBRs supporting high *Q*-factors have attracted increasing attention towards advanced optical device/system/network applications. Among others, they were used as a highly tuneable optical device [22], a microfluidic sensor [23], an optical sensor [27], a fibre add-drop filter [28], an optical nonlinear source [29] and also a plasmonic device [30]. Nonetheless, with the never ending demand and expectations for even more advanced photonic/optoelectronic technologies, there is plenty of space to be explored on WGM MBRs for future applications.

Key achievements of this thesis are as follows:

1. As MBRs attain non-degenerate WGMs, they would give rise to dense and complex spectral transmitted features. Two methods are demonstrated in this thesis for cleaner and simpler MBR WGMs spectra. The first manipulates the MBR’s excitation source (tapered fibre) to decrease the number of excited WGMs. For the first time, a mode transformation from LP_{01} to LP_{11} across scanned WGM is also presented. The second method involves direct writing on the surface of the MBR in order to attenuate some of the excited modes while maintaining the MBR’s high *Q*-factor.

2. Since optical WGM microresonators are polarization sensitive, a polarization-resolved set-up utilizing a normal microtaper is presented. The evolution of WGM transmission dips,

polarization cross-coupling peaks and scattered light was studied in detail as the input polarization was changed. The study is greatly beneficial for polarization sensitive device applications utilizing optical WGM microresonators.

3. A hybrid WGM plasmonics-MBR is demonstrated where a varying thin metal-film thickness facilitates a low-loss adiabatic transformation of the MBR-WGMs to surface plasmon polaritons (SPPs), and vice versa. The excitation strength of individual WGM-plasmonic resonances within a family group-mode could be controlled to a certain degree with different tapered fibre coupling arrangements, relative to the position of the meniscus thin metal-gold-film. The hybrid resonator is beneficial towards a high-*Q* SPP device.
4. Broadly tuneable *solid* MBRs with high *Q*-factors are presented by applying mechanical strain. A WGM resonance shift over an entire FSR is demonstrated in a single monolithic optical resonator design, suitable to be implemented as a WGM resonance tuning source and to be utilized in optical strain-sensing.

1.3 Thesis outline

Chapter 2 presents the basics of optical microcavities and WGMs. The governing factors in an optical microresonator coupling strength and its corresponding *Q*-factor are explored. Modes and fields of WGM microsphere, MBRs and tapered fibres are presented and parameters which influence coupling efficiency between a waveguide (tapered fibre) and a WGM resonator are determined. Main properties of optical microcavities which are relevant to WGM microspheres and MBRs are also presented.

Chapter 3 presents a systematic study of the effects of the microtaper excitation fibre diameter (D_t) on the MBR transmission spectrum. Mode transformation as a result of light coupling from MBR back to microtaper fibre is reported and for the first time, the conversion of microtaper LP_{01} mode to LP_{11} is shown experimentally and compared to numerical FDTD simulations of a planar waveguide/disc-resonator system.

Chapter 4 demonstrates a precise and controllable method to simplify the dense MBR WGM resonance spectra through the inscription of periodic micro-scars on the MBR surface by means of focused ion beam milling. High *Q*-factors in access of 10^5 are preserved by the MBRs even after the milling process. By utilizing a highly discriminating polarization resolved set-up, a distinguishable WGM resonance peak is observed over a broad wavelength with TE input polarized light and excitation arrangement near the MBR bottle neck. FDTD simulation performed on a microdisc show that selected WGMs can beat together to circumvent the defect introduced by the micro-scars.

Chapter 5 presents the study of polarization effects on four different types of WGM microresonators by utilizing a polarimetric set-up. The evolution of WG transmission dips, polarization cross-coupling peaks and scattered light are studied in detail by changing the input light polarization state. Transmission dips and polarization cross-coupling minima are shifted in the experimental results with respect to what is ideally expected at that input polarization angle. A theoretical model based on Jones matrix attributes the observed shifts to the residual birefringence of the output part of the micro-taper fibre, used for evanescent coupling into the microresonators.

Chapter 6 demonstrates a hybrid WGM plasmonics-MBR with varying thin metal-film thickness. The calculated composite WGMs *Q*-factors of dielectric-TE and plasmonics-TM transmission dips are in the range of 2100 and 850, respectively, with higher *Qs* of individual overlapping resonances. The excitation strength of each MBR individual resonance mode varies with position of the tapered fibre with respect to the meniscus thin metal-gold-film. FDTD simulations performed on a hybrid microdisc show a similar trend with experimental results and reveals that stronger plasmonics modes radiate into air on the starting-edge of the meniscus thin metal-film.

Chapter 7 presents the performance of a broadly tuneable *solid* WGM MBR with high-*Q* fabricated by slightly overlapping two standard optical fibres during an arc-fusion-splicing process. Simplification to the dense and complex MBR spectral feature are first established by exciting the WGMs via the up-taper region of an optical tapered fibre. The TE- and TM-WGM resonances shift with the applied mechanical strain and polarization resolved measurements have resulted in a TM-WGM shift over an entire FSR, along with TM-/TE-WGM resonance shift ratio of 1.67.

Finally, chapter 8 concludes the thesis and discusses potential future works.

1.4 References

[1] L. Rayleigh, “The problem of whispering gallery,” *Philosophical Magazine* **20**, 1001-1004 (1910).

[2] L. Rayleigh, “Further applications of Bessel’s functions of high order to the whispering gallery and allied problems,” *Philosophical Magazine* **27**, 100-109 (1914).

[3] J.A. Lott, N. N. Ledentsov, V. M. Ustinov, N. A. Maleev, A. E. Zhukov, A. R. Kovsh, M. V. Maximov, B. V. Volovik, Zh. I. Alferov, and D. Bimberg, “InAs-InGaAs quantum dot VCSELs on GaAs substrates emitting at 1.3 µm”, *Electronics Letters* **36**, 1384-1385 (2000).

[4] J. T. Kringlebotn, J.-L. Archambault, L. Reekie, and D. N. Payne, "Er^{3+}:Yb^{3+}-codoped fiber distributed-feedback laser," *Optics Letters* **19**, 2101-2103 (1994).

[5] M. N. Mohd Nasir, Z. Yusoff, M. H. Al-Mansoori, H. A. Abdul Rashid, and P. K. Choudhury, "Widely tunable multi-wavelength Brillouin-erbium fiber laser utilizing low SBS threshold photonic crystal fiber," *Optics Express* **17**, 12829-12834 (2009).

[6] I. N. Duling, "All-fiber ring soliton laser mode locked with a nonlinear mirror," *Optics Letters* **16**, 539-541 (1991).

[7] R. D. Richtmyer, “Dielectric resonators,” *Journal of Applied Physics* **10**, 391-398 (1939.)

[8] C. G. B. Garrett, W. Kaiser, and W.L. Bond, “Stimulated Emission into Optical Whispering Modes of Spheres,” *Physical Review* **124**, 1807-1809 (1961).

[9] V.B. Braginsky, M.L. Gorodetsky, V.S. Ilchenko, “Quality-factor and nonlinear properties of optical whispering-gallery modes,” *Physics Letters A* **137**, 393-397 (1989).

[10] M. L. Gorodetsky, A. A. Savchenkov and V. S. Ilchenko, "Ultimate Q of optical microsphere resonators," *Optics Letters* **21**, 453-455 (1996).

[11] T. A. Birks, J. C. Knight and T. E. Dimmick, "High-Resolution Measurement of the Fiber Diameter Variations Using Whispering Gallery Modes and No Optical Alignment," *IEEE Photonics Technology Letters* **12**, 182-183 (2000).

[12] D. K. Armani, T. J. Kippenberg, S. M. Spillane, and K. J. Vahala, “Ultra-high-Q toroid microcavity on a chip,” *Nature* **421**, 925 (2003).

[13] T. J. Kippenberg, S. M. Spillane, and K. J. Vahala, “Demonstration of ultra-high-Q small mode volume toroid microcavities on a chip,” *Applied Physics Letters* **85**, 6113-6115 (2004).

[14] G. S. Murugan, J. S. Wilkinson, and M. N. Zervas, “Optical microdiscus resonators by flattening microspheres,” *Applied Physics Letters* **101**, 071106 (2012).

[15] M. Sumetsky, "Whispering-gallery-bottle microcavities: the three-dimensional etalon," *Optics Letters* **29**, 8-10 (2004).

[16] Y. Louyer, D. Meschede, and A. Rauschenbeutel, “Tunable whispering-gallery-mode resonators for cavity quantum electrodynamics,” *Physical Review A* **72**, 031801 (2005).

[17] G. S. Murugan, J. S. Wilkinson, and M. N. Zervas, "Selective excitation of whispering gallery modes in a novel bottle microresonator," *Optics Express* **17**, 11916-11925 (2009).

[18] M. Sumetsky and J. M. Fini, “Surface nanoscale axial photonics,” *Optics Express* **19**, 26470 (2011).

[19] G. Kakarantzas, T. E. Dimmick, T. A. Birks, R. Le Roux, and P. St. J. Russell, "Miniature all-fiber devices based on CO_2 laser microstructuring of tapered fibers," *Optics Letters* 26, 1137-1139 (2001).

[20] J. M. Ward, D. G. O’Shea, B. J. Shortt, M. J. Morrissey, K. Deasy, and S. G. Nic Chormaic, “Heat-and-pull rig for fiber taper fabrication,” *Review of Scientific Instruments* **77**, 083105 (2006).

[21] F. Warken, A. Rauschenbeutel and T. Bartholomaus, "Fiber pulling profits from precise positioning.," *Photonics Spectra* **42**, 73 (2008).

[22] M. Pollinger, D. O’Shea, F. Warken and A. Rauschenbeutel, "Ultrahigh-Q Tunable Whispering-Gallery-Mode Microresonator," *Physical Review Letters* **103**, 053901 (2009).

[23] G. S. Murugan, J. S. Wilkinson, and M. N. Zervas, "Hollow-bottle optical microresonators," *Optics Express* **19**, 20773-20784 (2011).

[24] K. J. Vahala, “Optical microcavities,” *Nature* **424**, 839-846 (2003).

[25] V. S. Ilchenko and A. B. Matsko, “Optical resonators with whispering-gallery modes- Part II: Applications,” *IEEE Journal of selected topics in quantum electronics* **12**, 15-32 (2006).

[26] B. Min, E. Ostby, V. Sorger, E. Ulin-Avila, L. Yang, X. Zhang, and K. Vahala, “High-*Q* surface-plasmon-polariton whispering-gallery microcavity,” *Nature* **457**, 455-458 (2008).

[27] M. Ding, G. S. Murugan, G. Brambilla, and M. N. Zervas, “Whispering gallery mode selection in optical bottle microresonators,” *Applied Physics Letters* **100**, 081108 (2012).

[28] G. S. Murugan, J. S. Wilkinson, and M. N. Zervas, "Optical excitation and probing of whispering gallery modes in bottle microresonators: potential for all-fiber add–drop filters," *Optics Letters* **35**, 1893-1895 (2010).

[29] M. Pöllinger and A. Rauschenbeutel, "All-optical signal processing at ultra-low powers in bottle microresonators using the Kerr effect," *Optics Express* **18**, 17764-17775 (2010).

[30] A. Rottler, M. Harland, M. Bröll, M. Klingbeil, J. Ehlermann, and S. Mendach, “High-*Q* Hybrid Plasmon-Photon Modes in a Bottle Resonator Realized with a Silver-Coated Glass Fiber with a Varying Diameter,” *Physical Review Letters* **111**, 253901 (2013).

Chapter 2: Basics of optical microcavities and whispering gallery modes

2.1 Introduction

Key parameters which determine the main characteristics of a waveguide-coupled optical microresonator include the coupling factor and quality factor as they govern the power circulating within the system as well as the attributed wavelengths. In this chapter, the governing factors of an optical microresonator coupling strength and its corresponding quality factor are explored. Modes and fields of optical microsphere and microbottle resonators are first determined in section 2.2 and 2.3, respectively. In section 2.4, the fields of a tapered optical fibre that is utilized in coupling light to a whispering-gallery mode (WGM) resonator are determined. It is followed by establishing the parameters which influence the coupling efficiency between a waveguide and a WGM resonator in section 2.5. In section 2.6, the power circulating inside a WGM resonator and the power transmitted through a coupling waveguide are determined for different coupling regimes. Section 2.7 discusses the main properties of optical microcavities that are relevant to microsphere and microbottle WGM resonators. In section 2.8, a brief summary of the chapter is presented.

2.2 Modes and fields of optical microspheres

Optical microspheres which support whispering-gallery modes (WGMs) confine electromagnetic resonances in a circular trajectory. The confined modes propagate around the sphere equator hence making it comparable to a 2D light-confinement. Modes of spherical resonators of a given polarization are characterized by three modal numbers, $n, m \text{ and } l$ [1]. The mode number n represents the electromagnetic field component in the radial direction, the mode number m represents the electromagnetic field component in the azimuthal (equatorial) direction, and the mode number l represents the electric field component in the polar (angular) direction. The number of field extrema in the azimuthal, angular and radial directions are represented by $2m$, $l - |m| + 1$, and n, respectively. The spherical coordinates are shown in Figure 2.1 with the radius r measured from origin, the angular angle, θ, representing the variation perpendicular to the yz plane, and the azimuthal angle, ϕ, representing the variation in the yz plane.

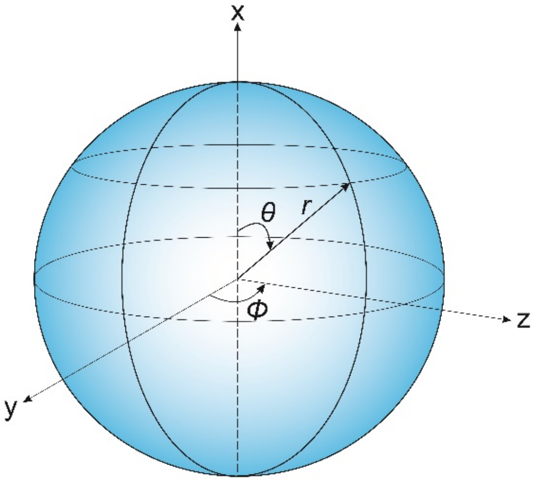

Figure 2.1 Spherical coordinates including radial, angular, and azimuthal coordinates (r, θ, ϕ).

The field which represents either the electric field (E_θ) or magnetic field (H_θ)components of the electromagnetic field of the WGM can be described by:

$$\Psi_{l,m,n}(r,\theta,\phi) = N_s \psi_r(r)\psi_\theta(\theta)\psi_\phi(\phi) \tag{2.1}$$

where

$$\psi_\phi(\phi) = \exp[\pm jm\phi], \tag{2.2a}$$

$$\psi_\theta(\theta) = \exp\left[-\frac{m}{2}\theta^2\right] H_N\left(\sqrt{m}\theta\right), \tag{2.2b}$$

$$\psi_r(r) = \begin{cases} j_l(kn_s r) & \text{if } \mathrm{r} \le \mathrm{R}_0 \\ j_l(kn_s \mathrm{R}_0)\exp[-\alpha_s(r-\mathrm{R}_0)] & \text{if } \mathrm{r} > \mathrm{R}_0 \end{cases} \tag{2.2c}$$

the normalization constant N_s is,

$$N_s = \left\{\sqrt{\frac{\pi}{m}}2^{N-1}N!\,\mathrm{R}_0^2\left[\left(1+\frac{1}{\alpha_s\mathrm{R}_0}\right)j_l^2(kn_s\mathrm{R}_0) - j_{l-1}(kn_s\mathrm{R}_0)j_{l+1}(kn_s\mathrm{R}_0)\right]\right\}^{-1/2} \tag{2.3a}$$

the coefficients α_s, β_l, N and k are:

$$\alpha_s = \sqrt{\beta_l^2 - k^2 n_0^2}, \quad \beta_l = \frac{\sqrt{l(l+1)}}{R_0} \tag{2.3b}$$

$$N = l - m, \quad k = \frac{2\pi}{\lambda} \tag{2.3c}$$

n_s and n_0 are the refractive indices of the sphere and the outside medium, respectively. α_s is the decay constant away from the sphere in the radial direction. β_l is the propagation constant parallel to the surface of the sphere. k is the wavenumber and R_0 is the radius of the sphere. The normalization constant, N_s, is chosen so that the volume integral of the square of magnitude of the field over the entire space in the sphere, divided by the sphere circumference is unity [1]. $\psi_\phi(\phi), \psi_\theta(\theta)$ and $\psi_r(r)$ represents the components of the electromagnetic field in the azimuthal, angular and radial directions, respectively. Figure 2.2 shows the angular distribution and the radial distribution of a sphere fundamental mode. The equatorial plane is perpendicular to the angular modal plane (transverse plane).

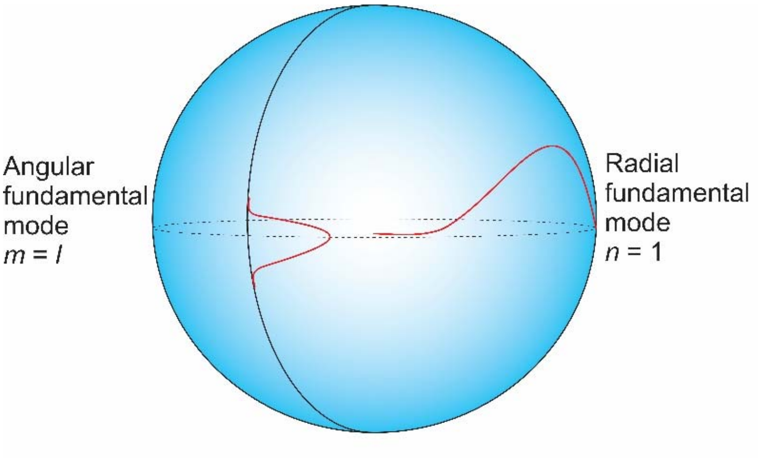

Figure 2.2 Spherical mode fields.

The characteristic equation which describes the relationship between the wave vector k, and the eigenvalues l and m can be determined by the matching tangential electric and magnetic fields across the spherical surface at $r = R_0$ [1]. Matching the tangential components of the electric and magnetic fields yields the characteristic equation

$$\left(\eta_s \alpha_s + \frac{l}{R_0}\right) j_l(kn_s R_0) = kn_s j_{l+1}(kn_s R_0) \tag{2.4}$$

where

$$\eta_s = \begin{cases} 1 & \text{TE mode} \\ \frac{n_s^2}{n_0^2} & \text{TM mode} \end{cases} \tag{2.5a}$$

$$k = \frac{2\pi}{\lambda} \tag{2.5b}$$

A resonance occurs when the optical path length of the WGM around the equator of the sphere is equal to an integer multiple of wavelengths. For a large sphere (compared to wavelength λ), l can be obtained from

$$l = 2\pi R_0 \frac{n_{\text{eff}}}{\lambda} \tag{2.6}$$

where l is the sphere azimuthal mode number, λ is the operating wavelength, and n_{eff} is the effective refractive index which corresponds to the cavity path length for each sphere mode. The sphere effective refractive index value needs to be below the value of the refractive index of the sphere. However, for each mode, the field that is extended to the outer region of the sphere is significantly small [2].

The radial dependence of the modal field distribution, $\psi_r(r)$, is described by the Spherical Bessel function, $j_l(x)$, and defined as [3, 4]

$$j_l(x) = (-1)^l x^l \left(\frac{d}{xdx}\right)^l \frac{\sin(x)}{x} \tag{2.7}$$

The spherical Bessel function is directly related to the well-known Bessel function

$$j_l(x) = \sqrt{\frac{\pi}{2x}} J_{l+0.5}(x) \tag{2.8}$$

where $J_l(x)$ is a Bessel function of the first kind of order l.

The first few terms of the Spherical Bessel function are described by equations

$$j_0(x) = \frac{\sin(x)}{x} \tag{2.9a}$$

$$j_1(x) = \frac{\sin(x)}{x^2} - \frac{\cos(x)}{x} \tag{2.9b}$$

$$j_2(x) = \left(\frac{3}{x^3} - \frac{1}{x}\right)\sin(x) - \frac{3}{x^2}\cos(x) \tag{2.9c}$$

The field in the angular direction, $\psi_\theta(\theta)$, is described by the Hermite-Gaussian function $\exp\left[-\frac{m}{2}\theta^2\right] H_N(\sqrt{m\theta})$, where $H_N(\sqrt{m\theta})$ are the Hermite polynomials. If $x = \sqrt{m\theta}$, the Hermite polynomials are defined by

$$H_N(x) = (-1)^N \exp(x^2) \frac{d^N}{dx^N} \exp(x^2) \tag{2.10}$$

The first four terms of the Hermite polynomials are [4, 5]

$$H_0(x) = 1, \tag{2.11a}$$

$$H_1(x) = 2x, \tag{2.11b}$$

$$H_2(x) = 4x^2 - 2, \tag{2.11c}$$

$$H_3(x) = 8x^3 - 12x, \tag{2.11d}$$

Mode numbers l and m determine the sphere electric filed in the angular direction. The integer m can range from $-l$ to l. The fundamental mode is obtained when $m = l$. However, all these modes are degenerate under the same wavelength on a perfect optical microsphere.

Figure 2.3 (a) shows the predicted m and l numbers associated with the modes supported by an ideal microsphere of radius $R_0 = 100\ \mu m$, microsphere refractive index $n_0 = 1.46$ and outside medium refractive index $n_1 = 1$ [6]. Figure 2.3 (b) shows the predicted m and l numbers associated with the modes supported by a *distorted* optical microsphere with radii $R_1 = 100\ \mu m$, $R_2 = 105\ \mu m$, microsphere refractive index $n_0 = 1.46$ and outside medium refractive index $n_1 = 1$ [6]. The distorted optical microsphere shows clear broken mode degeneracy at the resonant wavelengths. Along each vertical dashed line in figure 2.3 (a) (used here to guide the eye), the top point corresponds to angular number $l - m = 0$, while each subsequent point moving downwards corresponds to increasing value of the angular number $(l - m = 1,2,3 \dots)$. The same conventions apply to figure 2.3 (b). In both figures the radial number is $n = 1$.

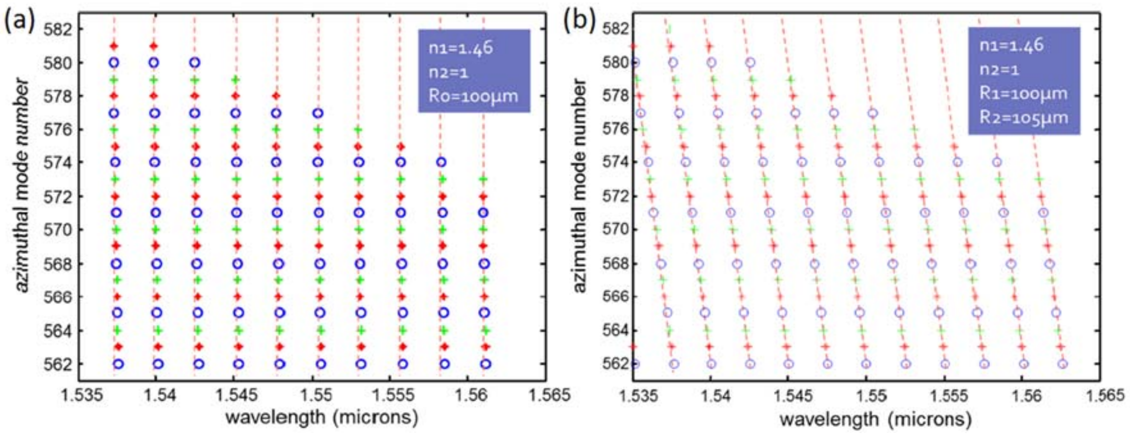

Figure 2.3 Resonant wavelengths and related azimuthal numbers m for (a) perfect and (b) distorted optical microsphere. Angular number from top point increases with subsequent point downwards $(l - m = 0,1,2,3..)$. Radial number for figure 2.3 (a) & (b) is $n = 1$.

2.3 Modes and fields of optical microbottle resonators

In contrast to 2D light-confinement of microspheres, microbottle resonators (MBRs) attain a 3D light-confinement structure through their combination of whispering-gallery and bouncing-ball confinement effects. Figure 2.4 illustrates the principle of a whispering-gallery MBR [7]. Light-confinement in such a structure, designated in cylindrical coordinates (z, ρ, φ), can be expanded into 2D whispering-gallery rays moving in the plane (ρ, φ) normal to the fibre axis z and 2D bouncing ball rays moving in the plane (z, ρ).

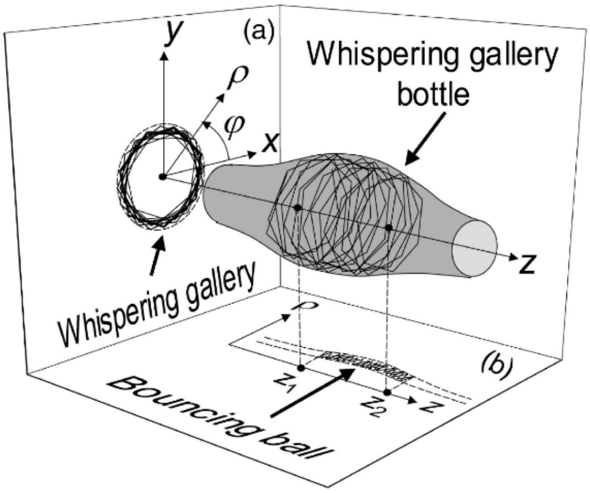

Figure 2.4 Illustration of whispering-gallery MBR and its projections on (a) plane (ρ, φ), and (b) plane (z, ρ) [7].

For the full-scale wave equation calculation of whispering-gallery MBRs on a dielectric structure, light confinement through the combination of equatorial WGMs and two turning points along the resonator axis should be considered. Figure 2.5 illustrates the concept of MBRs confinement where (a) light would spiral back and forth between two turning points that are separated by a distance $2z_c$, and (b) along an equatorial whispering-gallery [8]. Such modes exhibit two spatially separated caustics (caused by angular momentum barrier) located at $\pm z_c$ with an enhanced field strength.

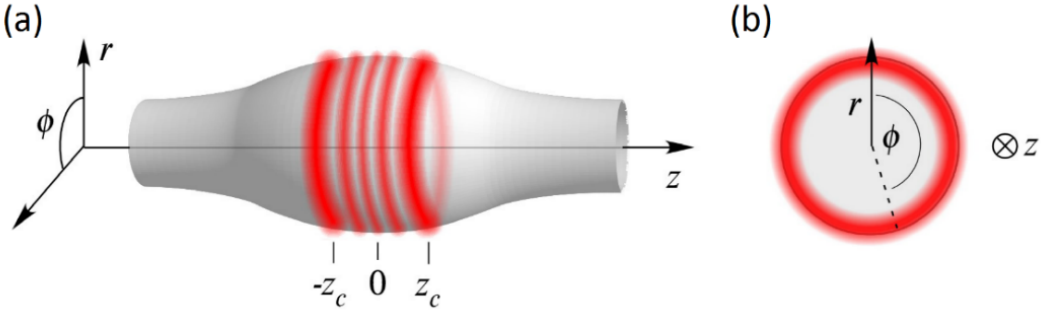

Figure 2.5 MBR geometry (a) along and (b) in a plane perpendicular to the resonator axis [8].

The MBR under study was considered to attain an approximate parabolic profile along the z axis

$$R(z) = R_0\left(1 - \frac{1}{2}(\Delta k)^2\right) \tag{2.12}$$

with the variation of the resonator radius being considered small, $dR/dz \ll 1$. Under the consideration of maximum angular momentum modes located close to the surface of the MBR, the radial component k_r of the wave vector is negligible with respect to k_z and k_ϕ. The total wavenumber can be expressed by

$$k = \sqrt{k_z^2 - k_\phi^2} = 2\pi n/\lambda \tag{2.13}$$

Due to cylindrical symmetry, the projection of the angular momentum onto the z axis is conserved, $\partial_z k_\phi(z)R(z) = 0$. Additionally, the axial component of the wave vector vanishes at radial R_c, $k_z(\pm z_c) = 0$, hence $k_\phi(\pm z_c) = k$. The axial dependency of k_ϕ is

$$k_\phi(z) = kR_c/R(z) \tag{2.14}$$

$$k_z(z) = \pm k\sqrt{1 - [R_c/R(z)]^2} \tag{2.15}$$

where $-z_c \leq z \leq z_c$ and $R_c = R(z_c)$.

Microbottle resonator modes of a given polarization are characterized by three modal numbers m, p, q, where $2m$ $(m = 0,1,2, \dots)$ denotes the number of field nodes around the circumference, p $(p = 1,2, \dots)$ is the power maxima along the radius, and q $(q = 0,1,2 \dots)$ gives the number of field nodes along the axis of the microresonator [9, 10]. With cylindrical symmetry, the azimuthal part of the wave equation can be separated with solutions proportional to $\exp(im\phi)$. The solution can be written $\Psi(r,z)\exp(im\phi)$ [8]. The radial mode number will be fixed to the minimum value $p = 1$, corresponding to modes located at the surface of the resonator. Using the adiabatic approximation along the z axis, $\Psi(r,z)$ can be separated in a product of two functions $\Phi(r,z)Z(z)$, where Φ is the solution of a Bessel equation

$$\frac{\partial^2\Phi}{\partial r^2} + \frac{1}{r}\frac{\partial\Phi}{\partial r} + \left(k_\phi^2 - \frac{m^2}{r^2}\right)\Phi = 0 \tag{2.16}$$

From equation (2.14) and using $kR_c = m$, $k_\phi(z) = m/R(z)$, and equation (2.16) yields

$$\frac{\partial^2\Phi}{\partial r^2} + \frac{1}{r}\frac{\partial\Phi}{\partial r} + m^2\left(\frac{1}{R(z)^2} - \frac{1}{r^2}\right)\Phi = 0 \tag{2.17}$$

In the scalar approximation, the transverse electric field is [7-10]

$$E(r,\phi,z) = \Phi(r,z)\Psi(z)\exp(im\phi) \tag{2.18}$$

where the radial distribution of the field is given by [10, 11]

$$\Phi(r,z) = \begin{cases} A_m \dfrac{J_m(U_{mp}\, r/R(z))}{J_m(U_{mp})} & r \leq R(z) \\ A_m \dfrac{K_m(U_{mp}\, r/R(z))}{K_m(U_{mp})} & r > R(z) \end{cases} \tag{2.19}$$

J_m is the Bessel function of the first kind for field distribution inside the dielectric [3], K_m is the modified Bessel function of the second kind which decays exponentially outside the dielectric [12], the coefficient A_m is determined such that the boundary condition is satisfied.

In the case of highly multimoded fibres, ignoring polarization effects, U_{mp} is approximated by the p^{th} root of the $J_m(U)$ function. U_{mp} can also be approximated by analytical expression [13,14]

$$U_{mp} = m + \alpha_p \left({}^{m}\!/_{2}\right)^{1/3} + \left({}^{3}\!/_{20}\right)\alpha_p^2 \left({}^{m}\!/_{2}\right)^{-1/3} \tag{2.20}$$

where α_p is the p^{th} root of the airy function ($\alpha_p = 2.3381, 4.0879, 5.5205, 6.7867, 7.9441$ for $p = 1,2,3,4,5$, respectively) [15].

Differential equation for Z distribution (MBR z-direction of figure 2.5) also depends on the bottle resonator profile $R(z)$. For analytical solution, the bottle resonator profile is considered to be $R(z) = R_0/\sqrt{1 + (\Delta k z)^2}$, and this simplifies the distribution to a harmonic oscillator profile

$$\frac{\partial^2 Z}{\partial z^2} + \left(k^2 - \frac{m^2}{R_0^2} - \frac{m^2 \Delta k^2}{R_0^2}\right) Z = 0 \tag{2.21}$$

In correlation to the harmonic oscillator profile, the total and the potential energy of the bottle resonator were identified as $E = k_2 - m^2/R_0^2$ and $V(z) = (\Delta E_m z/2)^2$, respectively, where $\Delta E_m = 2m\Delta k/R_0$. Also, the condition that Z be square integrable leads to a discrete set of energy levels $E_{mq} = (q + 1/2)\Delta E_m$. The eigenvalues could then be deduced to

$$k_{mq} = \left[\frac{m^2}{{R_0}^2} + \left(q + \frac{1}{2}\right)\Delta E_m\right]^{1/2} \tag{2.22}$$

Axial distribution field of a bottle resonator is then given analytically by [8, 10]

$$\Psi(\mathrm{z}) = C_{mq} H_q\left(\sqrt{\frac{\Delta E_m}{2}}\, z\right)\exp\left(-\frac{\Delta E_m}{4} z^2\right) \tag{2.23}$$

where H_q is the m^{th} order Hermite polynomial [5], and the normalization constant $C_{mq} = [\Delta E_m/\pi 2^{2q+1}(q!)^2]^{1/4}$. The axial spreading of each mode, the defined by corresponding turning point measured from the microbottle centre, is given by [9]

$$z_c = \pm\left[\frac{4}{\Delta E_m}\left(q + \frac{1}{2}\right)\right]^{1/2} \tag{2.24}$$

Beyond this point the mode is evanescent. The resonant wavelength for a bottle resonator with maximum radius of R_b for each $(m, p\,, q)$ is given from equation (2.22) [10]:

$$\lambda_{mpq} = 2\pi n_0 \left[\left(\frac{U_{mp}}{R_b}\right)^2 + \left(q + \frac{1}{2}\right)\Delta E_m\right]^{-1/2} \tag{2.25}$$

where $\Delta E_m = 2U_{mp}\Delta k/R_b$. When $\Delta k = 0$, or $R(z) = R_b$ in the case of cylindrical resonator, equation (2.25) reduces to

$$\lambda_{mp} = \frac{2\pi n_0 R_b}{U_{mp}} \tag{2.26}$$

giving the resonant wavelength of the (m, p) mode supported by a cylindrical resonator of radius R_b. Figure 2.6 plots the resonant wavelengths and the related modal numbers (m, p, q) for a MBR harmonic-oscillator with (a) the transverse wave vector U_{mp} obtained from equation (2.20) and TE polarization, and (b) the common approximation of $U_{mp} = m$ [6]. For modes localizing near the surface of the resonator, $p \ll m$, and $U_{mp} \approx m$ [7]. $U_{mp} = m$ is a commonly used approximation and used instead of the much more accurate expression of equation (2.20) that can provide accurate values of U_{mp} for different values of radial number p. The MBR under study has maximum bottle radius $R_b = 100\ \mu\text{m}$, stem radius $R_s = 70\ \mu\text{m}$, axial bottle length $L_b = 140\ \mu\text{m}$, bottle refractive index $n_0 = 1.46$, and outside medium refractive index $n_1 = 1$.

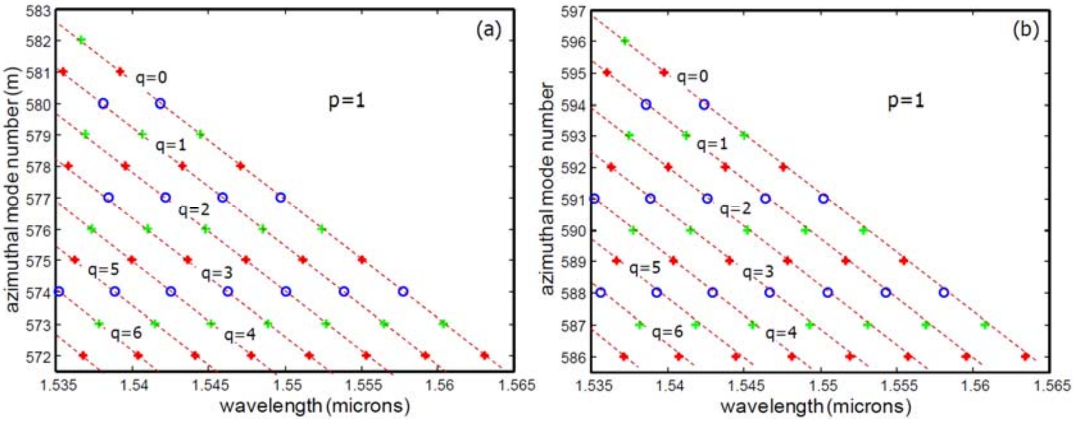

Figure 2.6 Resonant wavelengths and related modal numbers (m, p, q) for a harmonic oscillator MBR of (a) U_{mp} from equation (2.20), and (b) $U_{mp} = m$ [6].

The intensity distribution over a MBR cross-section and along the length for modal numbers $(m, p, q) = (731,3,20)$ of the TE polarized mode is illustrated in Figure 2.7 [6]. The MBR has diameter $D_b = 265\ \mu\text{m}$ and length $L_b = 550\ \mu\text{m}$ [10].

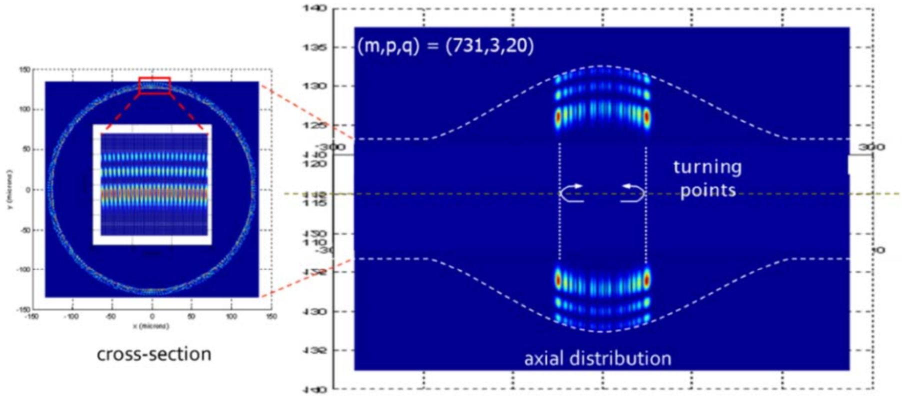

Figure 2.7 MBR intensity profile for a TE polarized mode with $(m, p, q) = (731,3,20)$ [6].

2.4 Fields of tapered optical fibres

Tapered optical fibres utilized in all of the experiments in this thesis were fabricated by heating the core and cladding of a conventional single-mode fibre (SMF) and drawing it to attain a narrow waist. For fields which are linearly polarized, the analytical form of tapered fibre modes with radius a, core index n_f and cladding index $n_{cl} = n_0$ (as illustrated in figure 2.8) is [1]

$$F_0(\rho) = \begin{cases} J_0^{-1}(k_f a) J_0(k_f \rho) & \text{if } \rho \le a \\ \exp[-\gamma_f(\rho - a)] & \text{if } \rho > a \end{cases} \tag{2.27}$$

where

$$N_f = \frac{\alpha_f J_0(k_f a)}{V_f \sqrt{\pi} J_1(k_f a)} \tag{2.28a}$$

$$k_f = \sqrt{k^2 n_f^2 - \beta_f^2} \quad , \quad \alpha_f = \sqrt{\beta_f^2 - k^2 n_{cl}^2} \tag{2.28b}$$

$$\gamma_f = \alpha_f \frac{K_1(\alpha_f a)}{K_0(\alpha_f a)} \quad , \quad V_f = ka\sqrt{n_f^2 - n_{cl}^2} \tag{2.28c}$$

where J_0 and J_1 are the Bessel functions of zero and first order, and K_0 and K_1 are the modified Hankel functions of zero and first order. Normalization constant N_f is obtained by integrating $F_o^2(\rho)$ over the transverse dimension and is made unity. Outside the core of the optical fibre, the modified Hankel function is utilized to determine the field by fitting decay constant γ_f.

The characteristic equation used to determine fibre mode propagation constant β_f is [1]:

$$k_f \frac{J_1(ak_f)}{J_0(ak_f)} - \alpha_f \frac{K_1(a\alpha_f)}{K_0(a\alpha_f)} = 0 \tag{2.29}$$

2.5 Coupling of tapered optical fibre to a WGM microresonator

For simplicity, the coupling of a tapered optical fibre to a WGM microresonator presented in this section is with an optical microsphere. Nonetheless, the coupling principle shown can also be utilized for the cross-section of an optical microbottle resonator. Figure 2.8 illustrates the cross-sectional view of the geometry of a tapered fibre and a microsphere [1].

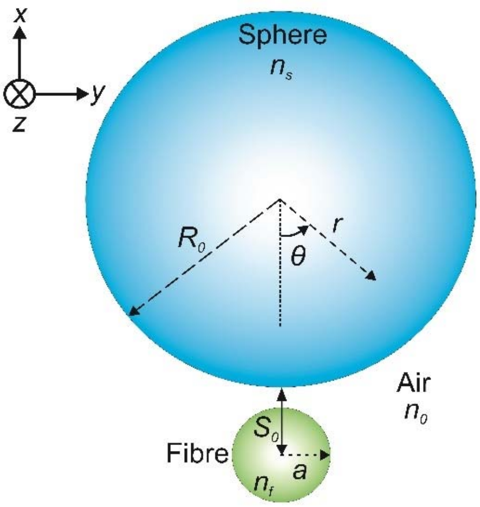

Figure 2.8 Cross-sectional view of the geometry of a tapered fibre coupled to a microsphere.

By using resonance wavelength and propagation constant of equation (2.4), the field of microsphere and tapered fibre could be determined. Using coupled mode theory, the interaction strength of the normalized spherical and fibre fields at minimum separation value of S_0 can be determined by

$$\kappa(S_0) = \frac{k^2}{2\beta_f}\int_x \int_y (n_s^2 - n_0^2)F_0\Psi_{l,m,n}\,dx\,dy \tag{2.30}$$

where $\kappa(S_0)$ is the increase rate of amplitude of the sphere mode at the minimum separation with the fibre, and β_f is the tapered fibre propagation constant. Assuming a parabolic profile of the sphere at the minimum separation distance, the interaction decreases with a Gaussian dependency away from this point along the length of the fibre.

κ is the transfer of amplitude from the fibre to the sphere per revolution of the mode. κ^2 is the amount of power coupled out of the fibre into the sphere per revolution, where

$$\kappa^2 = \kappa^2(S_0)\frac{\pi}{\gamma_t}\exp\left[-\frac{\Delta\beta^2}{2\gamma_t}\right] \tag{2.31a}$$

$$\Delta\beta = \beta_f - \beta_m\,, \qquad R_e = \frac{R_b R_0}{R_b - R_0}\,, \qquad \gamma_t = \frac{\gamma_f}{2R_e} \tag{2.31b}$$

$\Delta\beta$ is the difference in the propagation constants between the fibre mode β_f and the microsphere mode β_m with value m, where $\beta_m = m/R_0$. This phase mismatch reduces the coupling efficiency. R_e is the effective radius of the sphere as seen by the fibre that includes the bending of the radius R_b. In a straight fibre, $R_b \to \infty$, and $R_e = R_0$.

2.6 System power-transfer functions

The power-transfer characteristics covered in this section is based on a universal unidirectional coupling method. Figure 2.9 illustrates the exchange of optical power between a waveguide (fibre) and a resonator in a lossless system [16].

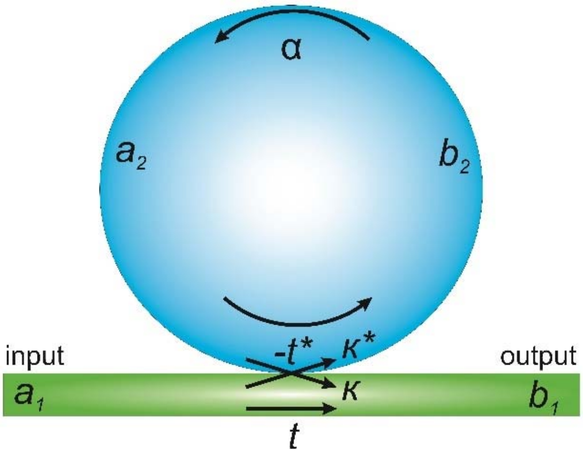

Figure 2.9 Cross-coupling factor and transmission coefficients of a universal lossless coupling system.

Interaction of the above coupling system can be described by matrix relation

$$\begin{vmatrix} b_1 \\ b_2 \end{vmatrix} = \begin{vmatrix} t & \kappa \\ -\kappa^* & t^* \end{vmatrix} \begin{vmatrix} a_1 \\ a_2 \end{vmatrix} \tag{2.32}$$

Complex mode amplitude b_i and a_i are normalized so that their squared magnitude corresponds to the modal power. From energy conservation

$$|t^2| + |\kappa^2| = 1 \tag{2.33}$$

With normalized input wave of $a_1 = 1$, the transmission around the resonator is

$$a_2 = \alpha e^{i\theta} b_2 \tag{2.34}$$

where α is the inner circulation factor, which, with zero internal loss, becomes $\alpha = 1$. It can be calculated from equation (2.32) and (2.34) that

$$b_1 = \frac{-\alpha + te^{-i\theta}}{-\alpha t^* + e^{-i\theta}} \tag{2.35a}$$

$$a_2 = \frac{-\alpha\kappa^*}{-\alpha t^* + e^{-i\theta}} \tag{2.35b}$$

The transmission in the waveguide past the coupling point is

$$|b_1|^2 = \frac{\alpha^2 + |t|^2 - 2\alpha|t|\cos(\theta + \phi_t)}{1 + \alpha^2|t|^2 - 2\alpha|t|\cos(\theta + \phi_t)} \tag{2.36}$$

where $t = |t|\exp(i\varphi_t)$. The total power circulating in the resonator is

$$|a_2|^2 = \frac{\alpha^2(1 - |t|^2)}{1 - 2\alpha|t|\cos(\theta + \phi_t) + \alpha^2|t|^2} \tag{2.37}$$

Interesting features of the coupling system occur near resonance at $(\theta + \varphi_t) = 2\pi m$, where m is an integer, φ is the circulation phase shift and can be calculated from [17]

$$\varphi = \frac{2\pi^2 \mathrm{D} n_{\mathrm{eff}}}{\lambda} \tag{2.38}$$

D is the resonator diameter and n_{eff} corresponds to the effective refractive index of the WGM. At resonance

$$|b_1|^2 = \frac{(\alpha - |t|)^2}{(1 - \alpha|t|)^2} \tag{2.39a}$$

$$|a_2|^2 = \frac{\alpha^2(1 - |t|)^2}{(1 - \alpha|t|)^2} \tag{2.39b}$$

Equation (2.39a) and (2.39b) determine the transmitted power through the waveguide and circulating power inside the resonator, respectively. There are three distinct coupling regimes of the system

- **Under-coupling,** $\alpha < t$
  $< 100\%$ of the waveguide incident light is coupled into the resonator. Intrinsic resonator losses are smaller than waveguide induced losses. Non-zero transmission at resonance $|b_1|^2 \neq 0$, with small and sharp features.
- **Critical-coupling**, $\alpha = |t|$
  100% of the waveguide incident light is coupled into the resonator and dissipated inside the resonator. Intrinsic resonator loss exactly equals the waveguide induced loss. Zero transmission at resonance $|b_1|^2 = 0$.
- **Over-coupling,** $\alpha > t$
  100% of the waveguide incident light is coupled into the resonator but part of the light coupled back into the waveguide. Waveguide induced loss dominates. Non-zero transmission at resonance $|b_1|^2 \neq 0$.

2.7 Properties of optical microresonators

In this section, an overview of the main properties of optical microcavities are presented. The main properties include microresonators quality Q-factor, free spectral range FSR, finesse $\mathcal{F}$ and mode volumes V.

2.7.1 Quality factor

Quality factor of a resonator is a dimensionless parameter which is a measure of the strength of the damping of its oscillations and corresponds to the temporal confinement of light in the resonator. It is generally defined as the ratio of stored energy to the power loss [18] and it is a measure for how long a photon can be stored in a cavity

$$Q = 2\pi \frac{\text{Stored energy}}{\text{Power loss per roundtrip}} \tag{2.40}$$

Many mechanisms contribute to the overall Q-factor of a WGM cavity microresonator. They can be connected by

$$\begin{aligned}\frac{1}{Q_{total}} &= \frac{1}{Q_{mat}} + \frac{1}{Q_{WGM}} + \frac{1}{Q_{ss}} + \frac{1}{Q_{cont}} + \frac{1}{Q_{coupling}} \\ &= \frac{1}{Q_{intrinsic}} + \frac{1}{Q_{coupling}}\end{aligned} \tag{2.41}$$

where Q_{total} represents the total Q-factor of the cavity. Intrinsic Q value owes to the combination of the resonator material loss (Q_{mat}), radiation losses due to curvature of the dielectric cavity (Q_{WGM}), surface scattering (Q_{ss}), and any contamination on the resonator (Q_{cont}). $Q_{coupling}$ signifies the energy loss due to input/output coupling. For the case of MBRs, mechanisms which can affect Q-factor values are intrinsic material absorption and radiation losses caused by waveguide bending and/or surface roughness scattering.

The external Q-factor of the tapered fibre and microsphere system can be calculated [1, 19] through equation

$$Q_e = \frac{m\pi}{\kappa^2} \tag{2.42}$$

The Q-factor is also related to the linewidth $\Delta\lambda$ of the resonance at wavelength λ, and the photon cavity lifetime τ by

$$Q = \frac{\Delta\lambda}{\lambda} = \omega_0 \tau \tag{2.43}$$

where ω_0 is the optical frequency ($\omega = 2\pi c/\lambda$).

2.7.2 Free spectral range

The free spectral range (FSR) of a cavity is commonly defined as the frequency spacing of its axial cavity modes. As a physical resonator size decreases (yielding shorter optical path length), its FSR increases. The modes which determine the FSR are the successive modes which have the same transverse mode structure. The axial ($\Delta v_q = v_{m,q+1} - v_{m,q}$) and azimuthal ($\Delta v_m = v_{m+1,q} - v_{m,q}$) FSRs can be derived from the eigenvalues $k_{m,q}$ of the wave function. They can be approximated by

$$\Delta v_m = \frac{c}{2\pi n}\left(k_{m+1,q} - k_{m,q}\right) \approx \frac{c}{2\pi n R_0} \tag{2.44}$$

$$\Delta v_q \approx \frac{c\Delta k}{2\pi n} \tag{2.45}$$

2.7.3 Finesse

Finesse $\mathcal{F}$ is the ratio of the cavity mode spacing to the cavity bandwidth. The definition factors in both the cavity loss and mode spacing in order to obtain a single dimensionless parameter which characterizes the ability to resolve the cavity resonance structure

$$\mathcal{F} = \frac{\Delta\lambda_{FSR}}{\Delta\lambda} = \frac{\lambda Q}{2\pi n R} \tag{2.46}$$

2.7.4 Mode volume

Mode volume V of a resonator corresponds to the spatial confinement of light in the cavity. In a small optical mode volume, the energy of the electric field would be stored in a small portion of space which results in a high optical energy density.

2.7.4.1 Mode volume of spherical resonator

The mode volume can be defined as

$$V_{\text{mode}} \approx \frac{\left(\int_{V_Q} \epsilon(\vec{r})|E|^2 d^3\vec{r}\right)^2}{\int_{V_Q} |E|^4 d^3\vec{r}} \tag{2.47}$$

where $\epsilon(\vec{r}) = N^2(\vec{r})$ is the dielectric material constant at $\vec{r}$, $\vec{E}$ represents the cavity field value, and V_Q is the integration volume. Spherical mode volume of electromagnetic field radial order $n = 1$ can also be approximated by [20]

$$V_{\mathrm{mode}} \approx 3.4\pi^{3/2}(\lambda/2\pi n)^3 l^{11/6}\sqrt{l-m-1} \tag{2.48}$$

where n is the refractive index of the sphere.

2.7.4.2 Mode volume of microbottle resonator

The mode volume $V_{m,q}$ of bottle resonators can be directly calculated by its radial and axial intensity distribution [8]. The intensity distribution is normalized to unity $I_{m,q}/I_{m,q}^{max}$ for calculation and then integrated over $\mathbb{R}^3$

$$V_{m,q} = \iiint_0^{R_{rad}} n^2(r)\frac{I_{m,q}(r,z)}{I_{m,q}^{max}} r d_r d_\phi d_z \tag{2.49}$$

where the upper limit for the radial integral is set to R_{rad}. With cylindrical symmetry, the integration over the azimuthal coordinate yields $\int \left|e^{im\phi}\right|^2 d_\phi = 2\pi$. For computation of the mode volume, the integral is split into radial and axial part

$$V_{m,q} \approx 2\pi \cdot \int \left(\frac{Z_{m,q}(z)}{Z_{m,q}^{max}}\right)^2 d_z \cdot \int_0^{R_{rad}} n^2(r)\left(\frac{\left|\vec{E}(r)\right|^2}{\max\left(\left|\vec{E}(r)\right|^2\right)} r d_r\right) \tag{2.50}$$

2.8 Summary

The modes and fields of optical microsphere, microbottle resonators and tapered fibre have been briefly discussed. Optical microsphere and microbottle WGM fields are described in a 3-dimensional coordinates. For an optical microsphere the fields are being determined by the mode numbers l, m, n and for optical microbottle the fields are being determined by the mode numbers m, p, q. The coupling of optical tapered fibre to a WGM resonator was presented with coupling constant κ governing the system performance. The difference in the propagation constants $\Delta\beta$ resulted in a phase mismatch that reduces the coupling efficiency of the system. A universal system power-transfer function (which contemplate the resonator inner circulation factor α and waveguide transmission factor t) was considered in this thesis for the exchange of power between a waveguide (tapered fibre) and a WGM resonator. Three distinct coupling regimes which best describe system power-transfer functions between an optical tapered fibre and a WGM resonator are under-coupling ($\alpha < t$), critical-coupling ($\alpha = |t|$), and over-coupling ($\alpha > t$). The properties of optical microresonators which define its characteristics were also explained. The free-spectral range of a resonator shows its frequency/wavelength spacing. The finesse $\mathcal{F}$ of a resonator factors in the cavity loss and the mode spacing of the resonator. The quality factor (Q-factor) corresponds to the temporal confinement of light in the resonator and the mode volume V corresponds to the spatial confinement of light in the resonator.

2.9 References

[1] B. E. Little, J. P. Laine and H. A. Haus, "Analytic theory of coupling from tapered fibers and half-blocks into microsphere resonators," *Journal of Lightwave Technology* **17**, 704-715 (1999).

[2] Y. Panitchob, "Integration of glass microspheres and planar waveguides for microsphere lasers," Ph.D Thesis, University of Southampton, U.K., 2008.

[3] http://mathworld.wolfram.com/SphericalBesselFunctionoftheFirstKind.html

[4] M. Abramowitz and I. A. Stegun, "*Handbook of Mathematical Functions with Formulas, Graphs, and Mathematical Tables*," Dover, New York, 1964. ISBN 0-486-61272-4.

[5] http://mathworld.wolfram.com/HermitePolynomial.html

[6] M. N. Zervas, "Fabrication and modeling of truncated oblate and prolate microresonators," *Laser Resonators, Microresonators and Beam Control XV*, San Francisco, US, Feb 03 - 07 (2013).

[7] M. Sumetsky, "Whispering-gallery-bottle microcavities: the three-dimensional etalon," *Optics Letters* **29**, 8-10 (2004).

[8] Y. Louyer, D. Meschede, and A. Rauschenbeutel, "Tunable whispering-gallery-mode resonators for cavity quantum electrodynamics," *Physical Review A* **72**, 031801 (2005).

[9] G. S. Murugan, J. S. Wilkinson, and M. N. Zervas, "Selective excitation of whispering gallery modes in a novel bottle microresonator," *Optics Express* **17**, 11916-11925 (2009).

[10] G. S. Murugan, J. S. Wilkinson, and M. N. Zervas, "Hollow-bottle optical microresonators," *Optics Express* **19**, 20773-20784 (2011).

[11] D. Gloge, "Weakly Guiding Fibers," *Applied Optics* **10**, 2252-2258 (1971).

[12] http://mathworld.wolfram.com/ModifiedBesselFunctionoftheSecondKind.html

[13] S. Schiller and R. L. Byer, "High-resolution spectroscopy of whispering gallery modes in large dielectric spheres," *Optics Letters* **16**, 1138-1140 (1991).

[14] C. C. Lam, P. T. Leung, and K. Young, "Explicit asymptotic formulas for the positions, widths, and strengths of resonances in Mie scattering," *Journal of Optical Society America B* **9**, 1585-1592 (1992).

[15] http://mathworld.wolfram.com/AiryFunctionZeros.html

[16] A. Yariv, "Universal relations for coupling of optical power between microresonators and dielectric waveguides," *Electronics Letters* **36**, 321-322, (2000).

[17] J. M. Choi, R. K. Lee, and A. Yariv, "Control of critical coupling in a ring resonator–fiber configuration: application to wavelength-selective switching, modulation, amplification, and oscillation," *Optics Letters* **26**, 1236-1238 (2001).

[18] J. D Jackson, *"Classical Electrodynamics,"* John Wiley and Sons, New York, 1989. ISBN-10: 047130932X.

[19] B. E Little, S. T. Chu, A. Haus, J. Foresi, and J. -P. Laine, "Microring Resonator Channel Dropping Filters," *Journal of Lightwave Technology* **15**, 998-1005 (1997).

[20] V.B. Braginsky, M.L. Gorodetsky, and V.S. Ilchenko, "Quality-factor and nonlinear properties of optical whispering-gallery modes," *Physics Letters A* **137**, 393-397 (1989).

Chapter 3: Spectral cleaning and output modal transformations in WGM microresonators

3.1 Introduction

Optical microresonators (MRs), supporting whispering gallery modes (WGMs), have created much interest in the recent years for their great potential towards miniaturization and applications in advanced optical micro-systems [1,2]. Various microresonator geometries such as microsphere [3], microtoroid [4] and microdisc [5] are capable of storing light with high *Q*-factors and in small mode volumes. This is accomplished through the process of total internal reflection between the guiding and surrounding medium of the microcavity and the formation of WGMs. Since these types of resonators primarily confine light at their respective equatorial planes, they are generally considered as a 2-D resonator with the spectral properties being defined primarily by their diameters.

The study of optical MRs supporting WGMs has also been extended to include cylindrical structures, such as optical fibers, or MRs formed on fibers for their distinctive manner in confining light as well as for easy handling and incorporation in practical applications [6-8]. Among optical MRs fabricated on optical fibers, micro-bottle resonators (MBRs) have been given increased attention due to their unique manner of supporting WGMs. Through the combination of WG-ring and WG-bouncing ball principles, MBRs are able to support true 3-D WGM light confinement [9]. MBR shape approximates accurately a harmonic-oscillator profile with its WGM numbers being defined by *m* (azimuthal), *p* (radial) and *q* (axial) order [10,11]. The two distinctive MBR turning points correspond to regions of strong field enhancement and define the area of WGM modal confinement [9]. The presence of distinctive turning points in MBRs can be used for efficient adding/dropping functionality [12]. In contrast with spherical MRs, MBRs show highly non-degenerate resonances and very rich and complex transmission spectra [10]. This is due to the fact that as the radius of MBRs varies along the length, multiple overlapping effective cavities give rise to dense superimposed resonance spectra. It has been shown that the variation of radius even at the nano-scale is sufficient for MBRs to form and trap the light close to their surface [13].

The dense WGM spectral features of MBRs are advantageous for studies where large number of resonance modes are preferred, such as in cavity quantum electro-dynamics (QED) where multiple resonances are required to be simultaneously present on a linked quantum network [1]. This however is a serious limitation in applications, such as sensing, where monitoring of specific WGM resonance is required over a broad wavelength range. It is then necessary to have MBRs with simpler WGM spectra that are easily distinguishable and traceable over a broad spectral range. Previously, two techniques for cleaning and simplifying the complex and dense spectral features of MBRs have been demonstrated by preferentially attenuating subset of the supported WGMs. The first technique showed that efficient modal filtering can be achieved by placing high-index micro-droplets as diffractive loss elements on MBRs [11]. It was also observed that even after the spectral "clean-up", narrow spectral features would still consist of superposition of a few overlapping modes. A drawback of this method is that it is very hard to control and accurately position the micro-droplets in order to attenuate certain modes while ensuring the desired ones have survived. The second technique applied direct writing of micro-groove scars on the MBR surface with focused ion beam milling. In this case, the scars introduced to the resonator surface would scatter-out the majority of WGMs and reduce the surviving mode resonances significantly [14]. With accessible beam size of < 50 nm, high precision micro-groove shapes and designs can allow the user to accurately perform mode filtering and selection on MBRs. Nevertheless, while this particular technique is highly accurate, it involves expensive equipment and a number of additional fabrication steps.

In this chapter, the effect of the microtaper excitation fibre diameter (D_t) on the MBR transmission spectrum characteristics are studied systematically, and being proposed as an alternative very simple means of cleaning-up MBR transmission spectra. In section 3.2, it is shown that progressively cleaner and simpler spectra are obtained when D_t is increased from 2 μm to 10 μm. In all cases, the measured *Q*-factor values of the MBR resonances reaches > 10^6. Mode transformation as a result of light coupling from MBR back to the tapered fibre is also reported. Conversion of the LP_{01} microtaper fibre mode into LP_{11} takes place in a number of strong transmission resonances in the case of 2 μm taper waist diameter. Despite the much larger modality, modal transformation was observed to be not as frequent in the case of microtaper with 8 μm waist diameter. Discussion on the experimental spectral evolution of the MBR transmission spectra with the change of taper diameter are also presented and compared to theoretical modelling results. In section 3.3, the experimental evidence of the modal transformation in the microtaper waist, associated with strong resonances is presented, and compared to numerical simulations of planar waveguide/disc-resonator systems of section 3.4.

3.2 Microbottle resonator excitation source and spectral clean-up

The MBR utilized in the experiment was fabricated by the "soften-and-compress" technique [10]. A continuous SMF was placed in a manual-controlled fibre fusion splicer (Furukawa Electric Fitel S178A) where a small section of the fibre was heated through plasma arcing. At the same time, one of the two clamped-ends compressed the fibre in the direction of the arcing-region. This softeningand-compressing procedure yields increasing pronounced bulge along the fibre with each number of arcs performed. Figure 3.1 shows the fabricated MBR with various number of arcs performed on the SMF [10].

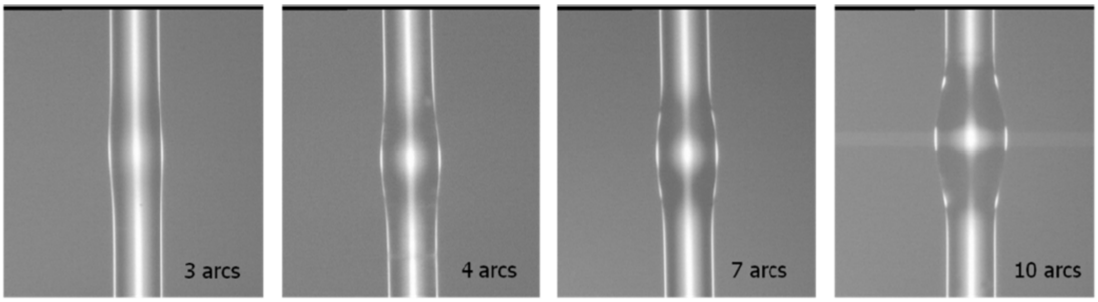

Figure 3.1 Fabricated MBR with "soften-and-compress" technique and different number of arcs [10].

As shown in figure 3.2, the fabricated microresonator had neck-to-neck distance L_b = 355 μm, bottle diameter D_b = 175 μm and stem diameter D_s = 125 μm. One of the important parts in MRs study is the coupling of light into and out of the microcavity. Several methods relying on energy exchange between WGMs and the evanescent part of guided modes or total internal reflection have been developed to efficiently couple light into the cavity of optical resonators. One of the earliest methods was based on prism coupling which relies on total internal reflection [15,16]. This method was later made more compact with the utilization of angle polished optical fibers instead of a prism [17]. Much recently, coupling light into WGM cavity using a fused-tapered fiber tip has been reported [18]. To date, the best method for coupling into a WGM microcavity with high efficiency is with the use of optical fiber microtapers. It is possible to couple more than 90% of the input light into the cavity of a high-*Q* fused silica resonator [19]. In the case of high-index barium titanate glass microspheres, it was reported that the required microtaper diameter (D_t) to observe strong transmission resonances is ≤ 2.5 μm [20].

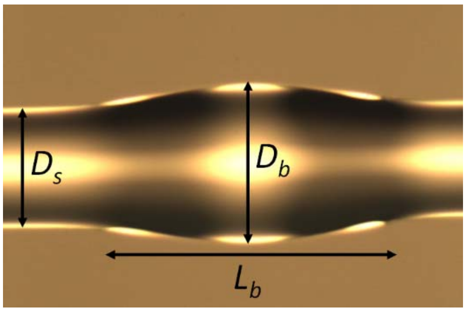

Figure 3.2 Fabricated MBR of L_b = 355 μm, D_b = 175 μm and D_s = 125 μm.

It is possible to control the excitation of MBR WGMs by varying the microtaper fiber waist diameters. For this study, five optical fibers tapered down adiabatically with D_t of 2, 4, 6, 8 and 10 μm were utilized to couple light into the cavity of the fabricated MBR. The tapers were fabricated from standard SMF-28 fibres using computer-controlled, in-house built tapering facilities. With the incorporation of a three-axis micro-positioning stage, the tapered fibers were arranged to be in contact with and at right angles to the MBR axis**.** Although this technique overloads the cavity and reduces the resonator overall Q-factor, it forms a robust and stable optical arrangement suitable for use in sensing and other practical applications. The narrow linewidth (~100 kHz) output from a tunable laser source (TLS) was launched into one end of the tapered fiber with the other end connected to an InGaAs photo-detector for transmitted power monitoring. By utilizing a charge-coupled device (CCD) camera, it is possible to observe any light scattering by the MBR. Figure 3.3 show the image of the MBR coupled to a tapered fibre at the centred position (a) without and (b) with 1550 nm lasing light launched through the tapered fibre. Excitation of the MBR modes with characteristic intensity maxima on both sides of the bottle could be seen in figure 3.3 (c) when lasing light was launched at just one side of the microbottle-neck.

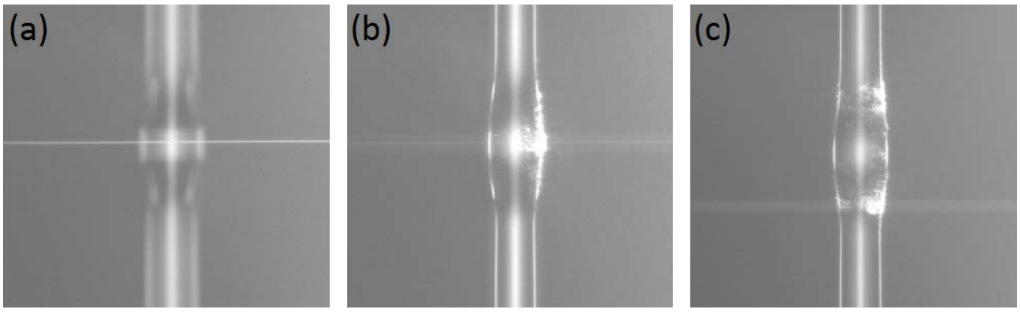

Figure 3.3 (a) Tapered fibre coupled at the centre of the MBR. Light scattering by MBR with 1550 nm lasing light launched through the tapered fibre at (b) the centre and (c) at the micro-bottle neck coupling arrangement.

Figure 3.4 shows the transmission spectra of the tapered fibre-coupled MBR when excited at the centre with D_t of (a) 2, (b) 4, (c) 6, (d) 8 and (e) 10 μm. With the smallest taper diameter D_t = 2 μm, a dense transmission spectrum with strong excitation of WGMs is observed. As the taper diameter increases to 10 μm the transmission spectrum becomes progressively cleaner and the maximum transmission dip decreases. The simpler transmission spectrum of the tapered fibre-coupled MBR excited with D_t of 10 μm also shows clearly the FSR of the MBR is $\approx 3.2\ nm$. Figure 3.4 (f) and (g) show the similar transmission spectra (albeit with different transmission strengths) selected in order to determine the FSR of the microcavity. In addition, strong and dense transmission spectra with tapered fibre of small D_t are accompanied by sizable insertion loss, predominantly due to excessive excitation of free-space radiation modes and a large number of partially overlapping and over-coupled WGMs (as a result of the taper being in direct contact with the MBR). The results are summarized in figure 3.5, where a decrease of the transmission dip from ~20 dB to ~4 dB and an insertion loss from ~12 dB to ~0 dB is measured as the taper diameter increases from 2 μm to 10 μm.

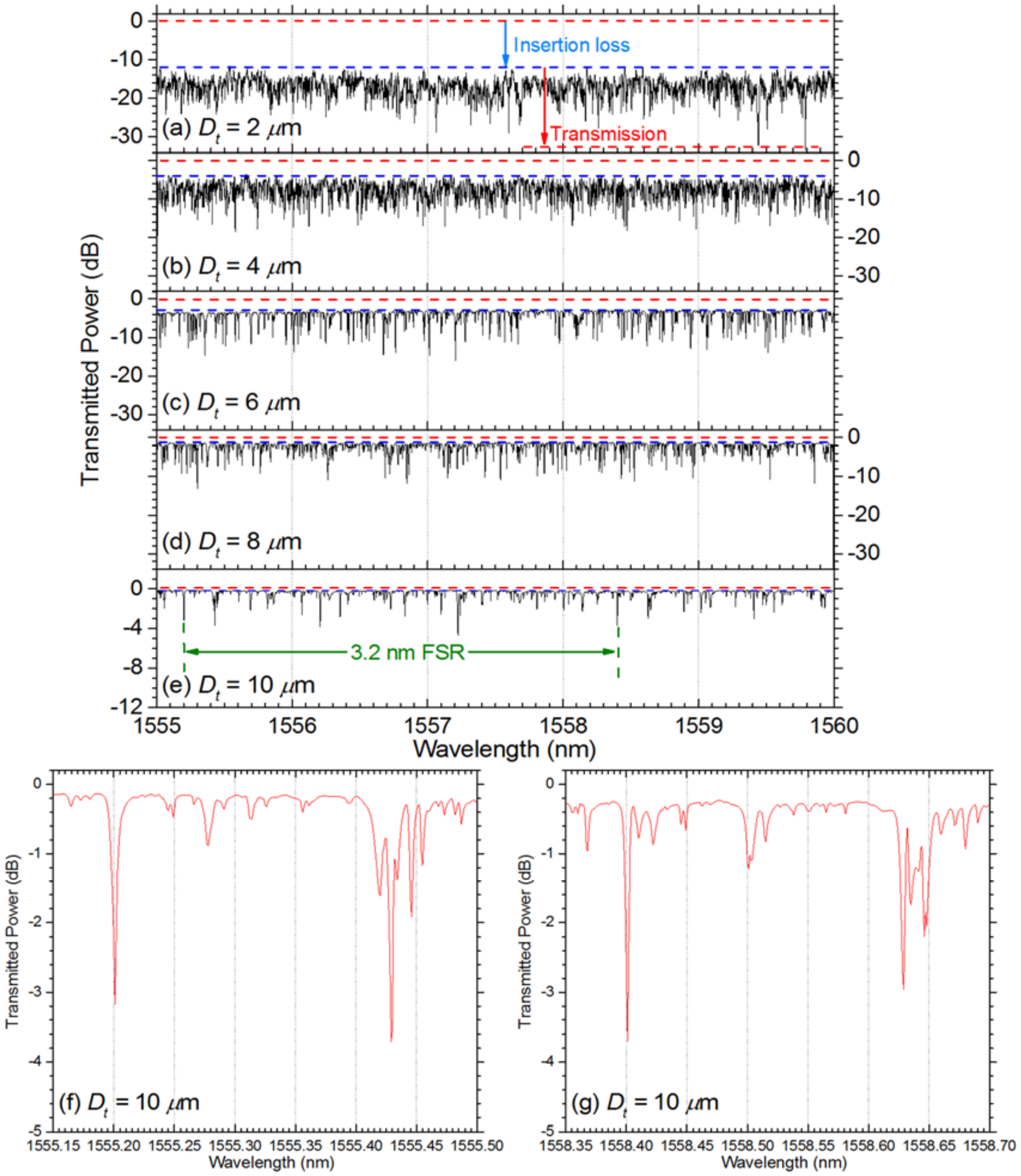

Figure 3.4 Transmission spectra of MBR WGM excited at the centre with microtapers of waist diameter D_t (a) 2, (b) 4, (c) 6, (d) 8 and (e) 10 μm. Figure 3.4 (f) and (g) Similar transmission spectra selected to determine the MBR FSR.

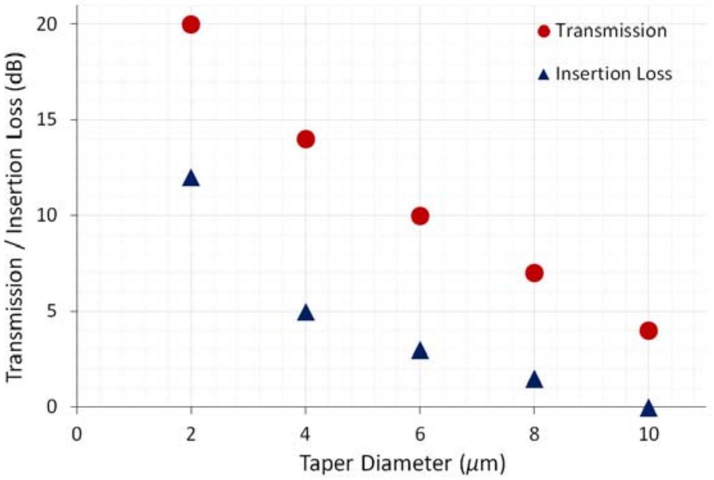

Figure 3.5 Summary of MBR transmission and insertion loss vs. taper D_t.

The observed reduction in the density of transmission resonances, i.e. spectrum clean-up, and the decrease in the transmission dips with the increase of the taper diameter is a result of the variation of the coupling strength between the propagating microtaper mode and the excited WGMs. In order to quantify the coupling effects, we have modified the theoretical analysis developed for microsphere excitation by microtapers [21,22]. In reference [21] a quasi-parabolic profile is considered to approximate the microsphere shape, and Hermite-Gauss functions are used to describe the axial (or polar) field distributions around the coupling point. These approximations are exact expressions for the shape and axial field distributions in quasi-parabolic profile MBRs and therefore the obtained coupling constants expressions are applicable to MBRs with higher accuracy. The required radial field distributions and MBR eigenfrequencies are given in terms of (*m,q,p*) in reference [11]. Figure 3.6 shows the effective index of the microtaper LP_{01} mode and MBR WGMs of different radial mode orders (p = 1, 2, 3, 4), as a function of the resonant wavelength. The effective indices for the taper LP_{01} mode and the WGMs are defined as β_{LP01}/k_0 and m/R_b, respectively, where β_{LP01} is propagation constant of the LP_{01} taper mode, k_0 is the vacuum wavenumber, m is the WGM azimuthal mode number and R_b is the MBR radius. It is shown that for D_t = 2 μm the effective index of the taper mode lies well within the WGM effective-index range and it is phase-matched with a large number of WGMs. It is, therefore, expected to strongly excite a large number of WGMs supported by the MBR. As D_t increases above the 4 μm level the taper mode gets progressively more detuned from the MBR WGMs.

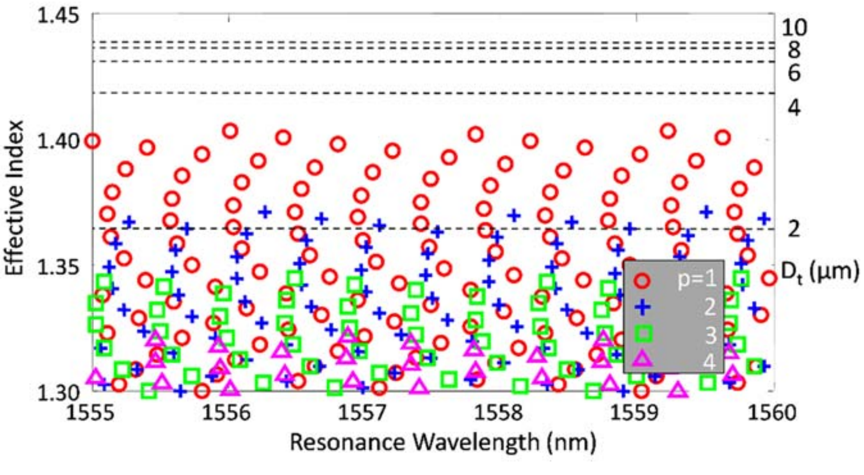

Figure 3.6 Effective index of the microtaper LP_{01} mode (D_t = 2, 4, 6, 8, & 10 μm) and MBR WGMs of different radial mode orders (p = 1, 2, 3, 4), as a function of the resonant wavelength.

The impact of the LP_{01} microtaper mode effective index variations are shown in figure 3.7, where the transmission minima are plotted as a function of the corresponding WGM resonance wavelength. The transmission minima are calculated using a simplified coupling approach, appropriate for generalized ring-resonators [22-24]. Figure 3.7 (a) and (b) show that for D_t = 2 μm and 4 μm, respectively, the transmission spectra are dense due to strong excitation of many different radial order WGMs. For D_t = 10 μm (figure 3.7 (c)), however, only the fundamental radial order (p = 1) WGMs are primarily excited and the calculated transmission spectrum is simplified substantially. In this case, the large phase mismatch between the microtaper LP_{01} mode and the MBR WGMs (see figure 3.6), and the decreased evanescent mode field overlaps result in smaller overall coupling constant and excitation strength and, therefore, reduced transmission dips. In figure 3.7 (c) the calculated WGM azimuthal and axial mode numbers are also shown. As expected, for a microtaper placed in the MBR centre, the strongest excitation corresponds to the fundamental WGM characterized by axial mode number q = 0. In this case, the calculated free spectral range (FSR) for modes with the same (p, q) mode numbers and adjacent azimuthal numbers, i.e. (m, q, p) = (476, 0, 1) and (m, q, p) = (475, 0, 1), is 3.15 nm, in close agreement with the experimental results (FSR_{exp} ≈ 3.2 nm – see figure 3.4 (e)).

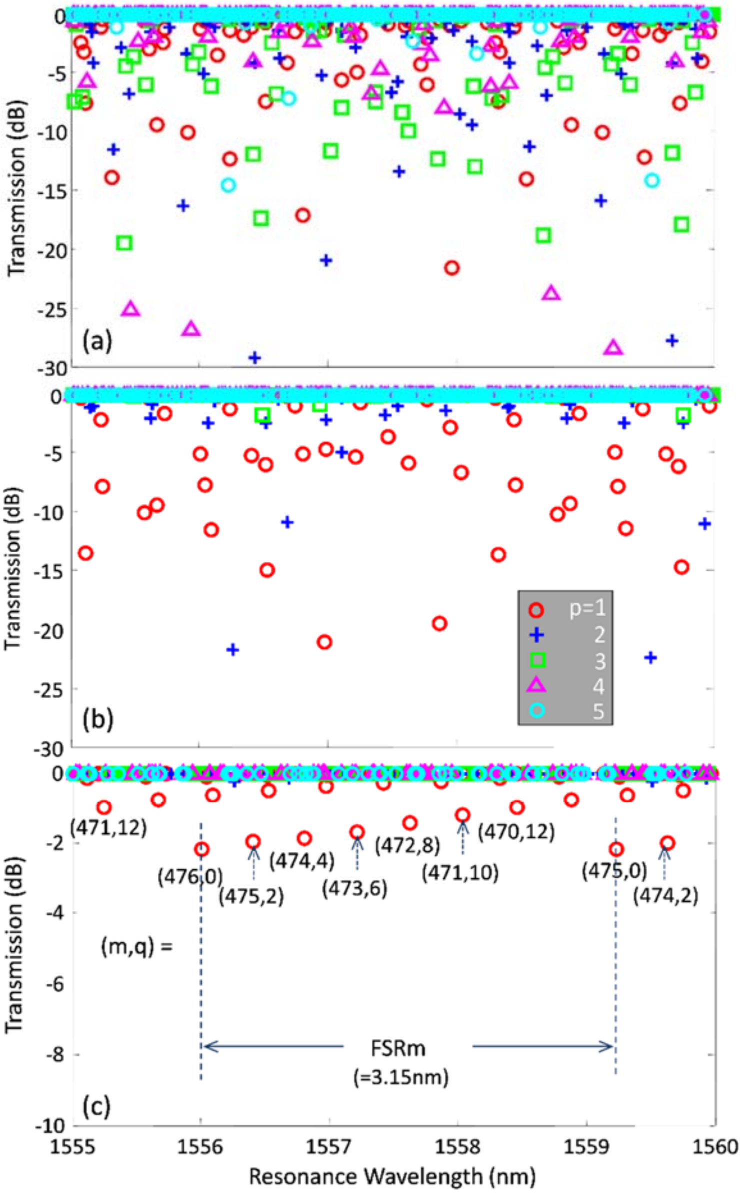

Figure 3.7 WGM transmission minima vs. corresponding resonance wavelength, for different radial mode orders (p = 1, 2, 3 ,4, 5), for microtaper diameter D_t of (a) 2 μm, (b) 4 μm and (c) 10 μm. (m, q are the WGM azimuthal and axial mode numbers, respectively).

It should be pointed out that WGMs with larger axial mode numbers show progressively smaller transmission dips, as a result of their larger axial spreading and smaller evanescent overlap with the microtaper LP_{01} mode. In addition, because of spatial mode symmetry, in the case of central excitation only the WGM modes with odd number of axial intensity maxima (i.e. even axial mode number q) are excited. In practice though, residual non-symmetries can result in excitation of both even and odd axial order WGMs, as it has been experimentally observed with offset excitation of slightly deformed microspheres [25]. This effect will be much more pronounced with the smaller diameter microtapers. Utilization of microtapers with $D_t = 10$ μm generated readily resolved single resonance dips which are easily distinguishable along with clearly identifiable FSR. These transmission dips can be beneficial as indication markers through any wavelength shifts in case MBRs are to be used in sensing applications [26]. In addition, we have noticed that a larger microtaper fibre waist diameter also results in a much more robust device showing negligible aging and deterioration towards environmental effects, such as humidity. Conversely, tapered fibres with 2 μm waist diameters deteriorate quickly resulting in a large surface scattering and a transmission power drop. Comparison of figure 3.4 (a) and (e) show that the use of a tapered fibre with $D_t = 10$ μm results in > 10 dB throughput power increase.

Figure 3.8 shows specific measured resonant features of the MBR excited at the centre with the five different tapered fibres of different D_t. The wavelength span is varied in order to best demonstrate the multiple overlapping resonance fitting and the observed dominant resonance Q-factor (approximated by $\lambda/\Delta\lambda$). The cumulative fitted and experimental curves are almost indistinguishable. As can be seen from the Lorentzian fitting, utilizing microtapers with $D_t \leq 6$ μm results in transmission features composed of a large number of overlapping WGM resonances. This is a direct consequence of the multiple radial-order WGM excitation discussed with reference to figure 3.7. When using microtapers with $D_t \geq 8$ μm the transmission features comprise predominantly single WGM resonances. As discussed above, our modelling attributes these resonances to radial order $p = 1$ WGMs. This could be of great advantage for applications where monitoring single WGM dip resonances is required over a broad wavelength range. While utilizing smaller microtaper fibre waist diameters provide increased coupling efficiency and stronger resonances, this is achieved at the expense of multiple higher-radial-order MBR mode excitation. However, it should be stressed that in all cases, the measured maximum Q-factor of the dominant resonance was > 10^6 for all microtaper waist diameters.

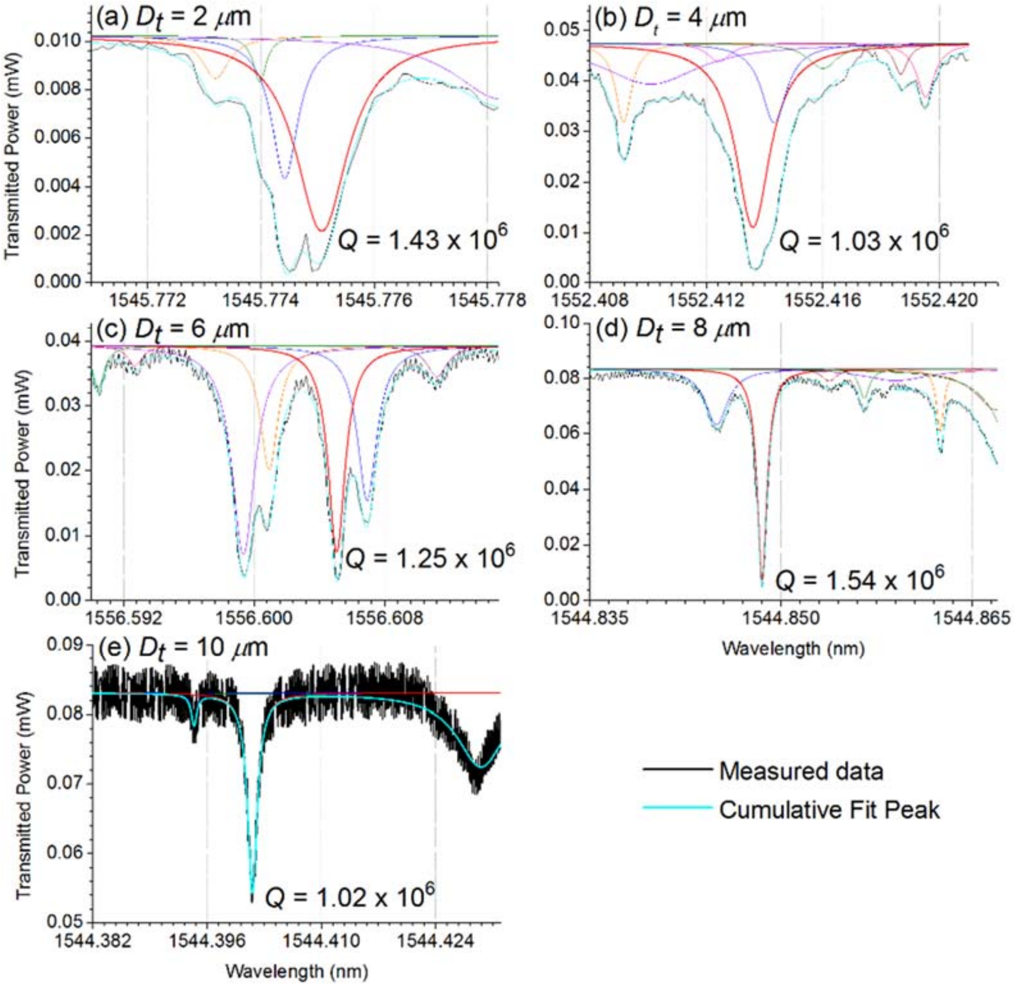

Figure 3.8 Lorentzian fitting and *Q*-factor values of MBR WGMs excited with tapered fibre of various D_t.

3.3 Tapered fibre modal transformation by microbottle resonator

Tapered fibres utilized for exciting the MBR under study were fabricated to have an adiabatic transition from full SMF 9/125 μm core/cladding diameter to the desired diameter with 6.0 mm uniform-waist length. For an adiabatic tapered fibre transition, high efficiency excitation of the LP_{01} fundamental fibre mode reaching 99.5% could be accomplished [27]. Although the tapered fibre supports a number of modes along its waist (where the original core diminishes and light is being guided by the clad/air interface), uniform-waist tapered fibres with adiabatic transition still maintain the LP_{01} mode excitation. Placing an optical microresonator in close proximity to the tapered fibre waist causes evanescent coupling. Two conditions must be met in order for energy transfer between the tapered fibre and the WGM to occur. The first is the wavelength of the LP_{01} taper mode must match a resonance wavelength, corresponding to a WGM of the microresonator. The second requires the coupling constant to match the microresonator WGM round trip losses for critical coupling and maximum power exchange. However, as we have seen, in the case of MBR more than one WGM can be excited simultaneously, albeit with different strengths. In a similar way, the energy back-transfer from an excited microresonator WGM can take place into many different microtaper fibre modes. Even the 2 μm waist microtaper supports ~5 LP modes at 1550 nm. In such case, the input LP_{01} mode is expected to be partially coupled into higher order waist modes after the MBR. In other words, the process of evanescently coupling into a microresonator can potentially transform the launched LP_{01} tapered mode. In this section, mode transformation at the output of the waist of a truncated microtaper are studied experimentally by monitoring the near-field images of the transmitted power, by scanning across WGM resonances. The near-field images were studied across the WGMs with high transmission dips as they are more likely to show energy back-transfer to the microtaper waist higher-order modes.

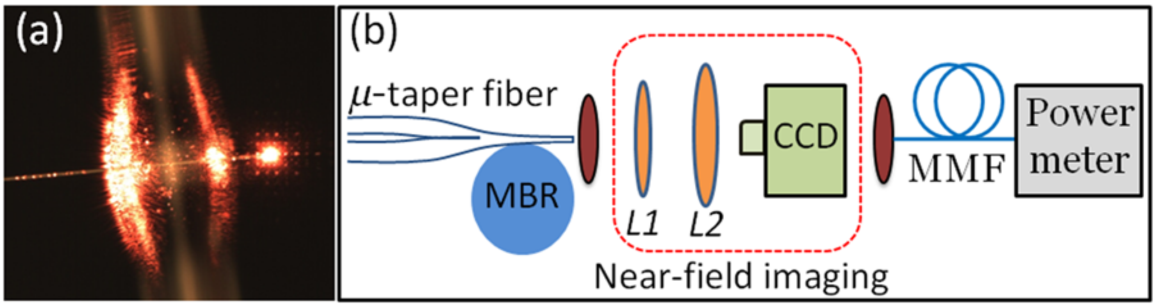

Figure 3.9 (a) MBR light scattering with microtaper fibre to a He-Ne laser. (b) Schematic of microtaper fibre near-field imaging experiment.

Investigation of modal transformation from an excited MBR back to the microtaper fibre was performed with the utilization of microtaper fibres of D_t = 2 and 8 μm. The microtaper fibres were cleaved at their respective minimum waist-regions and placed on top of the MBR as close as possible to their centre, in order to minimize any effect of vibration. Figure 3.9 (a) shows light scattering by the MBR with cleaved tapered fibre of D_t = 8 μm when its input end was connected to a He-Ne laser source. Schematic of the experimental setup for scanning the transmission spectra through the terminated tapered fibres and capturing the output beam near-field images is illustrated in figure 3.9 (b). For accurate near-field images across a WGM resonance, the output transmitted spectra were first scanned without the near-field imaging optical components (dashed-red box) set in the system. The input end of the tapered fibre was connected to a broadband CW-TLS and an objective lens with high NA (0.65) was aligned close to the taper cleaved end in order to collect the output light and collimate it through free-space. The light beam was then focused down by another high NA lens into a multi-mode fibre (MMF) and measured via an InGaAs optical power meter. Once the spectra of the excited MBR through the terminated microtaper fibre were acquired, optical components for capturing the output beam near-field images were placed in the system. For clear observation of modal transformations through the microtaper fibres, the collimated output beam was magnified 10X with the incorporation of two bi-convex lenses (*L1* and *L2*) before being directed into a CCD camera for image recording. In order to prevent image saturation on the CCD detector due to the high power going through the microtaper fibre, neutral density (ND) filters were placed in the lens barrel of the CCD camera.

Figure 3.10 illustrates the observed MBR modal transformation back into the terminated tapered fibre of one specific resonance using the finely tuned wavelength laser source with microtaper of D_t = 2 μm across the resonance centred at the wavelength of 1557.131 nm. Off-resonance (i.e. between 1557.110 – 1557.120 nm – images (a) & (b)), only the fundamental LP_{01} mode was observed. Around 1557.125 nm, there was a group of simultaneously excited WGMs. The near field image at this point shows that the output beam became slightly distorted– due to different modes beating (image (c)). Near 1557.128 nm (image (d)), the output beam started to lose power because of efficient light coupling into the cavity. At this strong resonance point, the TLS power was increased in order to have more light out of the microtaper for adequate image processing. The appearance of LP_{11} mode became much more significant past 1557.128 nm and tuning the wavelength further causes the LP_{11} mode to become predominant (images (e) – (h)). Modal transformation from LP_{01} to LP_{11} was clearly observed at the resonance transmission dip, which was near 1557.131 nm (image (i)). Again, away from the resonance (past 1557.133 nm), only the fundamental LP_{01} modes were observed (images (l) – (n)). With a few exceptions, most of the other strong WGM resonance checked showed noticeable LP_{11} mode excitation at their resonance wavelengths.

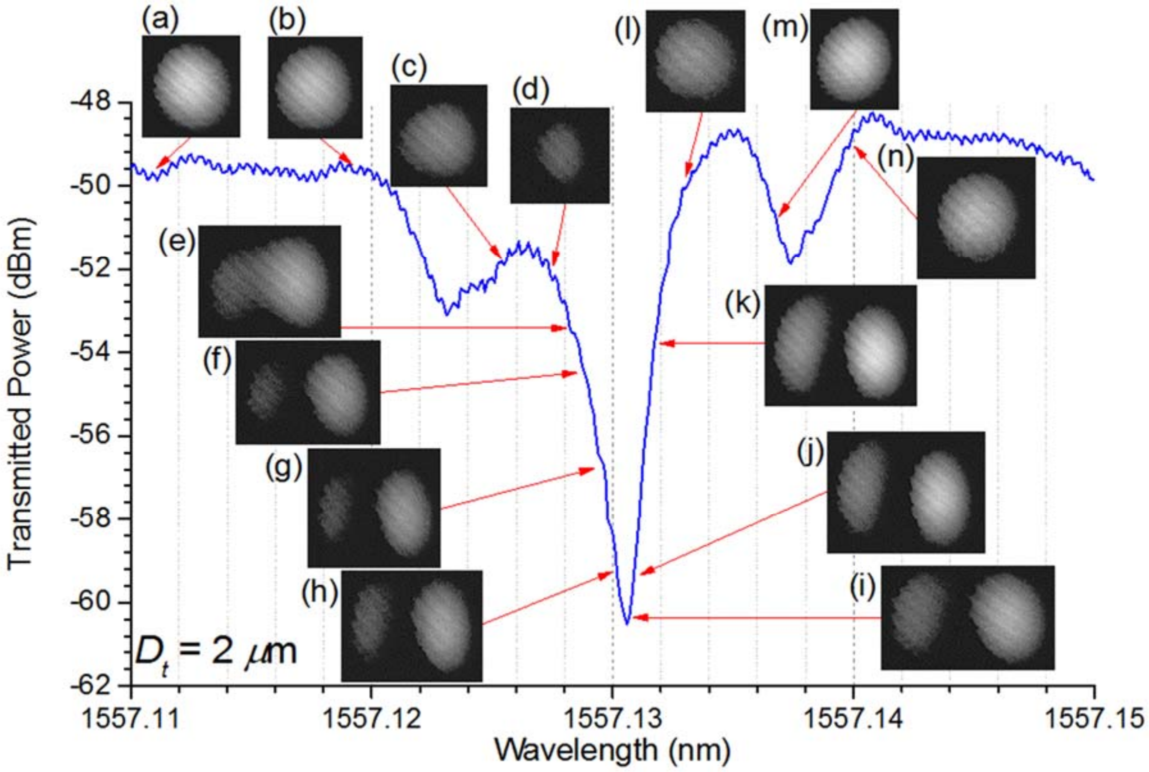

Figure 3.10 Near-field images from terminated microtaper fibre of D_t = 2 μm across a MBR WGM.

Exciting the MBR with a microtaper of D_t = 8 μm showed that only a small fraction of the WGM resonances result in a clear LP_{01} to LP_{11} modal transformation. Most of the stronger resonances only showed a slight distortion on the output beam image, indicating very small mode transformation. A large number of the checked resonances did not show any noticeable LP_{11} excitation.

Nevertheless, as shown in figure 3.11, the few resonances which did show clear modal transformation follow the same trend as with the previous microtaper with smaller waist diameter.

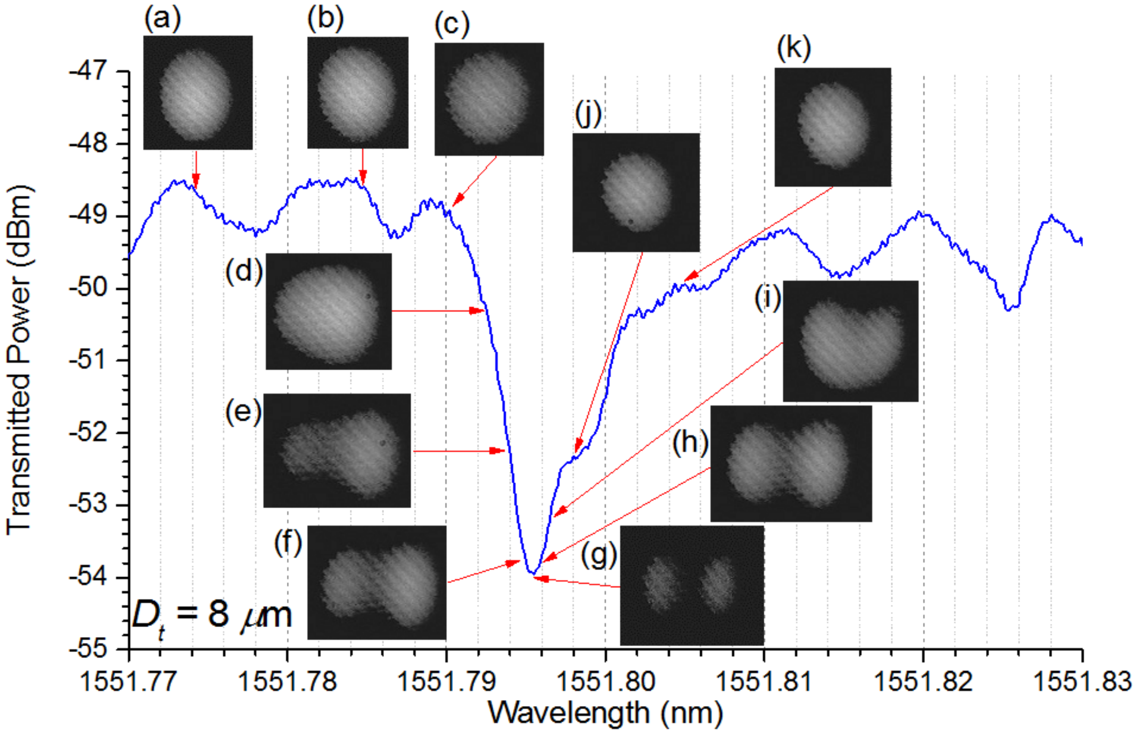

Figure 3.11 Near-field images from terminated microtaper fibre of D_t = 8 μm across a MBR WGM.

It could be observed from figure 3.10 and 3.11 that periodic "fringes" appeared on the recorded near-field images captured from the taper cleaved end. In order to understand the cause of this phenomenon, near-field images from SMF were studied in detail. Figure 3.12 (a) shows a near-field image from an SMF cleaved end without any magnification set-up. Noticeable periodic "fringes" appeared on the recorded near-field image. Figure 3.12 (b) shows that with 10X magnification, the periodic "fringes" on the near-field images appeared to be more acute. From observation, it can be determined that the periodic "fringes" appeared because of small amount of light was being reflected back and forth between two points of mirrors in the set-up. In the case without any magnification, light reflections originated from the ND filters placed in the barrel of the CCD camera. With 10X magnification image recording, more reflection points were introduced into the system with the utilization of the two bi-convex lenses (*L1 and L2*) set-up as the telescope.

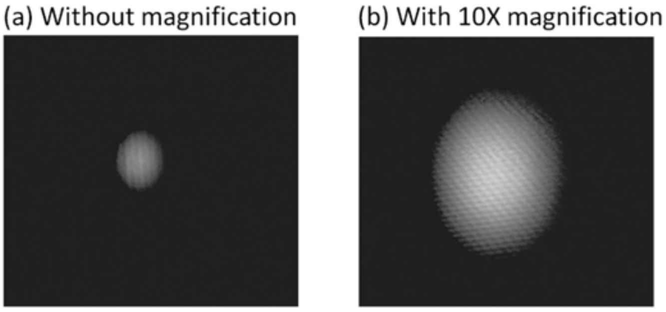
(a) Without magnification
(b) With 10X magnification

Figure 3.12 Near field images from an SMF cleaved end (a) without, and (b) with 10X magnification.

It had been previously reported that coupling 'ideality' from a microresonator back to the desired mode of microtaper fibres would decrease as D_t increases [28]. From this study, however, strong LP_{01} to LP_{11} modal transformations were observed more frequently on the smaller waist diameter microtaper fibres. Despite the fact that larger waist diameter tapered fibres support a much larger number of modes, the observed modal transformation was significantly smaller and less frequent. The conclusion in reference [28] was based entirely on microtaper modality arguments. However, mode excitation depends on evanescent field overlaps and phase-matching, which both decrease as the microtaper waist diameter increases. This implies that modal phase-matching, rather than the number of supported modes, defines the degree of modal transformation in an evanescently coupled microresonator. As shown in figure 3.13, in the case of $D_t = 2\ \mu m$ the effective indices of LP_{01} and LP_{11} lie well within the effective index range of WGM of different overlapping radial orders, making the $LP_{01} \rightarrow WGM_{mpq} \rightarrow LP_{01}$ and $LP_{01} \rightarrow WGM_{mpq} \rightarrow LP_{11}$ coupling feasible. However, due to its larger evanescent field extension into the MBR, the LP_{11} mode shows stronger overlap with the WGM_{mpq} and the $LP_{01} \rightarrow WGM_{mpq} \rightarrow LP_{11}$ transformation is dominant. Similar preferential excitation of LP_{11} mode has been observed in other coupled optical systems [29]. In the case of $D_t = 8\ \mu m$, on the other hand, the effective indices of both LP_{01} and LP_{11} are close together and highly mismatched with the radial order p = 1 family of WGMs and, therefore, the $LP_{01} \rightarrow WGM_{mpq} \rightarrow LP_{11}$ mode transformation is not favoured.

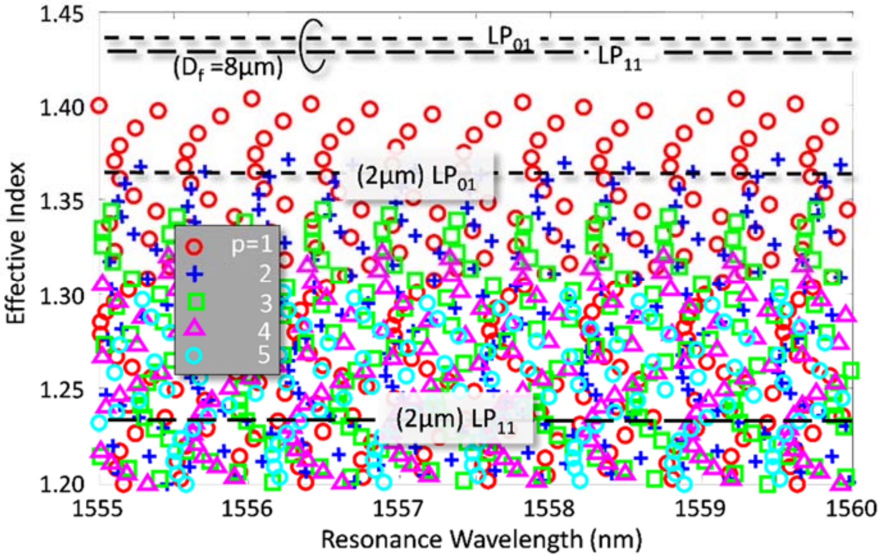

Figure 3.13 Effective index of the microtaper LP_{01} & LP_{11} mode (D_t = 2 & 8 μm) and MBR WGMs of different radial mode orders (p = 1, 2, 3, 4, 5), as a function of the resonant wavelength.

Finally, it should be stressed that in the case of full tapered excitation fibre and resonant $LP_{01} \rightarrow WGM_{mpq} \rightarrow LP_{11}$ (or other higher order mode) mode transformation, the LP_{11} (or higher order) mode will be gradually turn into a cladding mode in the up-taper region of the excitation fibre and be lost. In this case, the mode transformation and subsequent loss will appear as an apparent increased transmission dip and stronger resonance. This effect should be considered when the size of the experimentally obtained transmission dip and resonance wavelength are used to extract information about the MR parameters, such as losses or coupling strength.

3.4 FDTD modal simulations

In order to get additional physical insight, the modal transformation on a waveguide as it excites a WGM microresonator was simulated by utilizing a finite difference time domain (FDTD) software package [30]. The simulation was performed in a 2-D environment with smaller component dimensions relative to the experimental work in order to minimize the required memory size and the run time. The waveguide under study has a 0.7 μm-wide core with length of 16 μm. The waveguide was in contact with a microdisc resonator of radius 7 μm. The waveguide and microdisc refractive index was 1.5 and the background refractive index value was set to 1.0. In order to avoid any back-reflections from the computed windows, perfectly-matched layers were set on the boundaries. The waveguide was two-moded around λ = 1 μm. A TM-fundamental mode pulse was launched from one end of the waveguide with a power monitor placed at the other. The pulse sent into the waveguide core was of Gaussian-shape and centred at 1 μm wavelength to calculate the transmission spectrum of the coupled waveguide/microdisc structure. Figure 3.14 examines a specific whispering-gallery resonance of the microdisc.

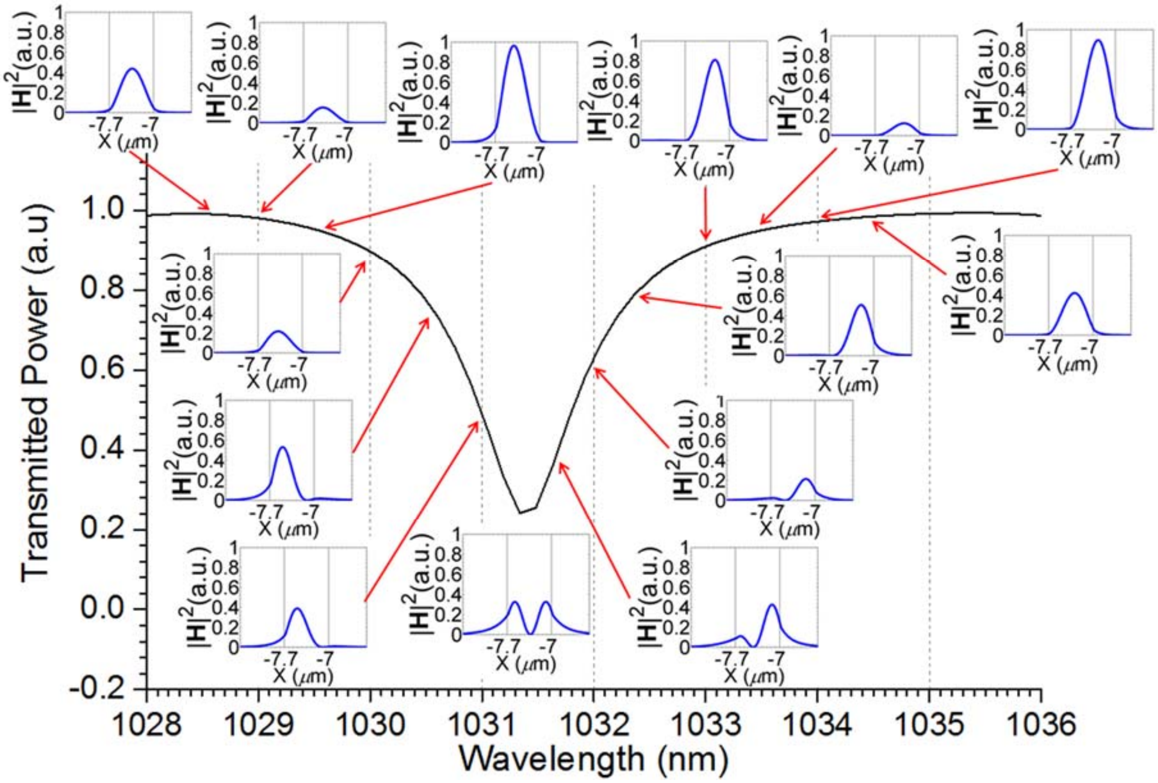

Figure 3.14 FDTD simulation **H**-field intensity patterns across a microdisc WGM near the waveguide output end.

The insets of figure 3.14 show the magnetic **H**-field intensity patterns across the waveguide near the output end. Away from resonance (wavelength range 1028.5 – 1030.0 nm), a high portion of the launched power remains in the waveguide fundamental TM_0 mode. Getting closer to the WGM resonance (λ > 1030.5 nm) the output intensity patterns started showing excitations of the waveguide TM_1 mode. At the precise microdisc resonance wavelength of 1031.338 nm, the output **H**-field intensity pattern shows a clear TM_1 mode transformation. For longer wavelengths, the **H**-field patterns consist of two modes travelling through the waveguide. For wavelengths λ > 1033.5 nm, only TM_0 modes were observed at the output of the waveguide. The FDTD simulation performed on a microdisc resonator shows similar trends of energy back-transfer to the waveguide as observed in the MBR experiment.

Figure 3.15 plots the steady-state **H**-field distribution within the waveguide and the WGM microdisc resonator at off-resonance wavelength of 1028.500 nm and figure 3.16 plots the steady-state **H**-field distribution within the waveguide and the WGM microdisc resonator at on-resonance wavelength of 1031.388 nm. A clear mode transformation is observed when power is coupled from the resonator back into the coupled waveguide at resonance.

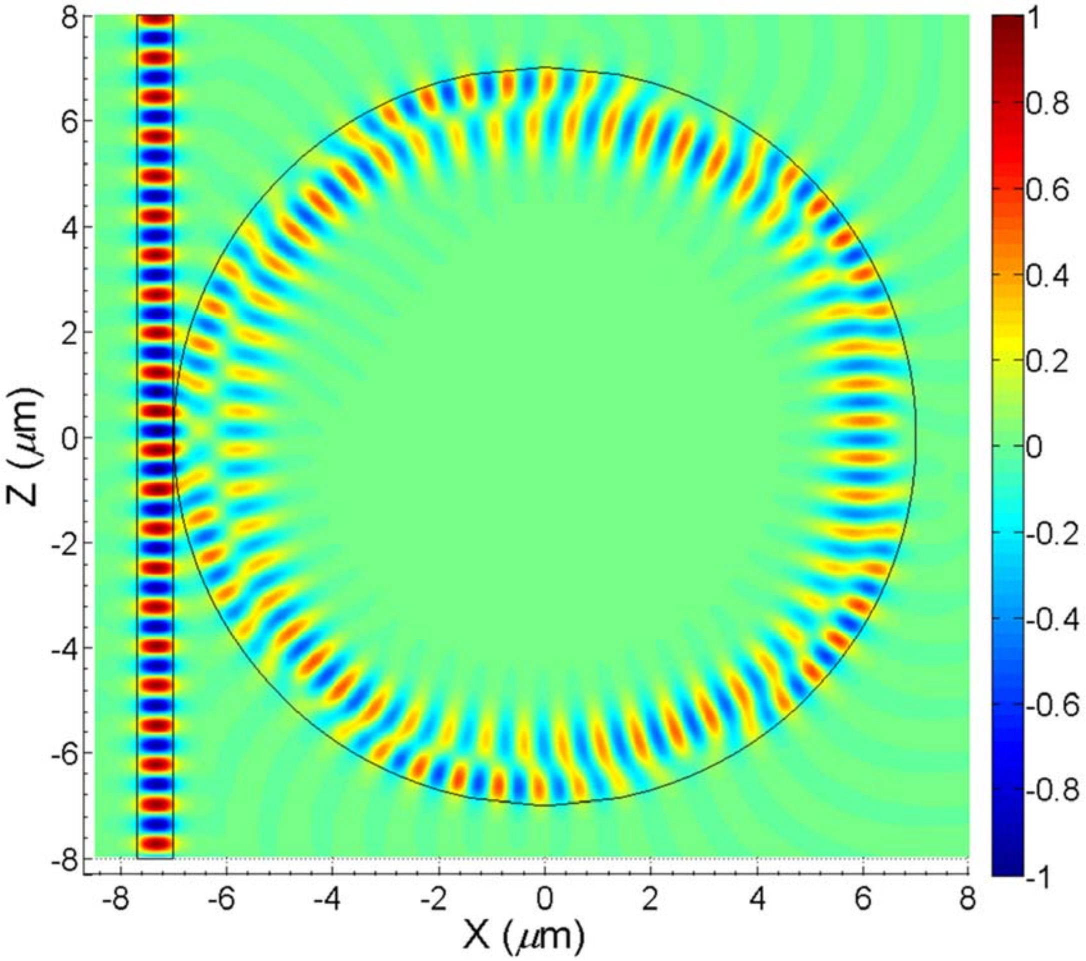

Figure 3.15 FDTD steady-state **H**-field distribution within waveguide and WGM microdisc at off-resonance wavelength of 1028.500 nm

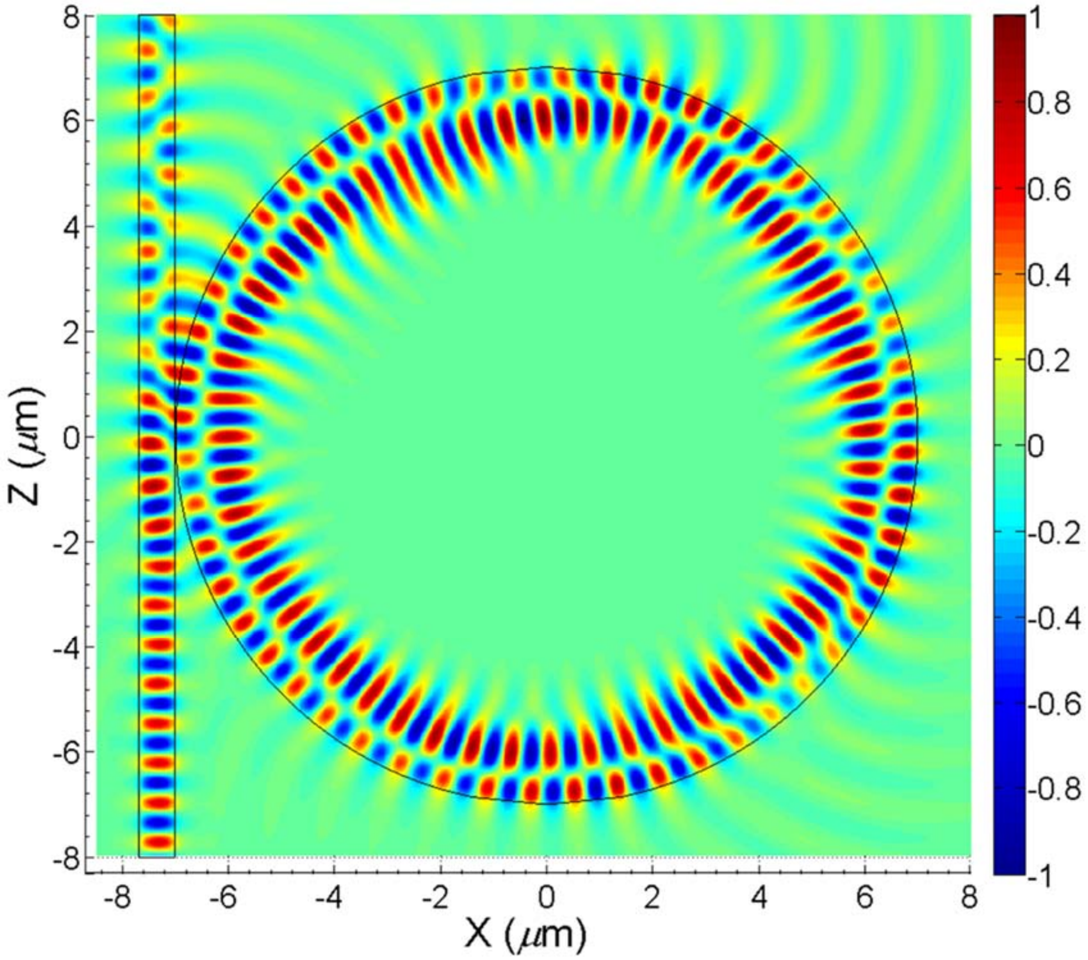

Figure 3.16 FDTD steady-state **H**-field distribution within waveguide and WGM microdisc at on-resonance wavelength of 1031.388 nm.

3.5 Summary

In this chapter, the systematic study of the effect of the microtaper fibre diameter (D_t) on the MBR transmission spectrum characteristics was carried out both experimentally and theoretically. Progressively cleaner and simpler spectra were obtained when D_t was increased from 2 μm to 10 μm. Microtaper waist diameters were shown to have little influence on the loaded *Q*-factor value of the MBR. The measured *Q*-factor with microtapers of different D_t were observed to reach values > 10^6 in all cases. The utilization of tapered fibres with relatively larger waist diameters (> 6 μm) was observed to increase the transmitted power and generate much simpler spectra, due to excitation of lower-radial-order MBR WGMs, albeit of reduced strength. These features could be beneficial as indication markers when MBRs are intended for sensing purposes [26]. The transmitted power can also be increased in the case of thin microtapers, when the gap between taper and microresonator is accurately controlled [31]. The effect of the microtaper diameter on the MBR transmission spectra were also calculated, showing a good agreement with the experimental results.

Mode transformation as a result of light coupling from MBR back to the microtaper fibre was studied. It was observed that conversion of the LP_{01} tapered fibre mode into LP_{11} takes place in a number of strong transmission resonances in the case of 2 μm taper waist diameters. Despite the much larger modality, and contrary to initial expectations [28], modal transformation was observed to be not as frequent in the case of microtaper with 8 μm waist diameters. In this case only a small fraction of the observed resonances showed clear modal transformation from a lower order to a higher order. Using calculations based on a newly developed theoretical model, we demonstrated that modal phase-matching between WGMs and microtaper LP modes, rather than the number of supported LP modes defines the degree of modal transformation and coupling "ideality" in an evanescently coupled microresonator. Hence there is no major concern of increased coupling losses from lower order to higher order modes on MBRs with the utilization of microtaper fibres of larger D_t. FDTD simulation on a microdisc resonator provided extra physical insight and shows similar energy back-transfer trend to the waveguide as its **H**-field strengths were scanned across a WGM resonance.

3.6 References

[1] K. J. Vahala, “Optical microcavities,” *Nature* **424**, 839 (2003).

[2] V. S. Ilchenko and A. B. Matsko, “Optical Resonators with Whispering-Gallery Modes–Part II: Applications,” *IEEE Journal of Selected Topics in Quantum Electronics* **12**, 15 (2006).

[3] M. L. Gorodetsky, A. A. Savchenkov, and V. S. Ilchenko, “Ultimate Q of optical microsphere resonators,” *Optics Letters* **12**, 182 (2000).

[4] D. K. Armani, T. J. Kippenberg, S. M. Spillane, and K. J. Vahala, “Ultra-high-Q toroid microcavity on a chip,” *Nature* **421**, 925 (2003).

[5] B. E. Little, J. S. Foresi, G. Steinmeyer, E. R. Thoen, S. T. Chu, H. A. Haus, E. P. Ippen, L. C. Kimerling, and W. Greene, “Ultra-compact Si-SiO2 microring resonator optical channel dropping filters,” *IEEE Photonics Technology Letters* **10**, 549 (1998).

[6] T. A. Birks, J. C. Knight and T. E. Dimmick, "High-resolution measurement of the fiber diameter variations using whispering gallery modes and no optical alignment," *IEEE Photonics Technology Letters* **12**, 182 (2000).

[7] V. S. Ilchenko, M. L. Gorodetsky, X. S. Yao, and L. Maleki, “Microtorus: a high-finesse microcavity with whispering-gallery modes,” *Optics Letters* **26**, 256 (2001).

[8] M. Sumetsky, Y. Dulashko, and R. S. Windeler, “Optical microbubble resonator,” *Optics Letters* **35**, 898 (2010).

[9] M. Sumetsky, “Whispering-gallery-bottle-microcavities: the three dimensional etalon,” *Optics Letters* **29**, 8 (2004).

[10] G. S. Murugan, J. S. Wilkinson, and M. N. Zervas, “Selective excitation of whispering gallery modes in a novel bottle microresonator,” *Optics Express* **17**, 11916 (2009).

[11] G. S. Murugan, M. N. Petrovich, Y. Jung, J. S. Wilkinson, and M. N. Zervas, “Hollow-bottle optical microresonators,” *Optics Express* **19**, 20773 (2011).

[12] G. S. Murugan, J. S. Wilkinson, and M. N. Zervas, "Optical excitation and probing of whispering gallery modes in bottle microresonators: potential for all-fiber add–drop filters," *Optics Letters* **35**, 1893 (2010).

[13] M. Sumetsky and J. M. Fini, “Surface nanoscale axial photonics,” *Optics Express* **19**, 26470 (2011).

[14] M. Ding, G. S. Murugan, G. Brambilla, and M. N. Zervas, “Whispering gallery mode selection in optical bottle microresonators,” *Applied Physics Letters* **100**, 081108 (2012).

[15] V. B. Braginsky, M. L. Gorodetsky, and V. S. Ilchenko, “Quality-factor and nonlinear properties of optical whispering-gallery modes,” *Physics Letters A* **137**, 393 (1989).

[16] M. L. Gorodetsky and V. S. Ilchenko, “Optical microsphere resonators: optimal coupling to high-Q whispering gallery modes,” *Journal of Optical Society America B* **16**, 147 (1999).

[17] V. S. Ilchenko, X. S. Yao, and L. Maleki, “Pigtailing the high-Q microsphere cavity: a simple fiber coupler for optical whispering-gallery modes,” *Optics Letters* **24**, 723 (1999).

[18] L. Arques, A. Carrascosa, V. Zamora, A. Díez, J. L. Cruz, and M. V. Andrés, “Excitation and interrogation of whispering-gallery modes in optical microresonators using a single fused-tapered fiber tip,” *Optics Letters* **36**, 3452 (2011).

[19] J. C. Knight, G. Cheung, F. Jacques, and T. A. Birks, “Phase-matched excitation of whispering-gallery-mode resonances by a fiber taper,” *Optics Letters* **22**, 1129 (1997).

[20] O. Svitelskiy, Y. Li, A. Darafsheh, M. Sumetsky, D. Carnegie, E. Rafailov, and V. S. Astratov, “Fiber coupling to BaTiO3 glass microspheres in an aqueous environment,” *Optics Letters* **36**, 2862 (2011).

[21] B. E. Little, J. P. Laine and H. A. Haus, "Analytic theory of coupling from tapered fibers and half-blocks into microsphere resonators," *Journal of Lightwave Technology* **17**, 704 (1999).

[22] Y. Panitchob, G.Senthil Murugan, M. N. Zervas, P. Horak, S. Berneschi, S. Pelli, G. Nunzi Conti, and J. S. Wilkinson, "Whispering gallery mode spectra of channel waveguide coupled microspheres," *Optics Express* **16**, 11076 (2008).

[23] M. N. Zervas, “Transmission resonance modelling in microbottle resonators,"” under preparation.

[24] A. Yariv, "Universal relations for coupling of optical power between microresonators and dielectric waveguides," *Electronics Letters* **36**, 321 (2000).

[25] G. Lin, B. Qian, F. Orucevic, Y. Candela, J.-B. Jager, Z. Cai, V. Lefèvre-Seguin, and J. Hare, “Excitation mapping of whispering gallery modes in silica microcavities”, *Optics Letters* **35**, 583 (2010).

[26] M. N. Mohd Nasir, G. S. Murugan, and M. N. Zervas, “Broadly Tunable Solid Microbottle Resonator,” submitted to 2016 *IEEE Photonics Conference (IPC)*, Hawaii USA.

[27] J. Villatoro, D. Monzón-Hernández, and E. Mejía, “Fabrication and modeling of uniform-waist single-mode tapered optical fiber sensors,” *Applied Optics* **42**, 2278 (2003).

[28] S. M. Spillane, T. J. Kippenberg, O. J. Painter, and K. J. Vahala, “Ideality in a Fiber-Taper-Coupled Microresonator System for Application to Cavity Quantum Electrodynamics,” *Physical Review Letters* **91**, 043902 (2003).

[29] S. Barcelos, M. N. Zervas and P. S. J. Russell, "Selective excitation of fiber-modes using surface plasmons," *IEEE Photonics Technology Letters* **9**, 1051 (1995).

[30] RSoft Design Group, Rsoft Inc., FullWAVE 6.0 (2008).

[31] M. Cai, O. Painter, and K. J. Vahala, “Observation of Critical Coupling in a Fiber Taper to a Silica-Microsphere Whispering-Gallery Mode System,” *Physical Review Letters* **85**, 74 (2000).

Chapter 4: Whispering gallery modes microbottle resonators with periodic micro-scars

4.1 Introduction

Optical microresonators with high *Q*-factors show great potential to be incorporated into high-performance optical device applications [1]. However, most of WGM microresonator studies concentrated in areas of on-chip integration as they can be easily handled [2-5]. Nonetheless the capacity of these microresonators should not be limited only to on-chip devices as they hold limitless possibilities for application in other areas as well. It is acknowledged that geometrical shapes of these microresonators do restrict their handling and hence their utilization for other specific purposes. Recognizing this, much studies have been done in recent years to expand further the scope of WGM microresonators, especially through the cooperation of optical fibres [6-8]. A particular type of microresonator developed in optical fibres which support unique features of WGM are the microbottle resonators (MBRs) [9-11]. The structure of this unique microresonator resembles a strongly prolate microsphere where confinement of light in the cavity is made possible through the combination of whispering gallery-ring and whispering-gallery bouncing ball principle [9]. It has been reported that a variation of the fibre radius in the nano-scale is sufficient to create a quantum well for MBRs to trap any excited WGMs [12]. Such distinctive structures in MBRs permit to support highly non-degenerate WGMs which in turn grant access to rich a variety of excitable modes. Although the dense spectral feature of MBRs is beneficial for certain research area of studies (i.e. cavity-QED) [1], it is a major issue in any other application where monitoring the spectral feature of WGM resonances is required over a broad range; i.e. sensing. A few methods in reducing the complex features of MBRs have been previously proposed [13-15] and while they managed to considerably decrease the number of resonating modes, it is still preferable to lessen the excited modes of MBRs to the smallest possible number.

In this chapter, experimental demonstrations in simplifying the dense and complex features of MBRs through the inscription of periodic micro-scars are presented. Section 4.2 describes the fabrication technique utilized in milling the MBRs with periodic micro-scars. Initial measurement presented in section 4.3 shows clear spectral “clean-up” of the scarred MBRs along with their *Q*-factor measurement values. In section 4.4, polarization-resolved measurements on the scarred MBRs are presented with distinguishable single resonance peak excitation generated over a broad wavelength range. In section 4.5, finite-difference time domain (FDTD) simulation performed on a microdisc adds additional physical insight to the effects of periodic micro-scars on a whispering-gallery resonator.

4.2 Fabrication of microbottle resonators with periodic micro-scars through focused ion-beam milling

Using conventional SMFs, two MBRs that were fabricated through "soften-and-compress" technique [11] were utilized for the experiment. MBR1 has a maximum diameter D_b of 171 μm and neck-to-neck bottle length L_b of 292 μm. MBR2 has D_b of 185 μm and L_b of 300 μm. A focused ion-beam (FIB) milling technique was applied on the MBRs in order to produce periodic micro-scars on their surface. In order to make the surface of the MBRs conductive for ion milling process, a thin layer of gold of (~ 30 nm) was deposited on their surface. FIB attains the same principle as a scanning electron microscope (SEM) except that instead of rasterizing electrons on the surface of the samples, ions were used instead. However, this is inherently a destructive process. In the utilized FIB system, finely focused beam of gallium ions were operated at low beam currents for imaging with low sample surface destruction. Setting the gallium ions with high current would result in sputtering and milling on the contact surface of the samples through surface-destruction with precision of < 50 nm. Figure 4.1 (a) shows the whole gold-coated MBR1 after the milling process. Figure 4.1 (b) and (c) show the zoomed-in image of the milled section. MBR1 was inscribed with 11 micro-scars of 142 nm maximum width, 1.9 μm length, 2.5 μm pitch and 6 μm depth along the resonator axial path.

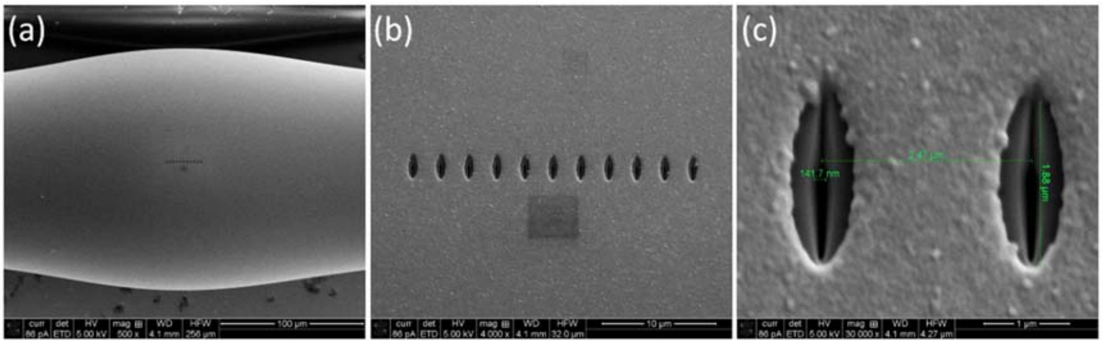

Figure 4.1 (a) Image of the milled MBR1, (b) zoomed-in image of the 11 periodic micro-scars and (c) parameters of the inscribed micro-scars.

For MBR2, 21 micro-scars were inscribed on the surface of the resonator along its azimuthal path with 340 nm maximum width, 10 μm length, 1.5 μm pitch and 6 μm depth. Figure 4.2 (a) shows the whole gold-coated MBR2 after the milling process. Figure 4.2 (b) shows the 21 periodic micro-scars with (c) its parameters.

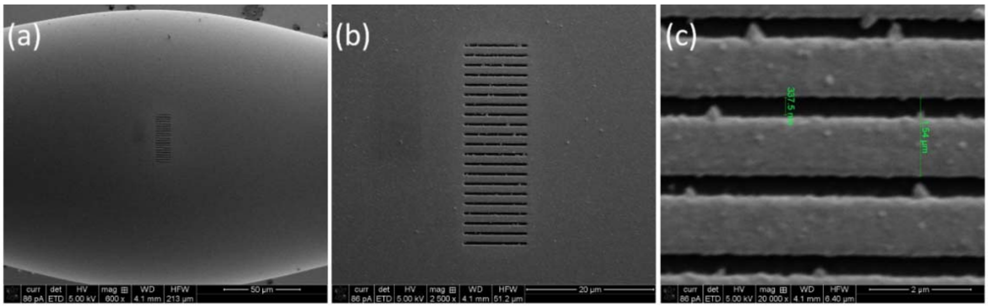

Figure 4.2 (a) Image of the milled MBR2, (b) zoomed-in image of the 21 periodic micro-scars and (c) parameters of the inscribed micro-scars.

The FIB milling process was not able to maintain the same width at the bottom point of inscription relative to the MBR surface due to the way it removes the dielectric material out. Thus each micro-scar has a v-shaped profile as it tunnels in the direction of MBR the core.

4.3 Characterization of the whispering-gallery microbottle resonators with periodic micro-scars

Gold coating on the surface of the MBRs was first removed by acid etching before the optical characterization. Tapered optical fibre of 2 μm waist diameter was used to evanescently couple light [16] from a broadly tunable laser source (TLS) into the MBRs under study. The tapered fibre was arranged to be in direct physical contact with the MBR while its other end having 125 μm diameter was used to monitor the transmitted power.

4.3.1 Excitation of whispering-gallery modes in MBR1

For the best demonstration of spectral simplification, MBR1 with the periodic micro-scars inscribed, was coupled with the tapered optical fibre 85 μm away off the resonator centre. Figure 4.3 shows (a) the excitation arrangement of MBR1 and (b) the scattered light captured using a CCD camera.

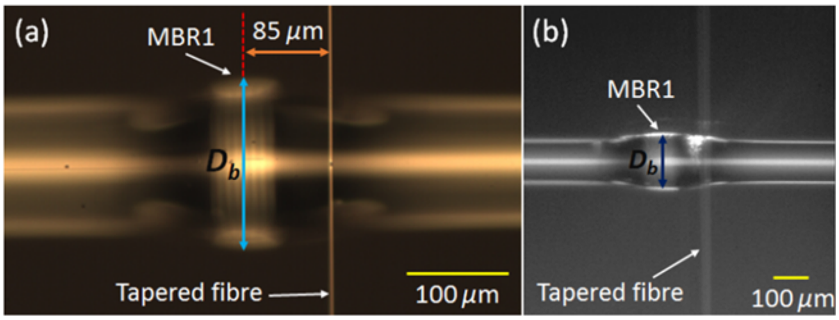

Figure 4.3 MBR1 (a) tapered fibre excitation arrangement and, (b) scattered light through the CCD camera.

Figure 4.4 shows the transmitted WGM spectra of MBR1 (a) without and (b) with periodic micro-scars inscribed along its axial path when excited 85 μm away from centre. The initial WGM profile of MBR1 shows a dense and complex WGM spectrum with indistinguishable family group-modes of

~10 dB maximum transmission dip. With the inscription of periodic micro-scars, a much simpler WGM resonance spectrum with distinguishable family group-modes was generated by the resonator with a maximum transmission dip of ~7 dB near the 1549.3 nm wavelength.

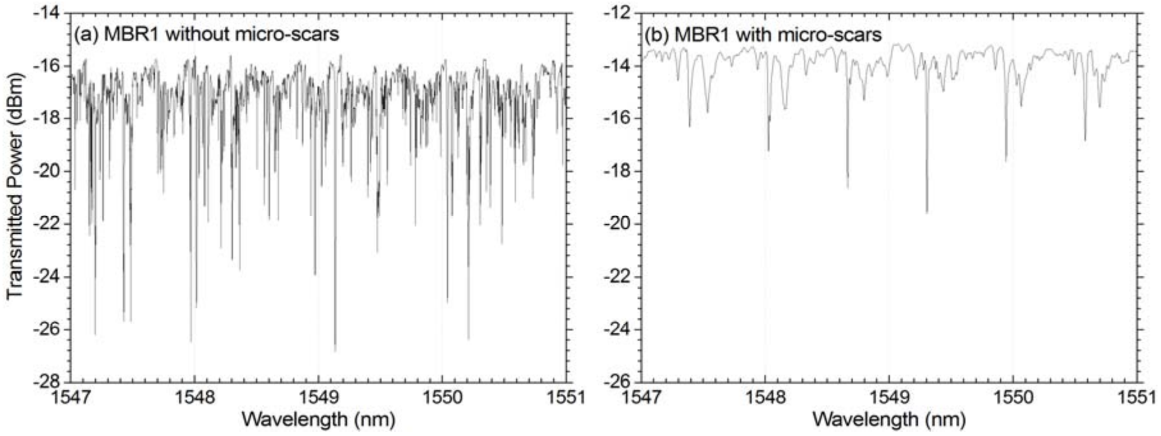

Figure 4.4 WGM spectra of MBR1 excited 85 μm off-centre (a) without and (b) with periodic micro-scars.

Q-factor values had not been affected much with the inscription of 11 periodic micro-scars on MBR1. Figure 4.5 shows the calculated *Q*-factor of MBR1, indicated by the red line, (a) & (b) without and (c) & (d) with micro-scars inscribed. Lorentzian fitting performed on the transmitted power of MBR1 shows a maximum *Q*-factor value of up to 10^5 being retained after the FIB milling process.

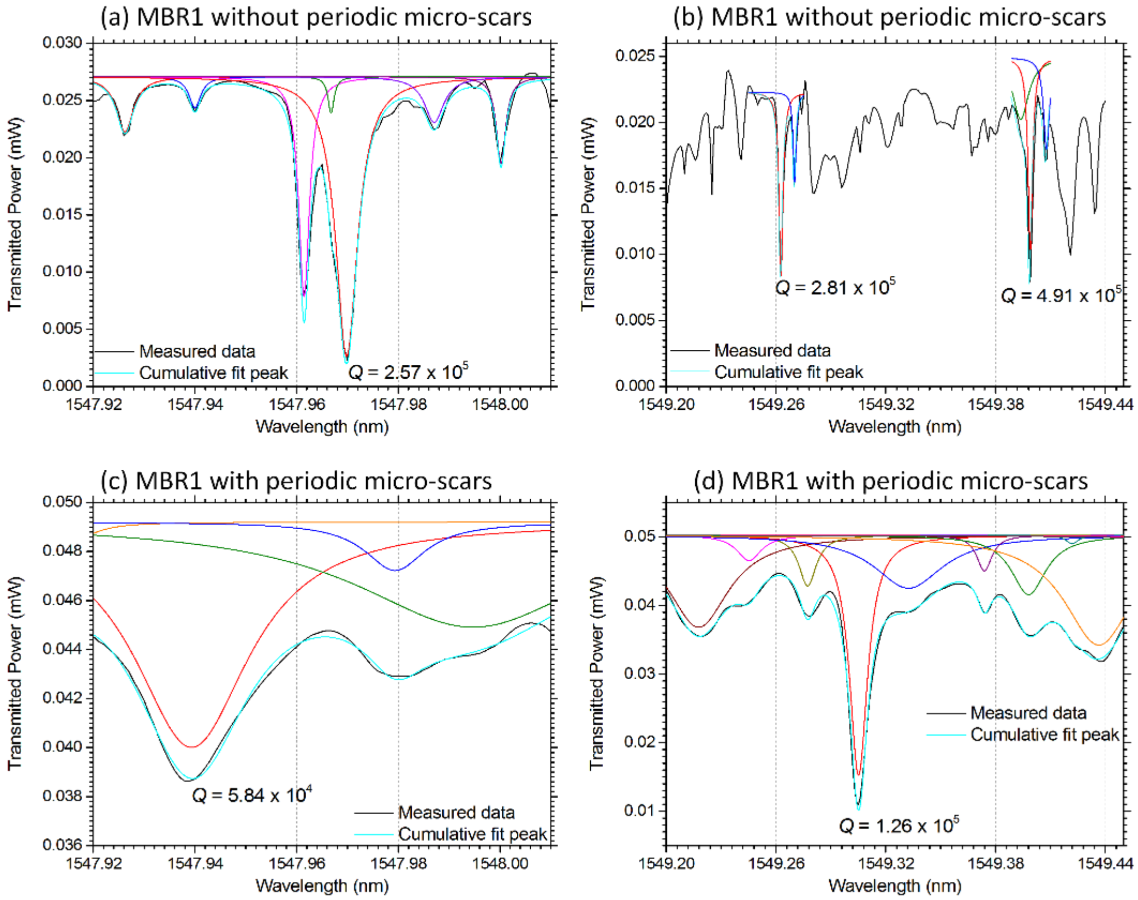

Figure 4.5 Transmitted Lorentzian fitting of MBR1 spectra (a) & (b) without, and (c) & (d) with the inscription of 11 periodic micro-scars.

4.3.2 Excitation of whispering-gallery modes in MBR2

Excitation arrangement for MBR2 was performed near the bottle's neck, i.e. the tapered fibre was coupled 127 μm away from the resonator's centre position. Figure 4.6 shows (a) the excitation arrangement of MBR2 and (b) the scattered light captured using a CCD camera.

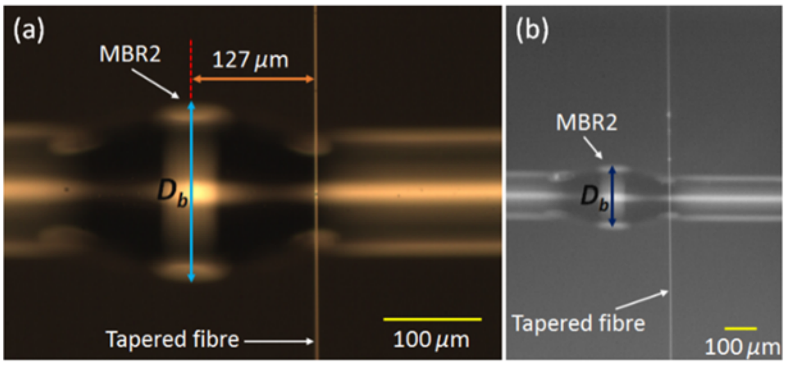

Figure 4.6 MBR2 (a) tapered fibre excitation arrangement and, (b) scattered light through CCD camera.

Excited WGM spectra of MBR2 without and with periodic micro-scars inscribed along its azimuthal path are shown in figure 4.7 (a) and (b) respectively. Simpler WGM spectra along with distinguishable single peak resonances were generated by the bottle resonator with the introduction of the periodic micro-scars on its surface. Strongest resonance transmission reaching ~7 dB could be identified near the 1556.1 nm wavelength.

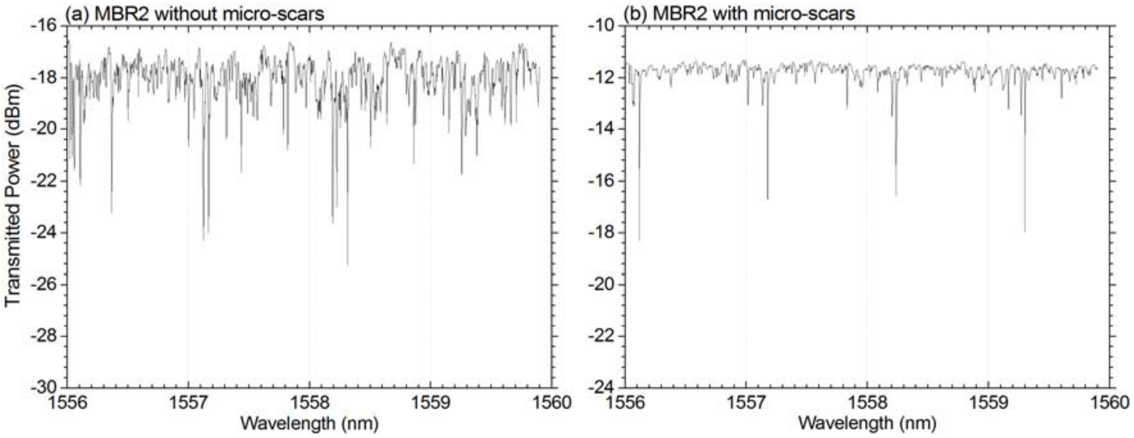

Figure 4.7 WGM spectra of MBR2 excited 127 μm off-centre (a) without and (b) with periodic micro-scars.

The *Q*-factor of MBR2 was not affected much by the inscription of the 21 periodic micro-scars. From Lorentzian fitting of the transmitted spectra, maximum *Q*-factor value in the range of 10^5 were observed in by the MBR after the FIB milling process. Figure 4.8 shows the calculated *Q*-factor of MBR2, indicated by the red line, (a) & (b) without and (c) & (d) with micro-scars inscribed.

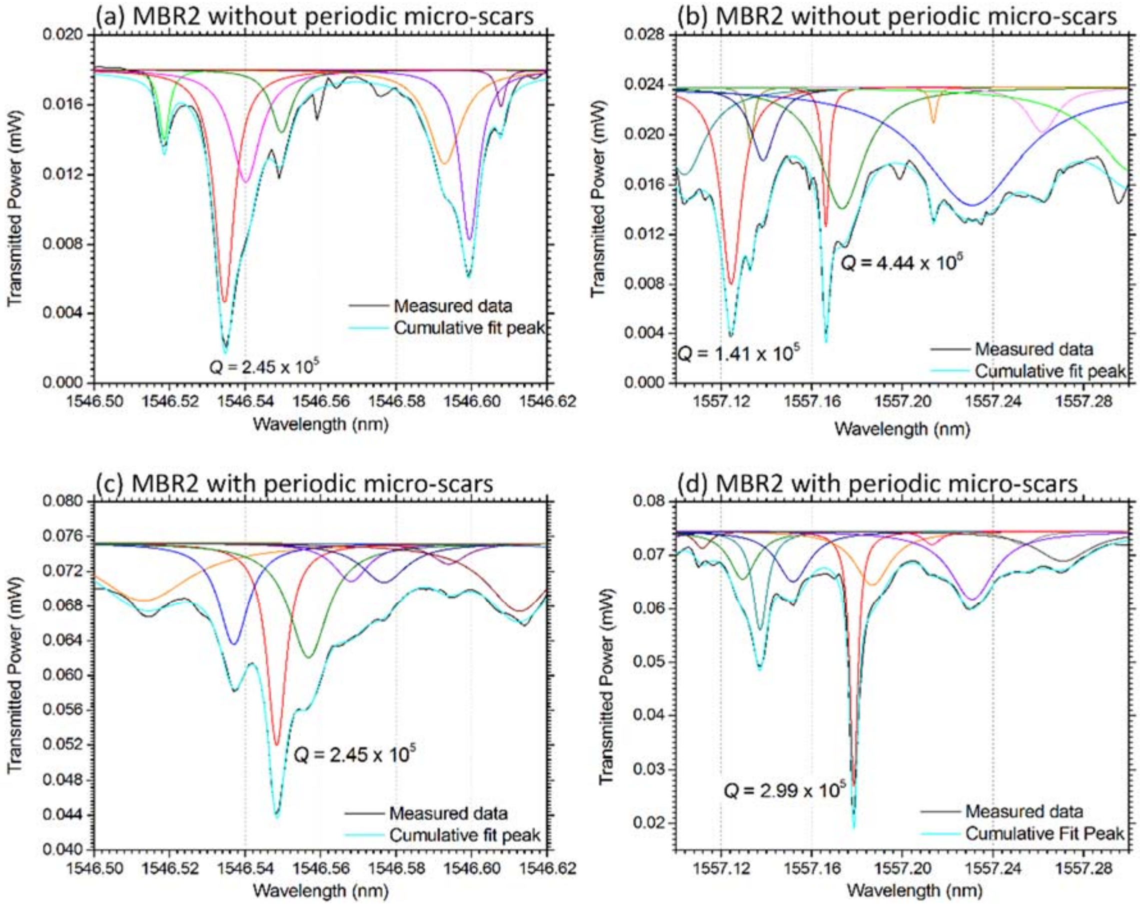

Figure 4.8 Transmitted Lorentzian fitting of MBR2 spectra (a) without and (b) with the inscription of 21 periodic micro-scars.

4.4 Polarization dependent measurement of whispering-gallery microbottle resonators with periodic micro-scars

It is well understood that a specific polarization of light would only excite specific WGMs in an optical resonator. Unless special fibres are utilized [17], it is a real challenge to maintain the polarization of light through the tapered optical fibres which can also provide high coupling efficiency at the same time [18-20]. In contrast to the low coupling-efficiency and complex system proposed in reference [20] and [21], a straightforward method in efficiently discriminating excited-TE and -TM WGMs of any optical microresonator along with high coupling-efficiency using normal tapered fibres is proposed. Figure 4.9 illustrates the schematic of the experimental setup to evanescently couple polarized light into an optical whispering-gallery microresonator.

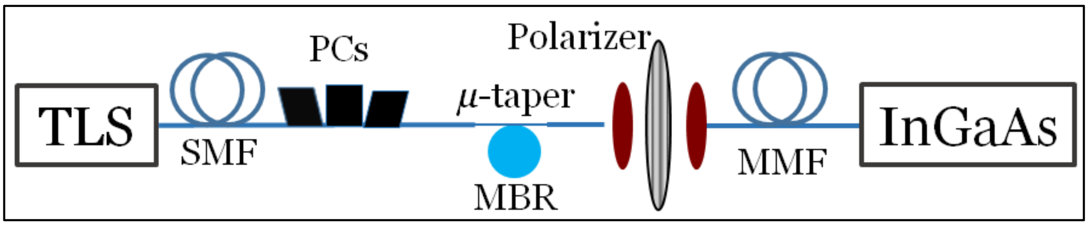

Figure 4.9 Schematic of the optical microresonator polarization-resolved measurement system.

To control the polarization of the tuneable laser source (TLS) light in the optical fibre, a standard SMF linked to a series of polarization controllers (PCs) was set in the system. The SMF was then spliced to an adiabatic tapered fibre of 2 μm waist diameter which had been cleaved at its other full 125 μm diameter end. The tapered fibre was held by rigid a mount and placed on top of an accurate micro-positioning stage. An objective lens with high NA (0.65) was brought close to the tapered fibre cleaved point in order to collimate the output light in free-space. The collimated light was aligned to pass through a highly discriminating polarizer (> 45 dB) which was set to be able to rotated freely to any angle and moved in and out of the system indefinitely. The output light was then focused down using another lens of high NA into a multimode fibre (MMF) for measurement in an InGaAs optical power meter. In order to minimize any birefringence effects that may disrupt the polarization dependent measurement from the point where light was coupled into the cavity of the resonator, the tapered fibre was kept straight after the coupling point of the MBR up to the point where the fibre was cleaved.

Efficiency of the system in discriminating TE- and TM-polarized light was first investigated without coupling the tapered fibre to the MBR. A continuous-wave (cw) laser light at specific wavelength λ_0 was first launched in to the system and monitored through the optical power meter. To couple the laser light to TE-/TM-polarized mode, the polarizer was set to TM/TE orientation and the PCs were tuned until power value at λ_0 reaches a minimum. This would couple the maximum TE-/TM-polarized light into the tapered fibre. Transmission spectra with and without the polarizer placed in the system were then compared to a tuned PCs arrangements and various polarizer rotations. Figure 4.10 shows the performance of the system with the PCs tuned at $\lambda_0 = 1550\ \mathrm{nm}$ for (a) TE and (b) TM polarized light. High polarization-extinction-ratio of > 20 dB could be achieved over a broad wavelength range through the proposed system; comparable to that achieved with a polarization-maintaining optical microfiber in [17]. The minor laser baseline drops after inserting the polarizer is due to the intrinsic loss of the polarizer itself (< 0.8 dB) and the weak Fabry-Pèrot cavity noise originated from the thickness of the polarizer used. The sinusoidal characteristic spectra of the orthogonal-polarized light originated from the birefringence effects caused by the fibre PCs utilized.

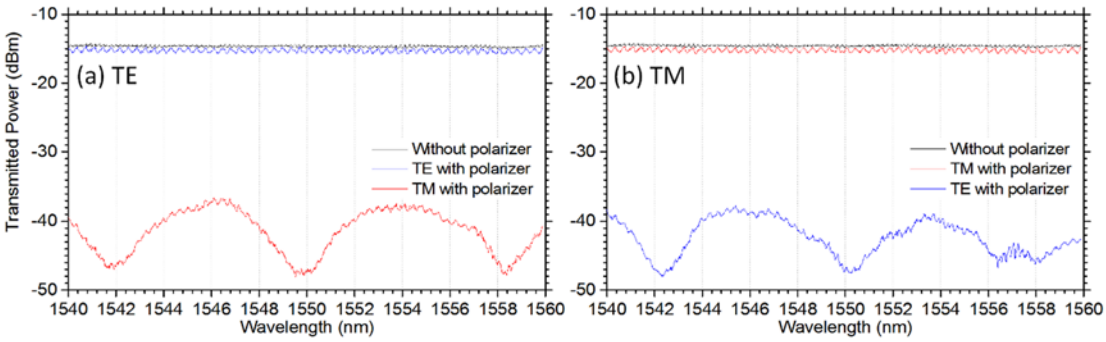

Figure 4.10 Polarization discriminated spectra of the utilized system with (a) TE and (b) TM polarized light.

4.4.1 Polarization dependent measurement of a standard microbottle resonator

For comparison, polarization dependent measurement of a standard MBR was performed. The polarization controller was tuned while the wavelength was fixed at 1550 nm for both TE and TM discrimination alignment processes. Figure 4.11 shows TE and TM WGM spectra of a standard MBR with maximum bottle diameter of 175 μm when excited from the centre position. The wavelength span was set to 20 nm in order to compare it to the measurements performed on MBR1 and MBR2 which yield much simpler spectra (figure 4.13 and 4.17). It could be observed that different modes are indeed being excited with different input of light polarization. However, with such dense and complex spectra of a standard MBR, it is difficult to distinguish one excited whispering gallery family modes from another.

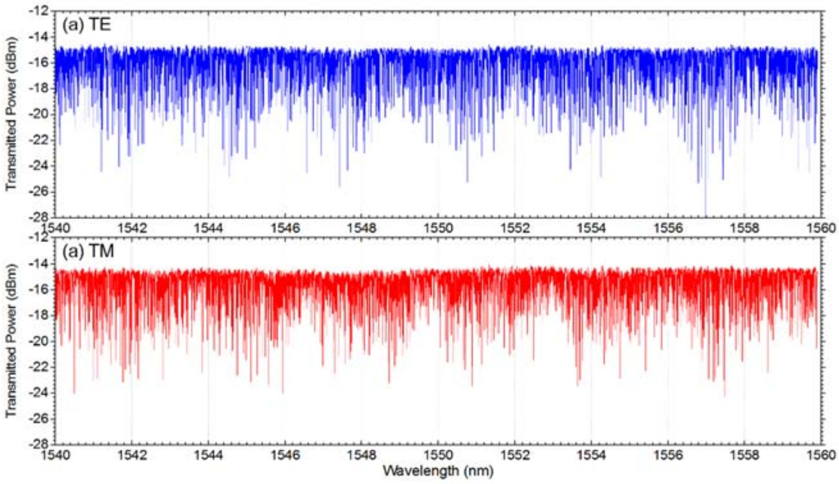

Figure 4.11 Centrally excited WGM spectra of a standard MBR with (a) TE and (b) TM input polarized light.

4.4.2 Polarization dependent measurement of MBR1 with periodic micro-scars

The excitation of the MBRs with periodic micro-scars was performed with optical tapered fibres in direct physical contact with the surface of the resonator. Figure 4.12 (a) shows the excitation arrangement of MBR1 where the tapered fibre was arranged at the centre position of the resonator and within the micro-scars period (red-dashed box). Figure 4.12 (b) shows light scattering at 1550 nm from the MBR.

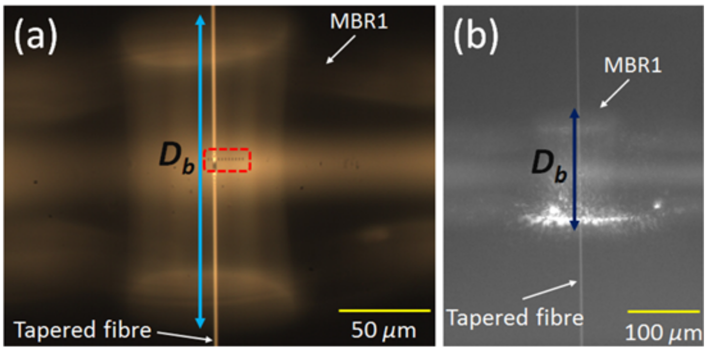

Figure 4.12 MBR1 (a) centre excitation arrangement with (b) its scattered light.

With the tapered fibre in direct physical contact with the surface of the MBR, polarization of the input light was aligned to the TE and the TM modes as measured through the cleaved point of the full 125 μm diameter fibre. The measurements in figure 4.13 were taken with the polarizer removed from the system after the polarization tuning was performed. TE- and TM-excited WGM spectra are clearly distinguishable for MBR1 with the periodic micro-scars as many strongly coupled transmission dips are not observable through the orthogonal spectra. This highly discriminating WGM feature would be near impossible to distinguish through the dense spectra of a standard MBR [11]. High coupling efficiency into the MBR could also be achieved with maximum transmission dip of < 16 dB. Free spectral range (FSR) of the excited MBR modes could also be determined with high precision through the simpler spectra and was between 3.16 – 3.19 nm.

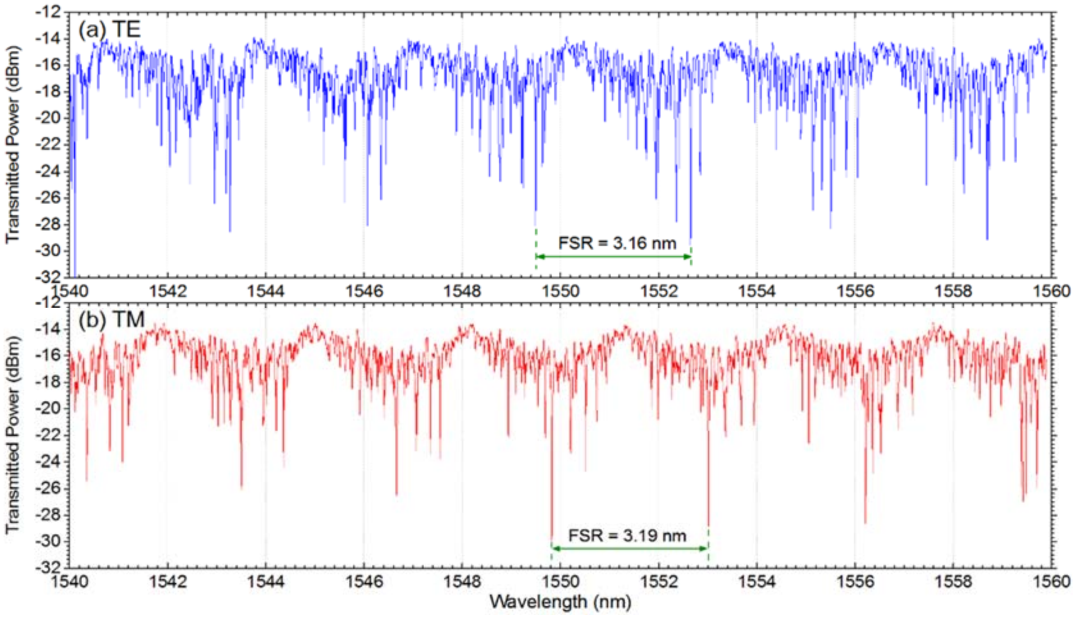

Figure 4.13 MBR1 centrally excited WGM spectra with (a) TE and (b) TM input polarized light.

The polarization of the input light was then tuned to a 45° angle by tuning the polarization controllers to minimize the power of λ_O at -45° (or 315°). Figure 4.14 (a) shows that without placing the polarizer in the system, the MBR1 transmitted spectrum comprises of mixed polarization-excited WGMs with small overall transmission dips. However, as in figure 4.14 (b) and (c), by maintaining the same polarization controller arrangements and placing the polarizer in the system to either TE or TM orientation, transmitted WGM spectra comparable to that of figure 4.13 could be captured (WGM spectra with properly aligned TE/TM input light).

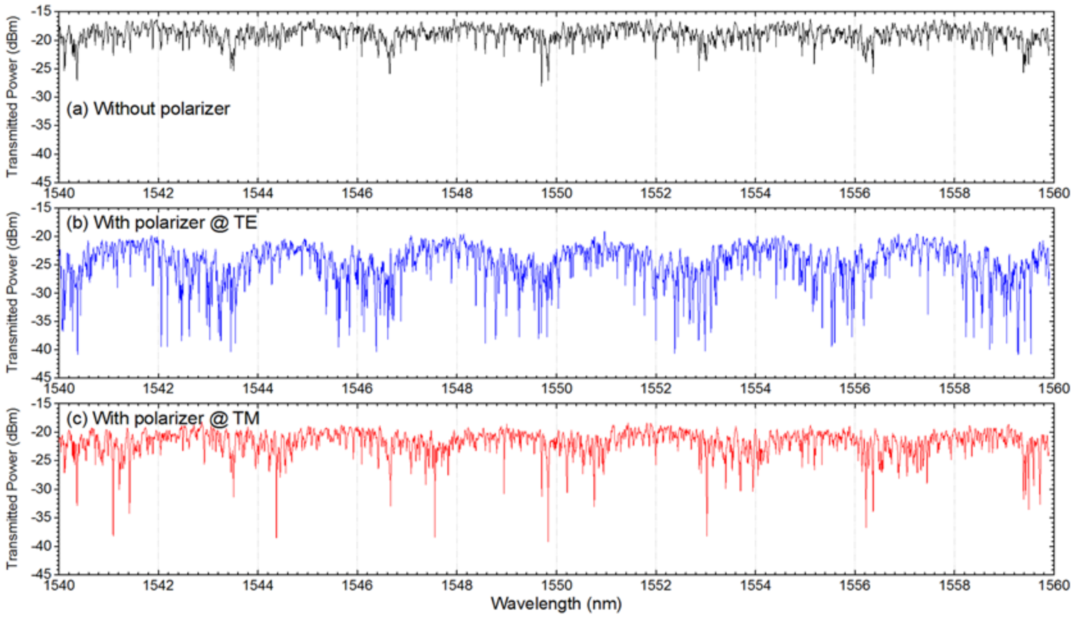

Figure 4.14 MBR1 transmitted spectra for excited WGM with fixed 45° input light polarization and (a) without any polarizer in the system, (b) with polarizer oriented to TE, and (c) with polarizer oriented to TM.

The average baseline of the mixed MBR1 transmission in figure 4.14 (a) is at -17 dBm and it dropped to ~ -20 dBm with the polarizer placed in the system in (b) and (c). This 3 dB drop corresponds to equal filtering of TE- and TM-excited WGMs transmitted power by the polarizer and it indicates that the light coupled into the cavity of MBR1 was in fact mix-polarized at 45° between TE and TM. Maximum transmission dip with the polarizer placed in system as it filters out TE/TM spectra increases from 7 dB without the polarizer to 20 dB with the polarizer.

Excitation arrangement of the tapered fibre was further investigated on carred MBR1 along its axial path with interesting WGM resonant features observed near the micro-bottle necks. Exciting MBR1 140 μm off-centre generates a distinguishable 18 dB transmission dip over a broad spectral wavelength. The sharp resonance dip centred at 1548.96 nm and only occurred with TE-polarized light coupled into the cavity of the resonator. Other modes excited shows transmission dips of less than 10 dB. Figure 4.15 (a) shows the sharp and highly distinguishable TE-WGM resonance dip with its inset showing more detailed measurement at 0.1 pm resolution. The distinguishable feature of this particular resonance mode would be useful should the MBR is utilized in sensing applications where tracing a specific mode is required as it shifts over a broad wavelength range. Explanation towards the cause of this phenomena will be discussed in section 4.5.

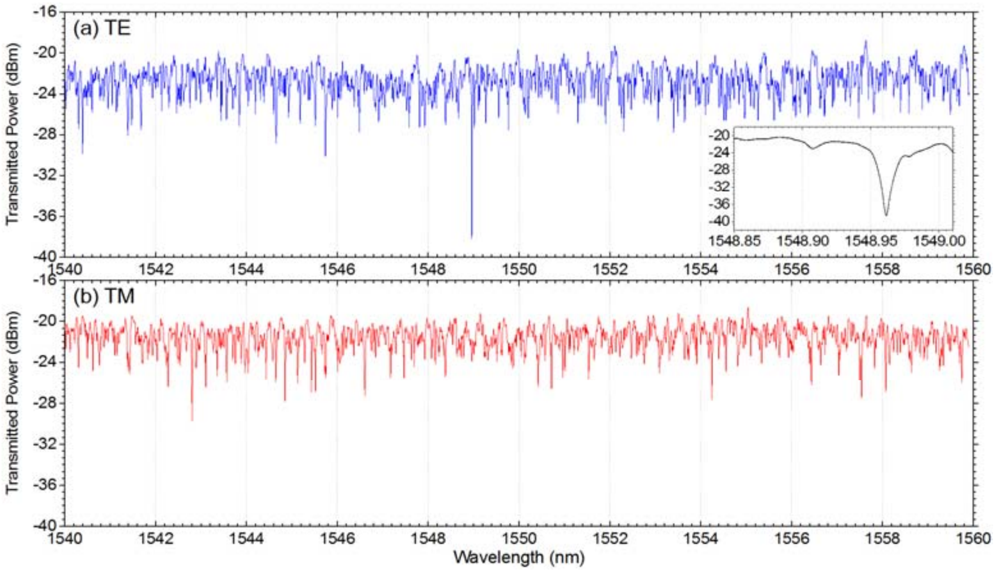

Figure 4.15 MBR1 WGM excited 140 μm off-centre with (a) TE and (b) TM polarization input light.

4.4.3 Polarization dependent measurement of MBR2 with periodic micro-scars

It was observed that by placing the tapered fibre at the centre and on top of MBR2 periodic micro-scars, the transmitted WGM spectra only yields relatively small transmission resonance dips. The presence of the micro-scars attenuates the evanescent light and only allows low coupling efficiency to occur. Figure 4.16 shows (a) TE- and (b) TM-WGM transmission spectra of MBR2 when excited at the centre (with the tapered fibre set on top of the periodic micro-scars). TE-excited WGMs shows maximum transmission dips in the range of ~ 4 dB. TM-excited WGMs shows a much lower coupling efficiency with maximum transmission dips of ~ 2 dB. Nonetheless, comparing to the dense and complex WGM spectra of a standard MBR (figure 4.11), much simpler and sparser centrally excited WGM spectra was generated by MBR2 even with relatively smaller transmission dips.

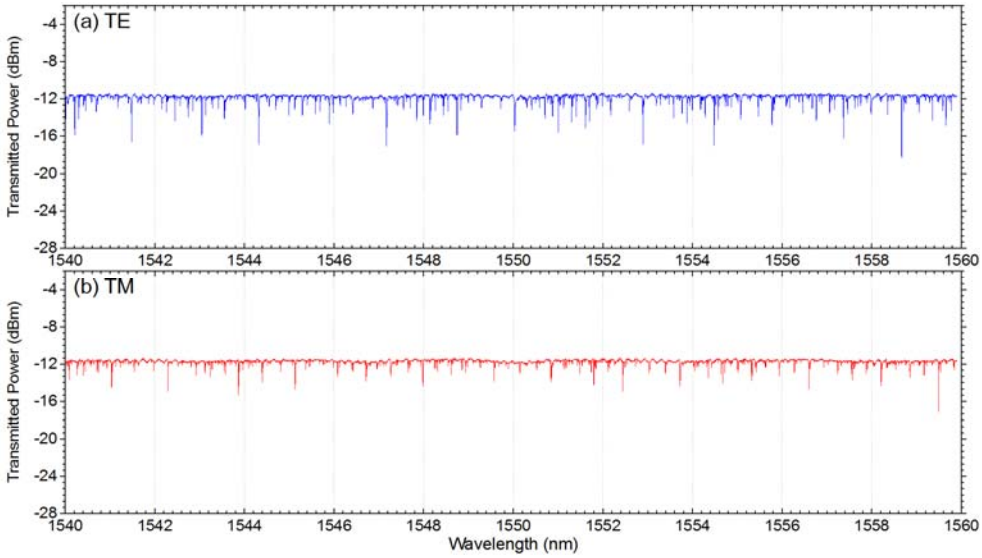

Figure 4.16 Centrally excited WGM spectra of MBR2 (tapered fibre placed on top of the periodic micro-scars) with (a) TE and (b) TM input polarized light.

In order to improve the coupling efficiency, the tapered fibre was then arranged to excite the MBR whispering-gallery modes from the edges of the periodic micro-scars, which is ~ 7 μm away from centre. Figure 4.17 shows (a) the excitation arrangement for MBR2 (with the micro-scars period inside the highlighted red-dashed box) and (b) its light scattering with 1550 nm lasing light.

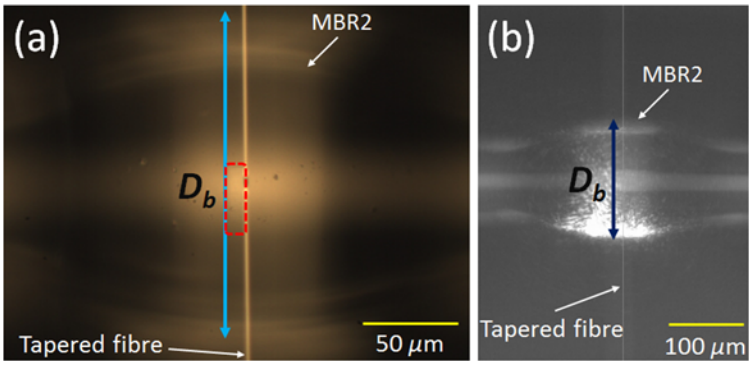

Figure 4.17 MBR2 (a) excitation arrangement with (b) its scattered light.

The polarization of the input light was aligned to excite the TE and the TM modes and MBR2 WGM transmitted spectra were captured through the cleaved tapered fibre point. As with the previous scarred MBR, the transmitted spectra of MBR2 also became much more simplified than that of a standard MBR. FSR of MBR2 could be distinguished through the TE excited resonances with a smaller range compared to MBR1. This is expected since, from equation 2.44, the larger diameter of MBR2 resonator would yield smaller resonating FSRs. Figure 4.18 shows (a) TE- and (b) TM-excited transmitted WGM transmission spectra of MBR2. The maximum transmission dip observed in the spectra reaches up to 18 dB.

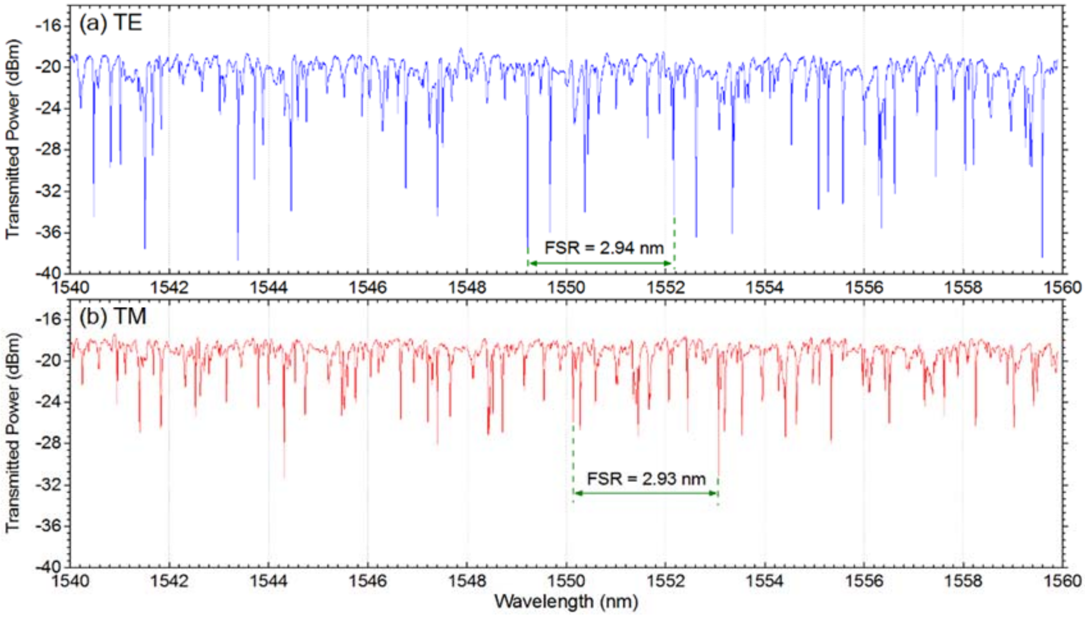

Figure 4.18 MBR2 WGM spectra excited 7 μm off-centre with (a) TE and (b) TM input polarized light.

Tuning the input polarized light to 45° angle also yields MBR2 to generate mixed WGM excited resonance spectra with small overall transmission dips. Filtering off the spectra to either just TE or

TM resonances could be achieved by placing the polarizer in the system. Figure 4.19 shows the captured WGM transmitted spectra of MBR2 excited 7 μm away from the centre with input light aligned at 45° (a) without the polarizer placed in the system, (b) with the polarizer aligned to TE orientation, and (c) with the polarizer aligned to TM orientation.

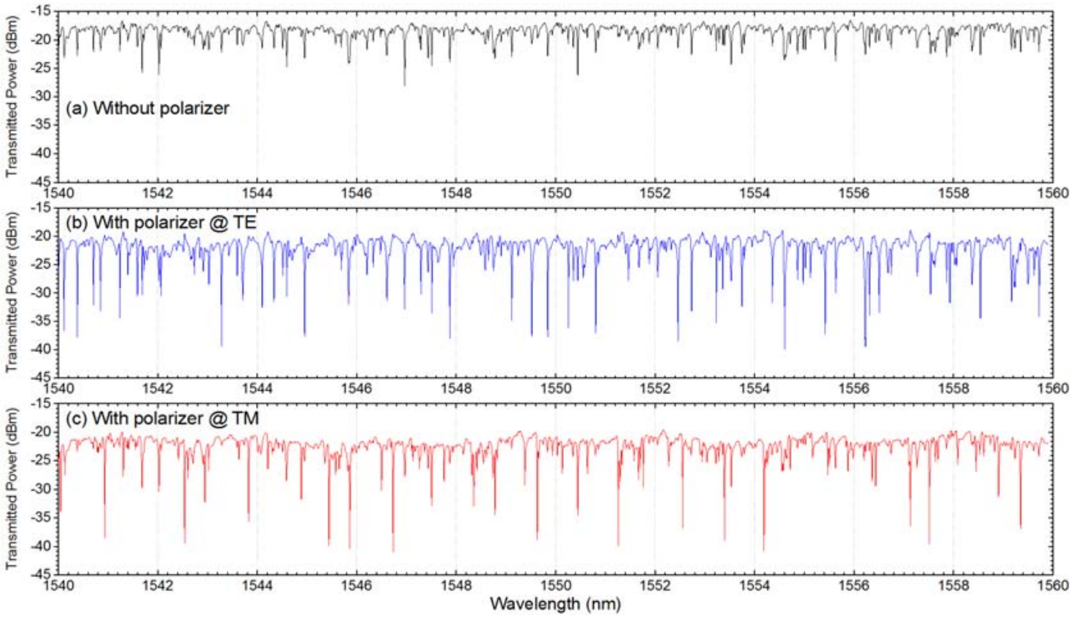

Figure 4.19 MBR2 excited WGM transmitted spectra with fixed 45° input light polarization and (a) without any polarizer in the system, (b) with polarizer oriented to TE, and (c) with polarizer oriented to TM.

The average baseline of the mixed MBR2 transmission spectra in figure 4.19 (a) dropped from -17 dBm to ~ -20 dBm with the polarizer placed in the system in (b) and (c). The 3 dB drop for each transmitted spectra filtering again indicates that the mixed transmitted spectra actually comprise of equal TE and TM excited WGM resonances. The maximum transmission dip with the polarizer placed in system as it filters out TE/TM spectra increases from 7 dB without the polarizer to 20 dB with the polarizer introduced in the system.

The excitation arrangement of the tapered fibre was further investigated on the scarred MBR2 along its axial path. Exciting MBR2 195 μm away from the resonator centre position generates a sharp and distinguishable 8 dB WGM transmission dip over a broad spectral wavelength. The resonance centred at 1549.242 nm and was only generated with TE-polarized input light. Other modes excited shows transmission dips of ~ 3 dB average. Figure 4.20 (a) shows the distinguishable TE-WGM resonance dip with its inset showing a more detailed measurement at 0.1 pm resolution. As could be seen in figure 4.20 (b), no distinguishable WGM spectra were generated with TM-polarized light coupled into the cavity of MBR2. The average transmission dip of the spectra is ~ 3dB. Section 4.5 discusses further the cause of this unique phenomena.

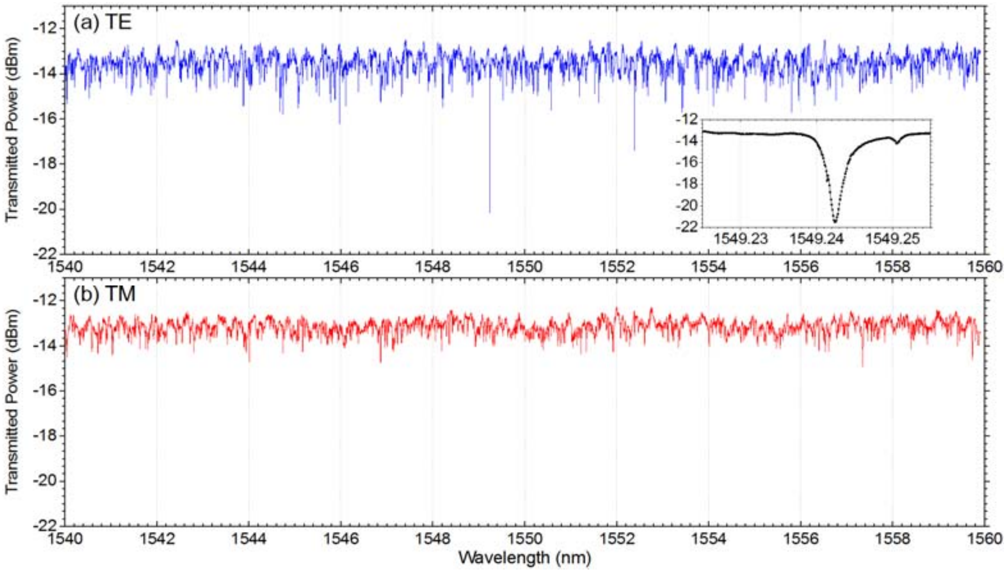

Figure 4.20 MBR2 WGM excited 195 μm off-centre with (a) TE and (b) TM polarized input light.

4.5 FDTD simulation of WGM microdisc resonator with periodic micro-scars

To get additional physical insight into the effects of micro-scars on whispering-gallery microresonators, simulations to a microdisc resonator were performed on a 2D environment using a finite-difference time domain (FDTD) software package [22]. A waveguide with 0.7 μm-wide core and 16 μm length was utilized to couple light evanescently into a whispering-gallery microdisc resonator with 7 μm radius. In order to avoid over-coupling effects, a 0.15 μm gap was set on the coupling point between the waveguide and the microdisc. Five periodic micro-scars were set on top of the microdisc with 1 μm depth and pitch of 0.7 μm. The micro-scars had width of 0.5 μm at the surface of the microdisc and they were set to taper down adiabatically to $^{1}/_{100}$ of its initial width as it tunnels into the resonator in order to mimic the v-shaped scars of the experimental work. The refractive index of the micro-scars and the background was set to 1 (air) and refractive index of the waveguide and the microdisc was set to 1.5 (glass). Perfectly matched layers were set on the boundaries of the computed windows in order to avoid any back-reflections that may affect the simulation. With such microdisc structure and size, coupling light into the microresonator (even without any periodic micro-scars) at 1.55 μm wavelength would radiate most of the energy into the background (air). Coupling light at 1 μm wavelength yields greater whispering-gallery light confinement towards the simulated structure. A TM-fundamental mode pulse of Gaussian-shape and centred at 1 μm wavelength was launched from position $z = -6$ in the waveguide with a power monitor placed at the other end.

Figure 4.21 shows transmitted spectra of the shorter wavelength captured from the output end of the waveguide without and with the introduction of the periodic micro-scars on the microdisc. It was observed that the strong WGM resonances of the resonator were attenuated with the introduction of the periodic micro-scars on this particular wavelength range. Maximum coupling efficiency dropped from 80% to just ~ 30% with the introduction of the micro-scars.

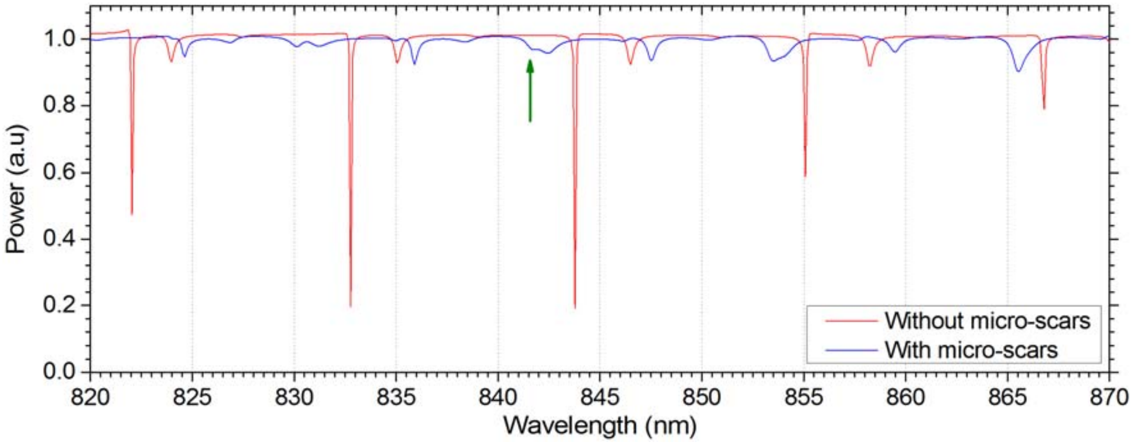

Figure 4.21 Transmitted shorter wavelength range spectra of WGM microdisc resonator without and with periodic micro-scars.

Figure 4.22 shows the magnetic **H**-field steady state distribution of the simulated microdisc resonator with periodic micro-scars at the wavelength of 841.75 nm. The whispering-gallery modes of two-radial mode orders were poorly excited at this specific wavelength. The micro-scars crafted the microdisc as a very lossy structure at such wavelength, hence only warranting low coupling energy transfer to the microdisc with high portion of the energy passing through the waveguide.

It could be seen that the light was scattered out by the micro-scars into the background of the computed window with only a small fraction of the power resonating at the surface of the microdisc. Figure 4.23 shows the zoomed-in image of light scattering by the micro-scars with a higher-contrast colour field distribution. It should then be specified that the small resonance spectral dip at 841.75 nm wavelength must be accounted to the low power resonating modes on the surface of the microdisc and the scattered-out power by the periodic micro-scars.

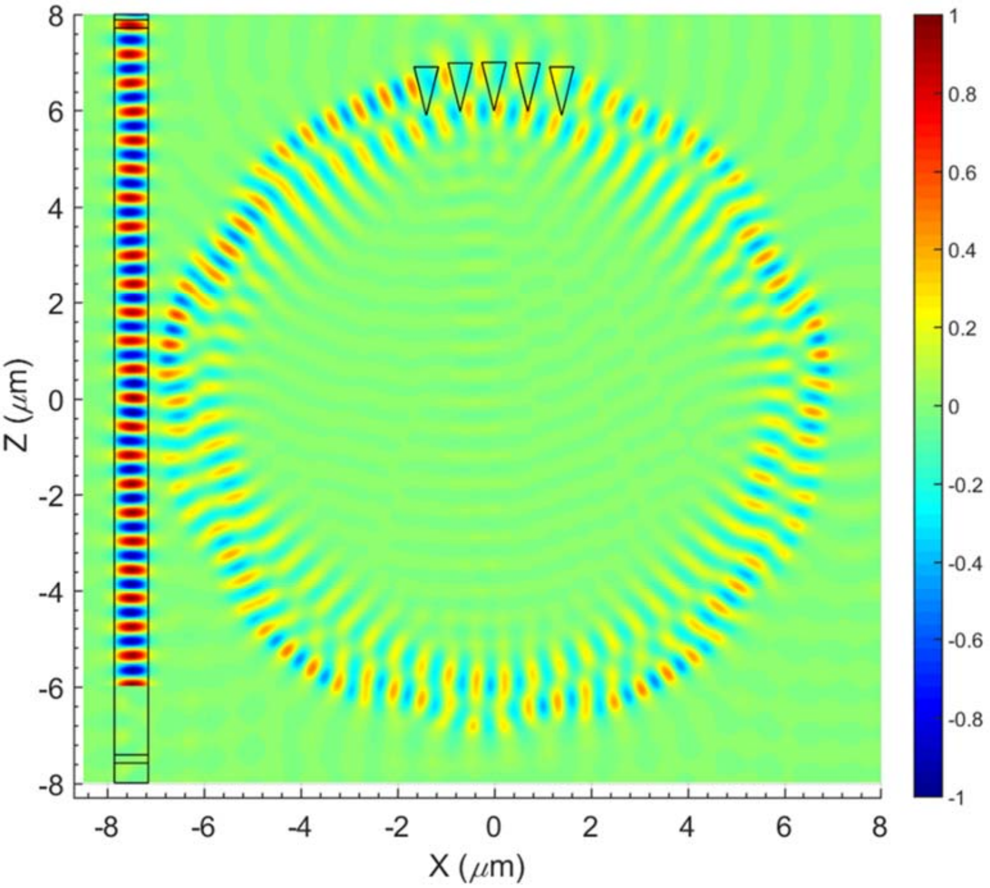

Figure 4.22 **H**-field steady state distribution of WGM microdisc resonator with periodic micro-scars at cw light wavelength of 841.75 nm.

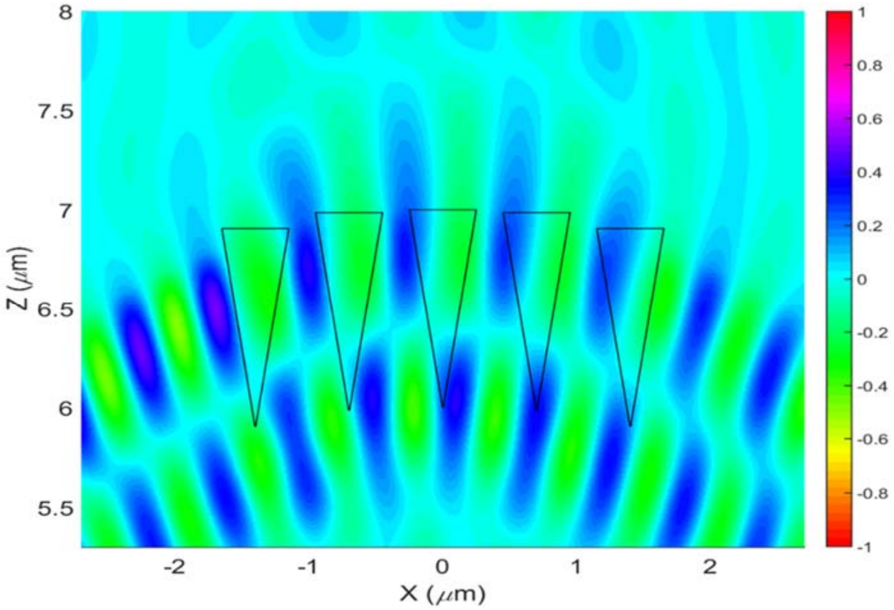

Figure 4.23 Zoomed-in **H**-field steady-state distribution of the micro-scars at cw wavelength of 841.75 nm showing light scattering to the outside medium (air) caused by the scars defects.

Figure 4.24 shows the longer wavelength range of the transmitted spectra through the waveguide output end with and without the presence of the periodic micro-scars on the surface of the resonator. With the micro-scars introduced, some weakly coupled and low-*Q* WGM resonances were generated along with some strongly coupled and high-*Q* ones. Maximum coupling efficiency were observed to improve from 40% to 75% with the introduction of the periodic micro-scars.

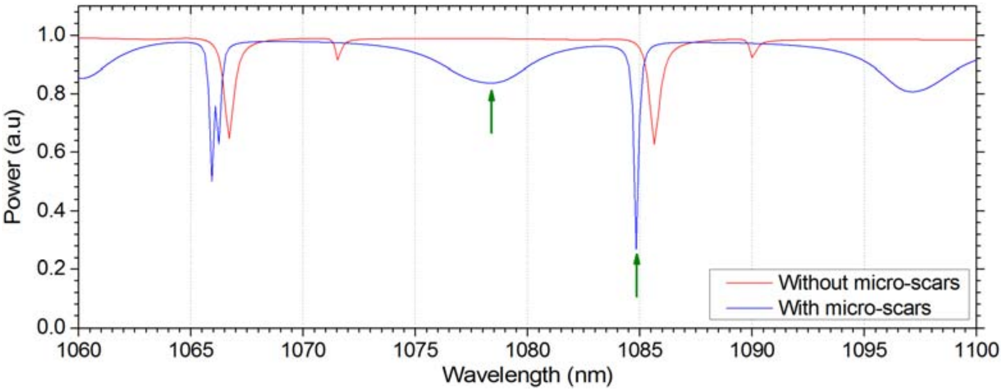

Figure 4.24 Transmitted longer wavelength range spectra of WGM microdisc resonator without and with periodic micro-scars.

Magnetic **H**-field steady-state distribution of the weakly coupling and low *Q*-factor whispering-gallery mode at wavelength 1078.40 nm is shown in figure 4.25. Light which was coupled into the cavity of the resonator was partially scattered out and partially reflected by the micro-scars to an altered path within the resonator, resulting to low light confinement near the surface of the microdisc.

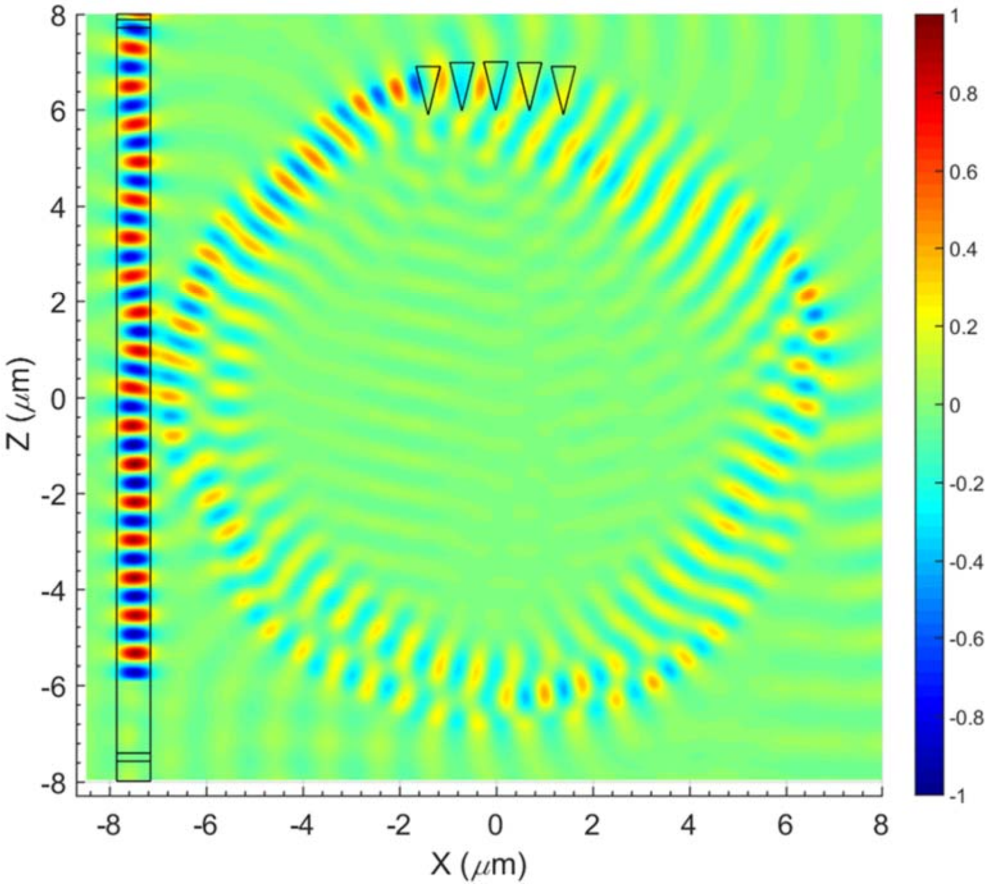

Figure 4.25 **H**-field steady state distribution of WGM mirodisc resonator with periodic micro-scars at cw light wavelength of 1078.40 nm.

Figure 4.26 shows the steady-state magnetic **H**-field distribution of the microdisc along with the periodic micro-scars at the sharp resonance wavelength of 1084.80 nm. Two whispering-gallery radial-order-modes were observed to be excited from near of the resonator coupling point. However, as the modes start to resonate near the micro-scars, they start to beat together and finely positioned themselves in between the scars defects. Passing through the periodic micro-scars, the modes started to show clear transformation back to two whispering-gallery radial-order-modes and continue to circulate the resonator near its surface. Only a small portion of the light energy was scattered out into the background by the micro-scars. The circumvention of the resonating modes from interacting with the periodic micro-scars allows for strong whispering-gallery light confinement near the microdisc surface. This phenomenon would explain the transmitted spectra observed in figure 4.15 (a) and 4.20 (a) of MBR1 and MBR2, respectively, where a single strong and sharp whispering-gallery resonance was generated over a broad wavelength range.

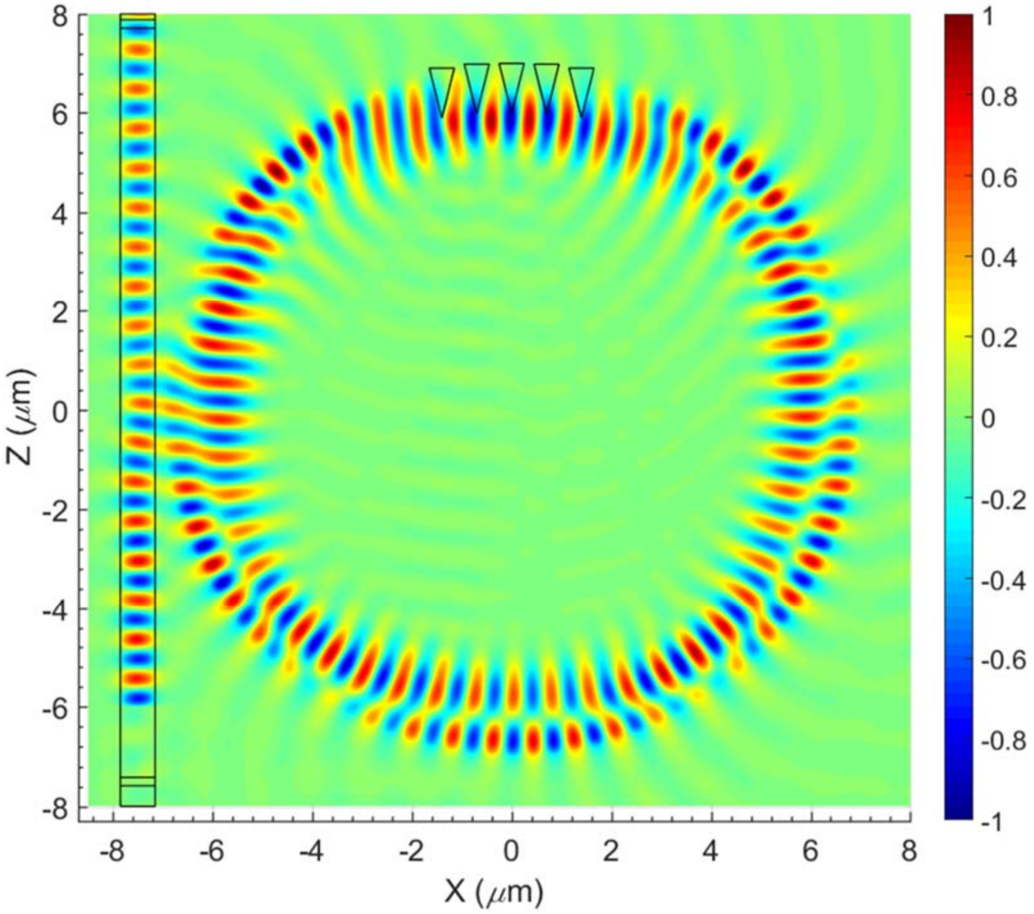

Figure 4.26 **H**-field steady state distribution of WGM microdisc resonator with periodic micro-scars at cw light wavelength of 1084.80 nm showing two modes beating together and positioning themselves between the scars defects.

4.6 Summary

A precise controllable method to simplify the transmitted WGM resonances of MBRs through the inscription of periodic micro-scars on the surface of the resonator has been successfully demonstrated. High *Q*-factors in excess of 10^5 were preserved by the MBRs even after the milling process. Highly discriminating polarization resolved measurements on the scarred MBRs also distinguished clearly the TE- and TM-excited WGMs with just the utilization of normal optical tapered fibres. Excitation arrangement near the MBR necks yielded a strong distinguishable resonance spectra dip over a broad spectral wavelength specifically with TE polarized input light. FDTD simulation performed on a WG microdisc shows that the micro-scars would scatter light out of the resonator at certain wavelengths. The resonating modes are also capable to beat together at longer wavelengths in order to circumvent the defect introduced by the micro-scars, generating a high-*Q* WGM resonance. This unique feature of scarred MBRs are highly advantageous to be utilized as markers in sensing applications where monitoring specific excited WGMs through a broad spectral wavelength range is required. The experimental demonstration using the simplified polarization-resolved setup presented in this chapter is an important reference for future optical microresonator work, especially those involving a highly-discriminative polarization measurement.

4.7 References

[1] K. J. Vahala, "Optical microcavities," *Nature* **424**, 839 (2003).

[2] V. Lefevre-Seguin and S. Haroche, "Towards cavity-QED experiments with silica microspheres," *Materials Science and Engineering: B* **48**, 53 (1997).

[3] J. –B. Jager, V. Calvo, E. Delamadeleine, E. Hadji, P. Noé, T. Ricart, D. Bucci, and A. Morand, "High-Q silica microcavities on a chip: From microtoroid to microsphere," *Applied Physics Letters* **99**, 181123 (2011).

[4] D. K. Armani, T. J. Kippenberg, S. M. Spillane, and K. J. Vahala, "Ultra-high-Q toroid microcavity on a chip," *Nature* **421**, 925 (2003).

[5] T. Baba, M. Fujita, A. Sakai, M. Kihara, and R. Watanabe "Lasing characteristics of GaInAsP-InP strained quantum-well microdisk injection lasers with diameter of 2-10 μm," *IEEE Photonics Technology Letters* **9**, 878 (1997).

[6] V. Zamora, A. Díez, M. V. Andrés, and B. Gimeno, "Interrogation of whispering-gallery modes resonances in cylindrical microcavities by backreflection detection," *Optics Letters* **34**, 1039 (2009).

[7] V. S. Ilchenko, M. L. Gorodetsky, X. S. Yao, and L. Maleki, "Microtorus: a high-finesse microcavity with whispering-gallery modes," *Optics Letters* **26**, 256 (2001).

[8] M. Sumetsky, Y. Dulashko, and R. S. Windeler, "Optical microbubble resonator," *Optics Letters* **35**, 898 (2010).

[9] M. Sumetsky, "Whispering-gallery-bottle-microcavities: the three dimensional etalon," *Optics Letters* **29**, 8 (2004).

[10] M. Pöllinger, D. O'Shea, F. Warken, and A. Rauschenbeutel, "Ultrahigh-*Q* Tunable Whispering-Gallery-Mode Microresonator," Physical Review Letters **103**, 053901 (2009).

[11] G. S. Murugan, J. S. Wilkinson, and M. N. Zervas, "Selective excitation of whispering gallery modes in a novel bottle microresonator," *Optics Express* **17**, 11916 (2009).

[12] M. Sumetsky and J. M. Fini, "Surface nanoscale axial photonics," *Optics Express* **19**, 26470 (2011).

[13] G. S. Murugan, M. N. Petrovich, Y. Jung, J. S. Wilkinson, and M. N. Zervas, "Hollow-bottle optical microresonators," *Optics Express* **19**, 20773 (2011).

[14] M. Ding, G. S. Murugan, G. Brambilla, and M. N. Zervas, "Whispering gallery mode selection in optical bottle microresonators," *Applied Physics Letters* **100**, 081108 (2012).

[15] M. N. Mohd Nasir, M. Ding, G. S. Murugan, and M. N. Zervas, "Microtaper fiber excitation effects in bottle microresonators," *Proc. SPIE* **8600**, Laser Resonators, Microresonators, and Beam Control XV, 860020 (2013).

[16] J. C. Knight, G. Cheung, F. Jacques, and T. A. Birks, "Phase-matched excitation of whispering-gallery-mode resonances by a fiber taper," *Optics Letters* **22**, 1129 (1997).

[17] Y. Jung, G. Brambilla, and D. J. Richardson, "Polarization-maintaining optical microfiber," Optics Letters **35**, 2034 (2010).

[18] G. Guan and F. Vollmer, "Polarized transmission spectra of the fiber-microsphere system," *Applied Physics Letters* **86**, 121115 (2005).

[19] G. Adamovsky and S. Wrbanek, "Coupling of low-order LP modes propagating in cylindrical waveguides into whispering gallery modes in microspheres," Optics Express **21**, 2279 (2013).

[20] P. Bianucci, C. R. Fietz, J. W. Robertson, G. Shvets, and C.-K. Shih, "Polarization conversion in a silica microsphere," Optics Express **15**, 7000 (2007).

[21] H. Konishi, H. Fujiwara, S. Takeuchi, and K. Sasaki, "Polarization-discriminated spectra of a fiber-microsphere system," *Applied Physics Letters* **89**, 121107 (2006).

[22] RSoft Design Group, Rsoft Inc., FullWAVE 6.0 (2008).

Chapter 5: Polarization effects in optical microresonators

5.1 Introduction

Over the years a number of advanced high-Q optical whispering gallery mode (WGM) microresonator-based devices have been proposed and successfully demonstrated [1]. Among the well-established WGM microresonators are the microspheres [2], microtoroids [3] and microdisc [4]. Recently, microbottle resonators [5] and bubble microresonators [6] have also been demonstrated to attain complex and dense whispering-gallery mode (WGM) spectra. Since excitation of WGMs in any microresonator is polarization sensitive, it is important to understand their performance under TE/TM launching conditions and their polarization cross-coupling. It has been reported that light can change its state of polarization when it is coupled into and out of a microcavity [7]. Polarization cross-coupling at the output of a resonator can take place either through coupling into an "intermediate" resonant state (i.e. WGM) with composite polarization [8], or polarization rotation due to resonant polarization-dependent transmission and associated phase shift [9]. The former was investigated in ring resonators and the cross-polarization was found to increase with non-vertical ring walls. In the latter, a polarimetric setup was used in order to control the polarization and characterize the polarization cross-coupling in microspheres [10].

In this chapter, we investigate the polarization cross-coupling behaviour in a number of different optical whispering-gallery microresonators. Section 5.2 describes the utilized microresonators for the polarization experimental study. Polarization alignment and cross-coupling characterization set-up for the optical microresonators under study are described in section 5.3. Experimental cross-polarization results with respect to the input light polarization of the microresonators are presented in section 5.4. The experimental results are also compared to a theoretical model developed based on Jones matrix calculus in section 5.5.

5.2 Optical whispering-gallery microresonators utilized for polarization measurement

Polarization cross-coupling (PXC) behaviour on whispering-gallery resonators was investigated on a number of different microresonators. Figure 5.1 shows the four optical microresonators under test, (a) a microsphere, (b) a microcylinder, (c) a milled micro-rod resonator, and (d) a microbottle resonator (MBR) with micro-scars. The microsphere utilized was a commercial silica resonator (Duke Scientific 9060) with diameter of 60 μm, while the cylindrical resonator was a standard silica fibre with outer diameter of 125 μm. The micro-rod resonator was fabricated by milling two sections of a conventional single-mode fibre (SMF) with a pulsed CO_2 laser. The MBR under test has maximum diameter of 170 μm with two micro-scars milled close to its centre so that most of its axial WGMs would not be excited yielding a simplified transmission resonance spectrum.

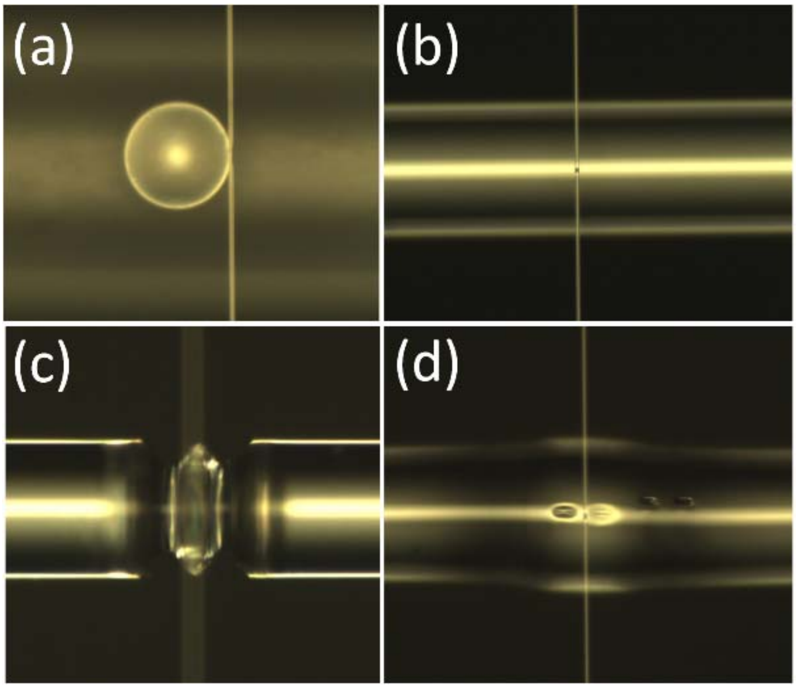

Figure 5.1 Optical WGM resonators under test: (a) microsphere, (b) microcylinder, (c) milled micro-rod resonator, and (d) scarred MBR.

5.3 Polarization alignment and cross-coupling characterization set-up

The experiment set-up used for the characterization of the polarization alignment and cross-coupling is shown schematically in figure 5.2 (a). A plane polarized light from a tuneable laser source (TLS) was launched through a standard fibre into a tapered fibre with 2 μm diameter waist, brought into direct contact with the microresonator under test. Fibre polarization controllers were utilized to control the plane of polarization of the lasing light coupled into the microresonators. The output end of the tapered fibre was cleaved after its full transition back to full 125 μm diameter as close to its waist and was kept straight in order to minimize any additional bending- and/or stress-induced birefringence. The light from the end of the fibre was collimated using a lens and again focused using another lens into a MMF to be measured by a fibre compatible InGaAs detector.

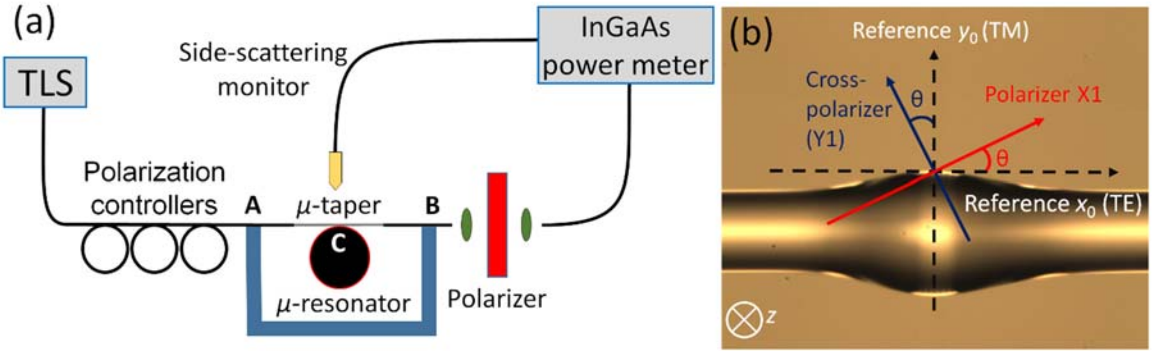

Figure 5.2 (a) Polarization-resolved measurement set-up, and (b) schematic of reference axes and polarizer/ cross polarizer orientations.

A polarizer was between the lenses in order to facilitate polarization alignment and measure the induced polarization cross coupling (cross-polarizer). In addition, the scattered light from the microresonator collected using a microscope objective was measured with the help of a free-space optical power detector to identify WGM resonances. Figure 5.2 (b) shows a schematic of the reference axes (x_0, y_0) with respect to the microresonator surface at the point of the launching tapered fibre contact and the relative orientations of the polarizer (X1) and cross-polarizer (Y1). In the case of optical MBR, the tapered optical fibre was placed on top of the resonator in the *z*-axis direction.

5.3.1 Off-resonance polarization alignment

After having scanned the wavelength and measured the transmission spectrum without the presence of a polarizer, the wavelength from the TLS was fixed at a point of maximum transmission. This is to ensure that the launched wavelength is away from both of the microresonator TE and TM WGM resonances. The polarizer (with polarization extinction ratio > 45 dB) is then inserted with its transmission axis then set at a certain angle θ with respect to reference axis x_0, and the polarization controller is used to maximize the throughput power. Because the segment CB of the microtapered fibre is small (~ 3 cm) and kept straight, the polarization at the microresonator launching point is assumed to be to a large extent the same with the output polarization. However, the validity of this assumption will be explored and tested in the following sections.

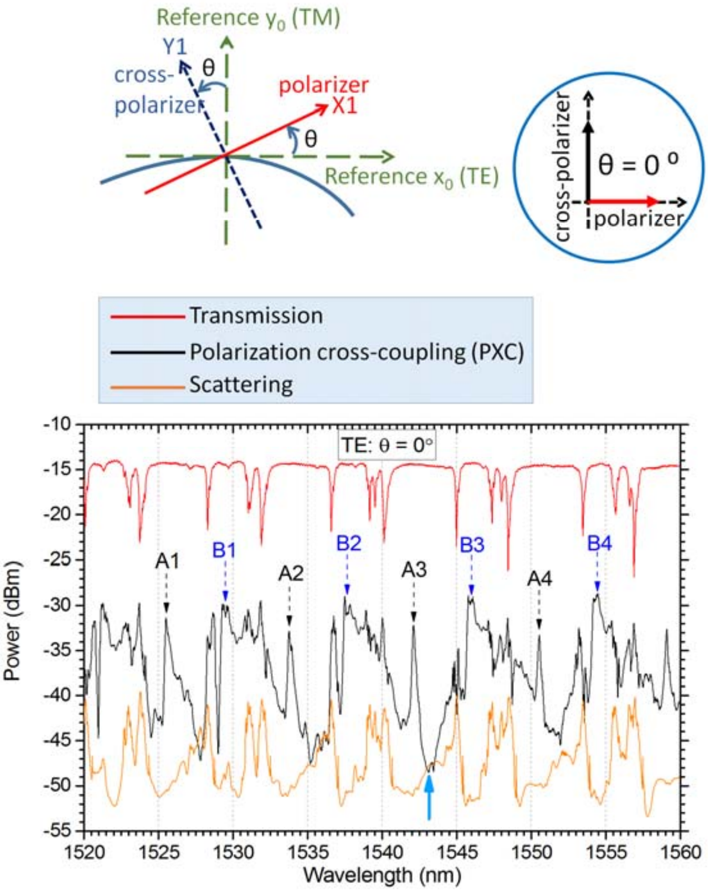

Figure 5.3 Transmission (red line), polarization cross-coupling (black line), and scattering (orange line) spectra for a microsphere. Polarization alignment @ 1543.5nm (thick blue arrow) with the polarizer set at θ=0° (TE polarization).

Figure 5.3 shows the transmission (top red line), polarization cross-coupling (PXC) (middle black line), and scattering (bottom orange line) spectra for a microsphere. The polarization was initially aligned at the off-resonance wavelength of 1543.5nm (thick blue arrow) with the polarizer set at $\theta = 0°$ (TE polarization). It is shown that the scattering and transmission spectra show a clear correlation, with the scattering peaks well aligned with the transmission dips. This is expected since at the transmission dips the launched power is strongly coupled and stored inside the microresonator, which results in increased internal power and therefore scattering (due to surface roughness). The PXC spectrum, on the other hand, shows a much more complex behaviour with no clear correlation with the transmission spectrum. Attention is drawn to two strong and sharp PXC peak families (denoted A1-A4 & B1-B4), which have no obvious corresponding feature in the transmission or scattering spectrum. This implies that the unaccounted A1-A4 & B1-B4 PXC peaks are not associated with TE polarized WGM resonances and owe their origin to different effect. In the next section, the evolution of the transmission, PXC and scattering spectra with launching polarization will be presented.

5.4 Experimental results

Transmission WGM spectra at various polarization angles were recorded along with their respective transmitted cross-polarization and scattered spectra. Figure 5.4 shows the transmission, PXC, and scattering spectra for a microsphere. The polarization was aligned at the off-resonance wavelength of 1543.5nm (thick blue arrow) with the polarizer set at (a) θ=0° (TE polarization), (b) θ=+8°, (c) θ=-8° and (d) θ=90° (TM polarization). The insets show schematically the polariser (P – red arrow) and cross-polariser (XP – black arrow) orientations. Clear whispering-gallery family group-mode of the microsphere could be distinguished by the transmitted spectra with FSR of 8.15 nm.

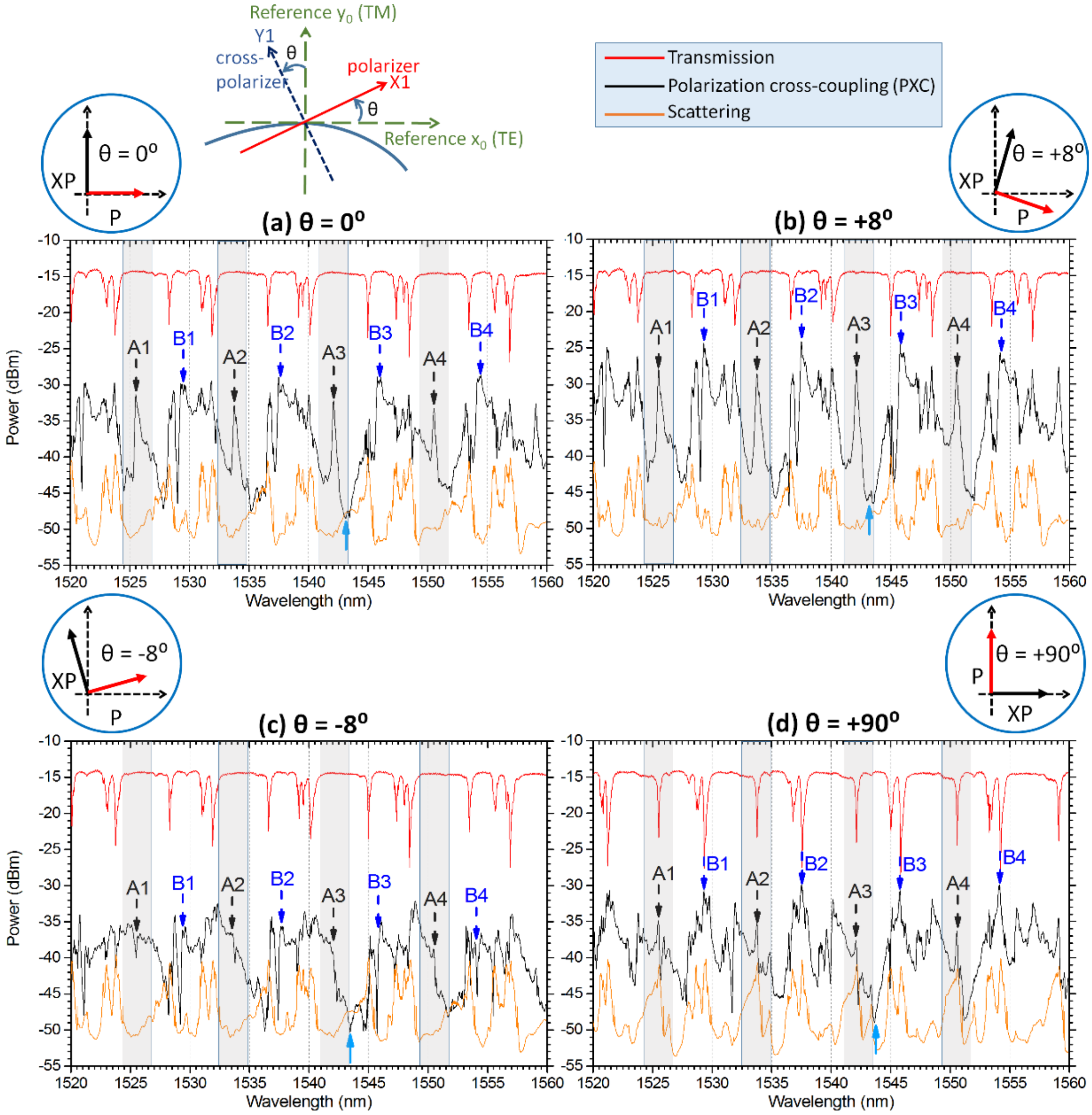

Figure 5.4 Transmission (red line), PXC (black line), and scattering (orange line) spectra for a microsphere. The polarization was aligned at the off-resonance wavelength of 1543.5nm (thick blue arrow) with the polarizer set at (a) θ=0° (TE polarization), (b) θ=+8°, (c) θ=-8° and (d) θ=90° (TM polarization).

It is shown that as the polarizer is rotated to θ=+8° (figure 5.4 b), the transmission dips and scattering peaks reduce slightly, while all the PXC peaks and their average level increase. When the polarizer is rotated in the opposite direction to θ=-8° (figure 5.4 c), however, the transmission dips and scattering peaks increase slightly, while all the PXC peaks and average level decrease. In this case, the initially unaccounted A1-A4 & B1-B4 PXC peaks disappear. Finally, when the polarizer is set at θ=+90°, which corresponds to TM polarization (figure 5.4 d), it is shown that the initially unaccounted A1-A4 & B1-B4 PXC peaks under TE polarization excitation actually correspond to TM-polarized WGM resonances.

These results clearly indicate that the complex PXC spectra, and in particular the initially uncorrelated A1-A4 & B1-B4 peaks under TE polarization excitation, are due to more involved polarization beating/evolution effects. They also indicate that, under the current experimental conditions, negligible PXC at the TM resonances occurs for a polarizer initial orientation θ=-8°. This implies that PXC spectra are better indicators for accurate polarization alignment and WGM excitation in optical microresonators.

For the rest of this chapter (and unless otherwise stated), the polarization orientation of the launched light was carried out at a wavelength away from WGM resonances by maximizing the power through the output polarizer. Figure 5.5 shows the variation of the transmission dips (a & d), scattering peaks ((b) & (e)), and PXC peaks ((c) & (f)) with the polarizer orientation angle θ, for different microsphere WGM TE ((a), (b), (c)) and TM ((d), (e), (f)) resonance wavelengths. The consecutive TE and TM resonance wavelengths are chosen to be one FSR apart and, therefore, belong to the same WGM family. It should be stressed that the polarizer orientation angle θ, during the polarization alignment process, is assumed to define to large extend the state of polarization of the light launched into the microresonator.

It was observed that for both the TE and TM WGM resonances, the transmission dips ((a) & (d)) and scattering peaks ((b) & (e)) follow the expected trends with the polarizer orientation angle θ. As the polarizer orientation angle θ increases towards +90° (or -90°) the TE polarization transmission dips decrease. At the same time, the corresponding scattering peaks also decrease as the excitation of TE WGM resonances becomes progressively smaller. The opposite trend is followed by the TM resonances. It should be stressed, however, that the transmission dip maximum for all the TE resonances (and transmission dip minimum for all the TM resonances) occurs for a polarizer orientation angle θ in the region of -5° to -12°.

The PXC peaks ((c) & (f)) follow a markedly different behaviour. In contrast with transmission dips and scattering peaks, both TE and TM resonances show the same dependence on the polarizer orientation angle θ. It is observed that the PXC peaks show minimum values for a polarizer orientation angle θ≈-10° (note that in a n ideal case these minima were expected to occur at θ≈0°).

In all cases, the PXC peaks show maximum values for a polarizer orientation angle θ≈-55° and θ≈+35° (shifted again by ≈-10° from their ideal values).

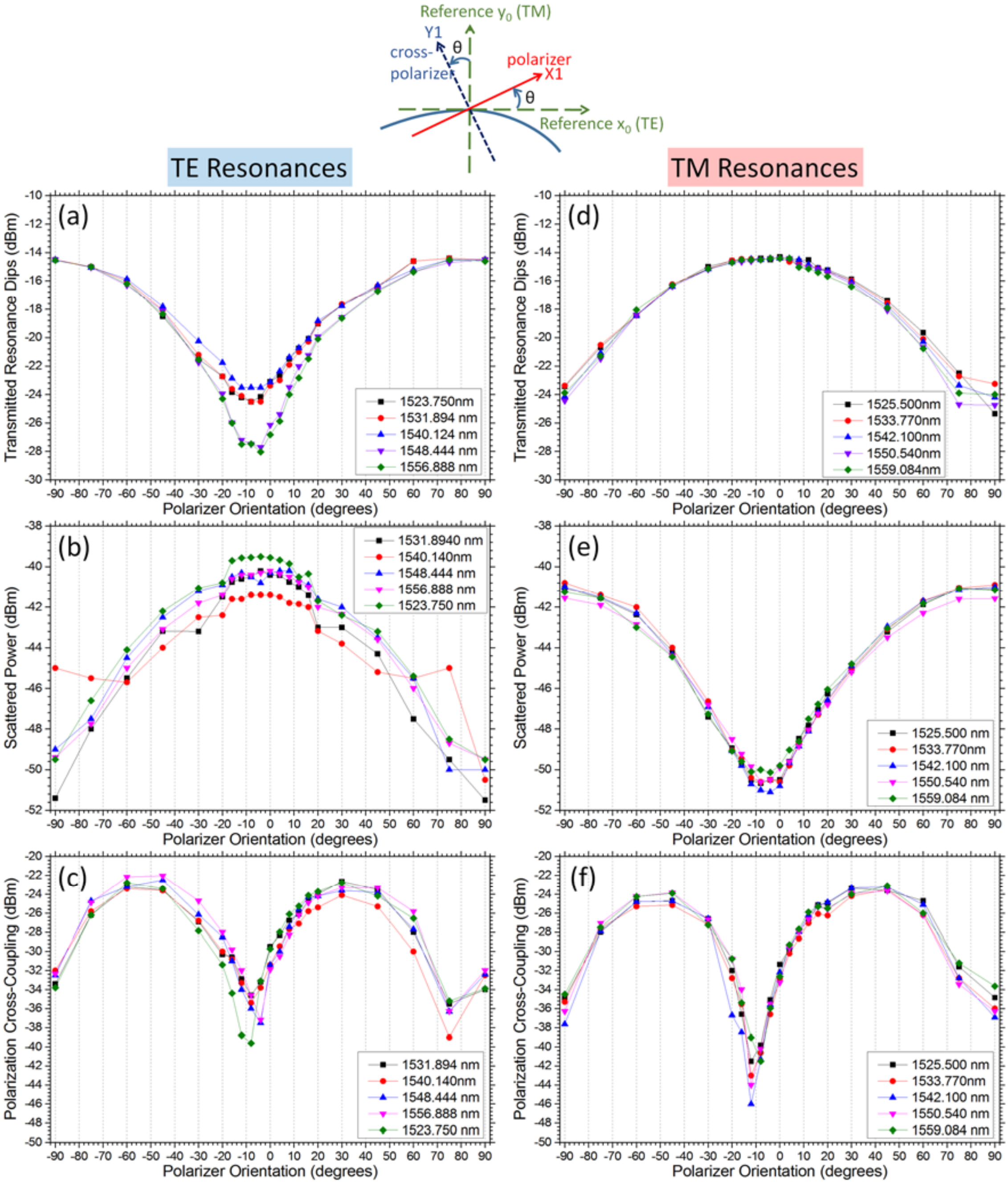

Figure 5.5 Transmission dips ((a) & (d)), scattering peaks ((b) & (e)), and PXC peaks ((c) & (f)) with the polarizer orientation angle θ, for different microsphere WGM TE ((a), (b), (c)) and TM ((d), (e), (f)) resonance wavelengths.

As mentioned in the introduction, PXC can occur either through an “intermediate” WGM resonance with composite polarization [8], or polarization rotation due to transmission-dependent amplitude change and phase shift [9]. However, examining closely and comparing the variation of the scattering peaks (figure 5.5 (b) & (e)), and PXC peaks (figure 5.5 (c) & (f)), with the polarizer orientation angle θ, we can easily deduce that the observed PXC in microspheres *cannot* depend appreciably on the excitation of “intermediate” WGM resonances [8]. This is because in that case, the PXC peaks and scattering peaks at the TE and TM resonances would have followed the same functional dependence on θ, as they both would have been driven by the internally stored WGMs power. This then leaves polarization rotation due to transmission-dependent amplitude change and phase shift [9] as the main contribution to the observed PXC effects. This effect will be explored theoretically in section 5.5.

Figure 5.6 and 5.7 summarize the PXC variation with polarizer orientation angle θ for all tested microresonators, in the case of TE-polarized and TM-polarized WGM resonances, respectively. It was observed that all whispering-gallery microresonators follow similar PXC evolution with the polarizer orientation angle θ. It is shown that the minimum PXC levels do not occur at θ=0°, as would be expected under ideal experimental conditions. In all cases, a polarizer orientation angle θ offset of about ∓10° is measured. The maximum PXC levels, on the other hand, occur for input polarizations around ∓45°.

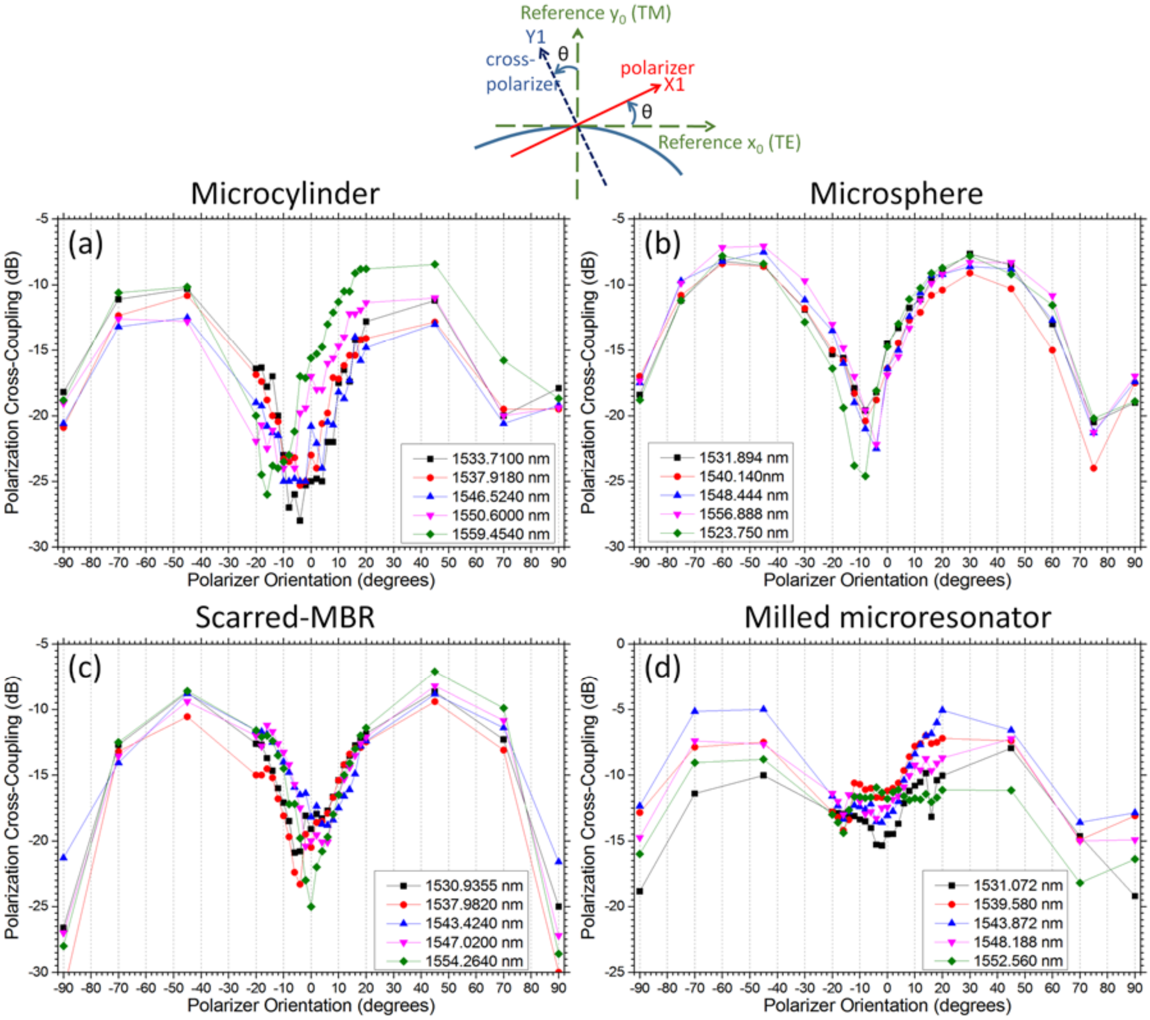

Figure 5.6 PXC variation with polarizer orientation angle θ for (a) microcylinder, (b) microsphere, (c) scarred-MBR, and (d) milled microresonator and TE polarization WGM resonances.

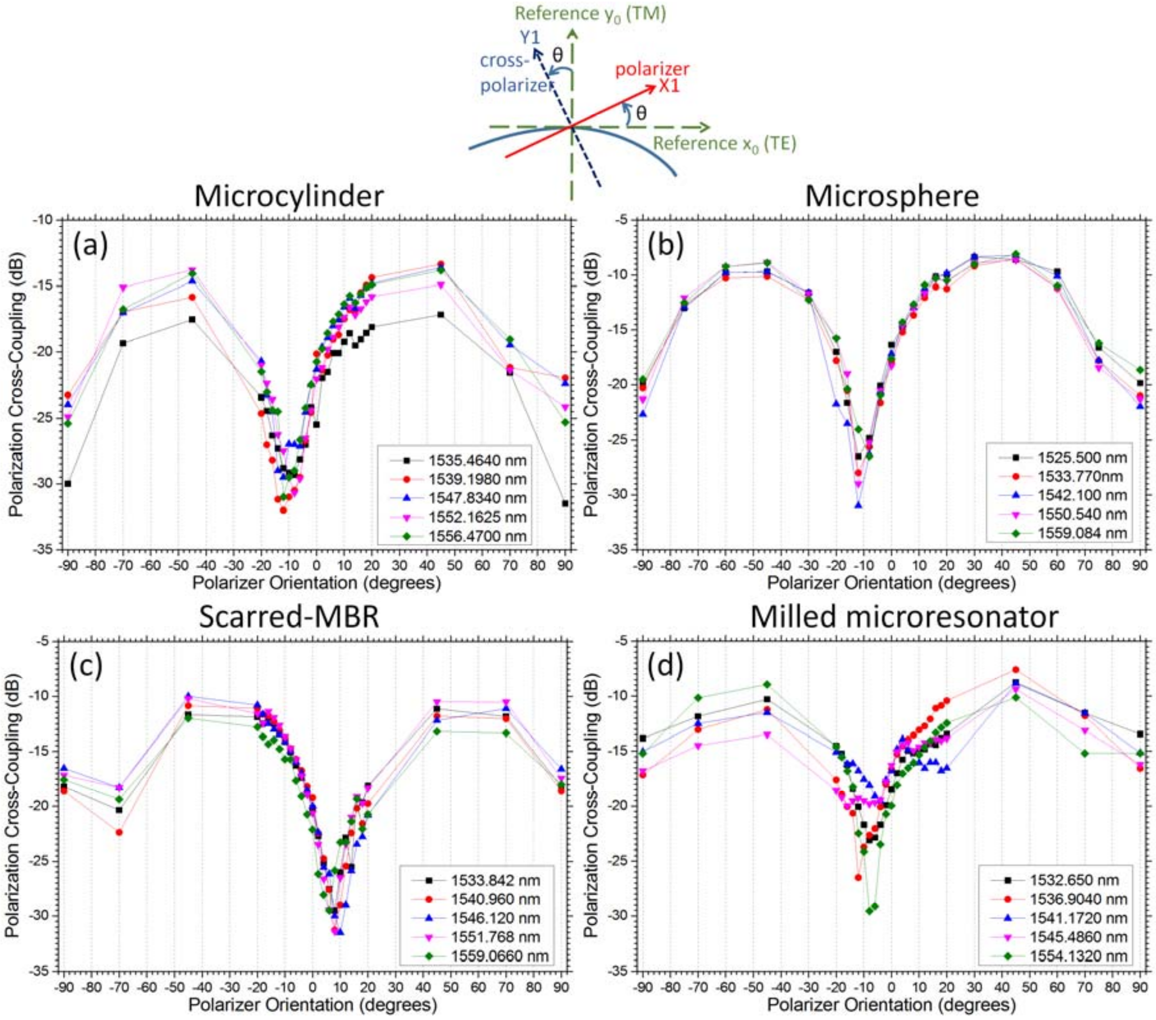

Figure 5.7 PXC variation with polarizer orientation angle θ for (a) microcylinder, (b) microsphere, (c) scarred-MBR, and (d) milled microresonator and TM polarization WGM resonances.

To further explore PXC characteristics, figure 5.8 shows in detail the transmission (top red line), PXC (middle black line), and scattering (bottom orange line) spectra for (a) a microsphere and polarizer angle θ_P = -75°, (b) microsphere and θ_P = -90°, (c) microcylinder and θ_P = +4° and (d) scarred-MBR and θ_P = 0°. It was first observed that in all cases the scattering peaks align very well with the transmission dips, as both are associated with increased internal resonantly enhanced optical energy storage. In contrast, the PXC signal shows a markedly different relation to the transmission dips. It was actually observed that PXC peaks are not well aligned with the transmission dips. Instead, it appears that PXC varies quasi-linearly across the transmission resonances.

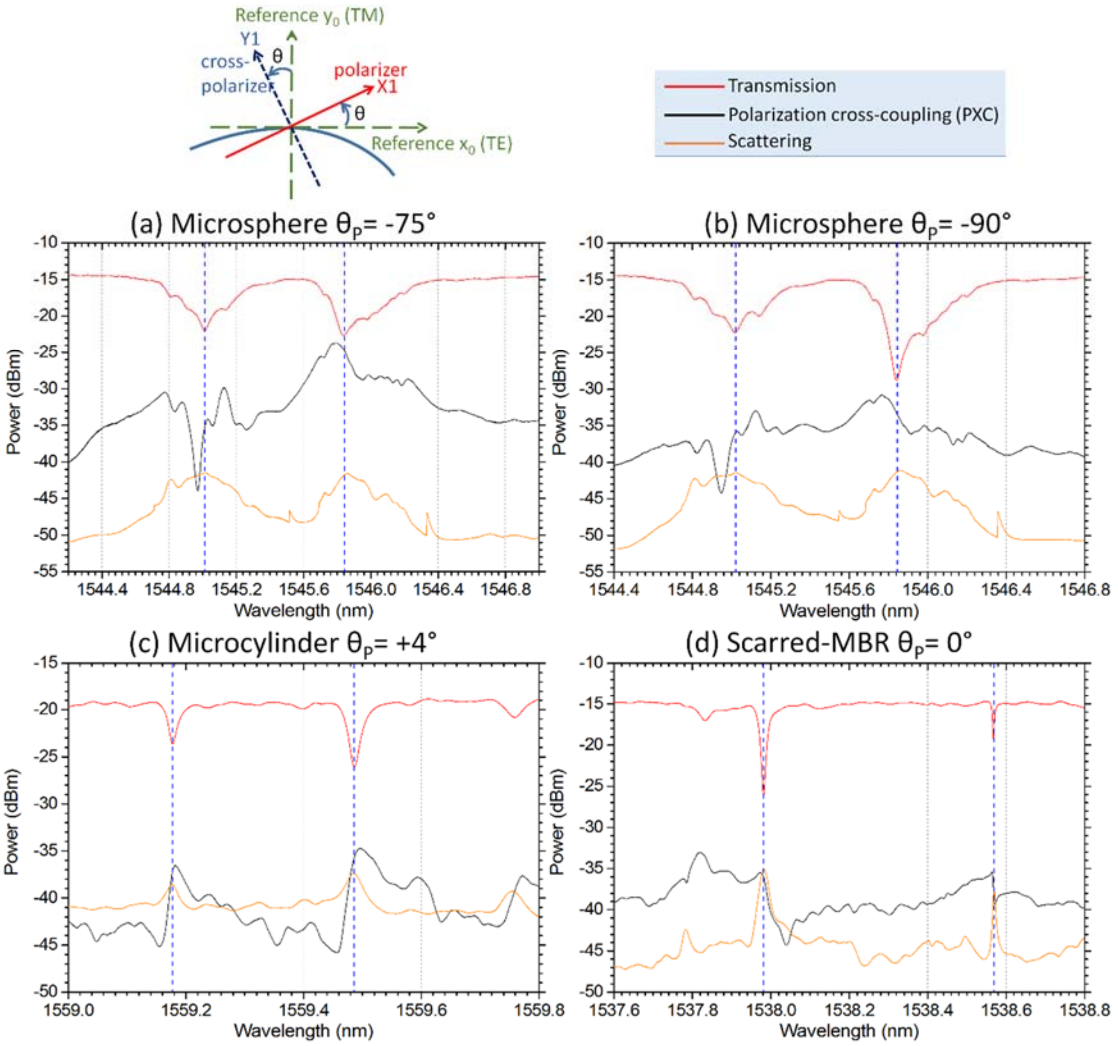

Figure 5.8 transmission, PXC, and scattering spectra for (a) a microsphere and polarizer angle θ_P = -75°, (b) microsphere and θ_P = -90°, (c) microcylinder and θ_P = +4° and (d) scarred-MBR and θ_P = 0°.

5.5 Theoretical analysis

In this section, the unexpected experimental observation of PXC behaviour are being investigated theoretically. Figure 5.9 shows a schematic of the polarization cross-coupling set-up. The electric field of the input polarization is described by a polarization angle θ_0 and ellipse retardation φ_0. The tapered fibre is evanescently coupled to the whispering-gallery microresonator. The output polarizer forms an angle θ_p with the x-axis.

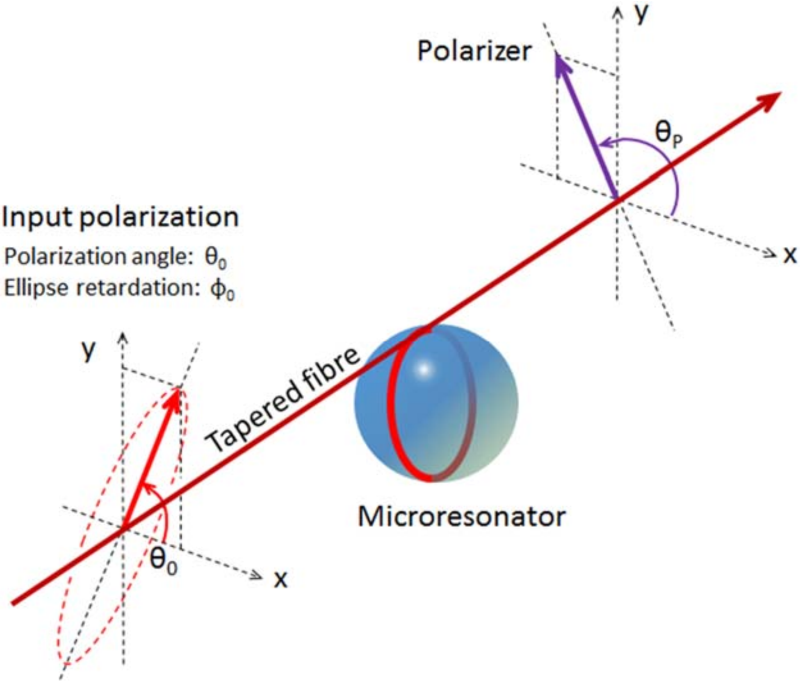

Figure 5.9 Schematic of the transmission and polarization cross-coupling measurement set-up.

Polarization evolution in optical systems is described by the use of Jones calculus [14]. The Jones matrices are given by the following relations:

Input polarization:

$$\boldsymbol{E}_0 = \begin{bmatrix} \cos\theta_0 \\ \sin\theta_0 \exp i\varphi_0 \end{bmatrix} \tag{5.1}$$

Microresonator TE WGM resonance:

$$\boldsymbol{R}_{\mathrm{TE}} = \begin{bmatrix} \tau & 0 \\ 0 & 1 \end{bmatrix} \tag{5.2}$$

Microresonator TM WGM resonance:

$$\boldsymbol{R}_{\mathrm{TM}} = \begin{bmatrix} 1 & 0 \\ 0 & \tau \end{bmatrix} \tag{5.3}$$

Polarizer rotated at an angle θ_{P}:

$$\boldsymbol{P}\theta_P = \begin{bmatrix} cos^2(\theta_P) & sin(\theta_P)cos(\theta_P) \\ sin(\theta_P)cos(\theta_P) & cos^2(\theta_P) \end{bmatrix} \tag{5.4}$$

The polarization state of electric field at the output of the polarizer for TE polarized WGM resonances is given by:

$$\boldsymbol{E}_P = \begin{bmatrix} E_{Px} \\ E_{Py} \end{bmatrix} = \boldsymbol{P}(\theta_P)\boldsymbol{R}_{TE}\boldsymbol{E}_0 \tag{5.5}$$

with $\boldsymbol{R}_{TE}$ is given by equation 5.2. For TM polarized WGM resonances, $\boldsymbol{R}_{TE}$ in equation 5.5 is replaced by $\boldsymbol{R}_{TM}$, given by equation 5.3. The polarizer output intensity I_P is given by:

$$I_P = \boldsymbol{E}_P^{\dagger} \cdot \boldsymbol{E}_P \qquad (5.6)$$

where $\boldsymbol{E}_P^{\dagger} = [E_{Px}^{*} \quad E_{Py}^{*}]$.

In equation 5.2 and 5.3, τ describes the resonance transmission coefficient, given by [15]:

$$\tau = |\tau| \exp(i\varphi) \frac{r - a \exp(i\Delta\varphi)}{1 - ra \exp(i\Delta\varphi)} \qquad (5.7)$$

where a is the resonator round-trip loss, $\Delta\varphi = \left(\frac{2\pi}{\lambda}\right) nR_0$ is the round-trip phase shift, and $r = \sqrt{1-\kappa^2}$ is the coupling transmission coefficient and κ being the tapered fibre/resonator coupling coefficient. The transmission minimum (maximum transmission dip) occurs at resonance ($\Delta\varphi = 0$) is given by:

$$T_{min} = \frac{(a - r^2)}{(1 - ar)^2} \qquad (5.8)$$

Resonances ($\Delta\varphi = 0$) are also associated with maximum internal intensity, stored inside the microresonator cavity, which is given by [15]:

$$I_{int}^{max} = \frac{a^2(1-r)^2}{(1-ar)^2} \qquad (5.9)$$

Figure 5.10 plots the polarizer output intensity I_P given by equation 5.6, as a function of the coupling transmission coefficient r, for resonator round-trip loss $a = 0.8$ and input polarization angle $\theta_0 = 1°$ and $\varphi_0 = 0°$ (linearly polarized light). The output polarizer angle is $\theta_P = \theta_0$. It is shown that at critical coupling ($r = a$), T_{min} acquires the lowest value. For $r < a$, the resonator is over-coupled, while for $r > a$, it is under-coupled. Figure 5.10 (b1) plots the variation of the transmission through the polarizer ($\theta_P = \theta_0$) and (b2) the resonance transmission phase as a function of the round-trip phase (achieved by the input wavelength shift), for coupling transmission coefficient $r = 0.895$ and $r = 0.63$. It is shown that for $r = 0.895$ (under-coupled) and $r = 0.63$ (over-coupled) resonances the minimum transmission acquires the same value (≈ -10 dB). However, the under-coupled resonance shows higher Q-value and a transmission phase shift (at resonance) equal to zero. On the other hand, the corresponding over-coupled resonance for the same transmission dip shows lower Q and a resonance transmission shift of π.

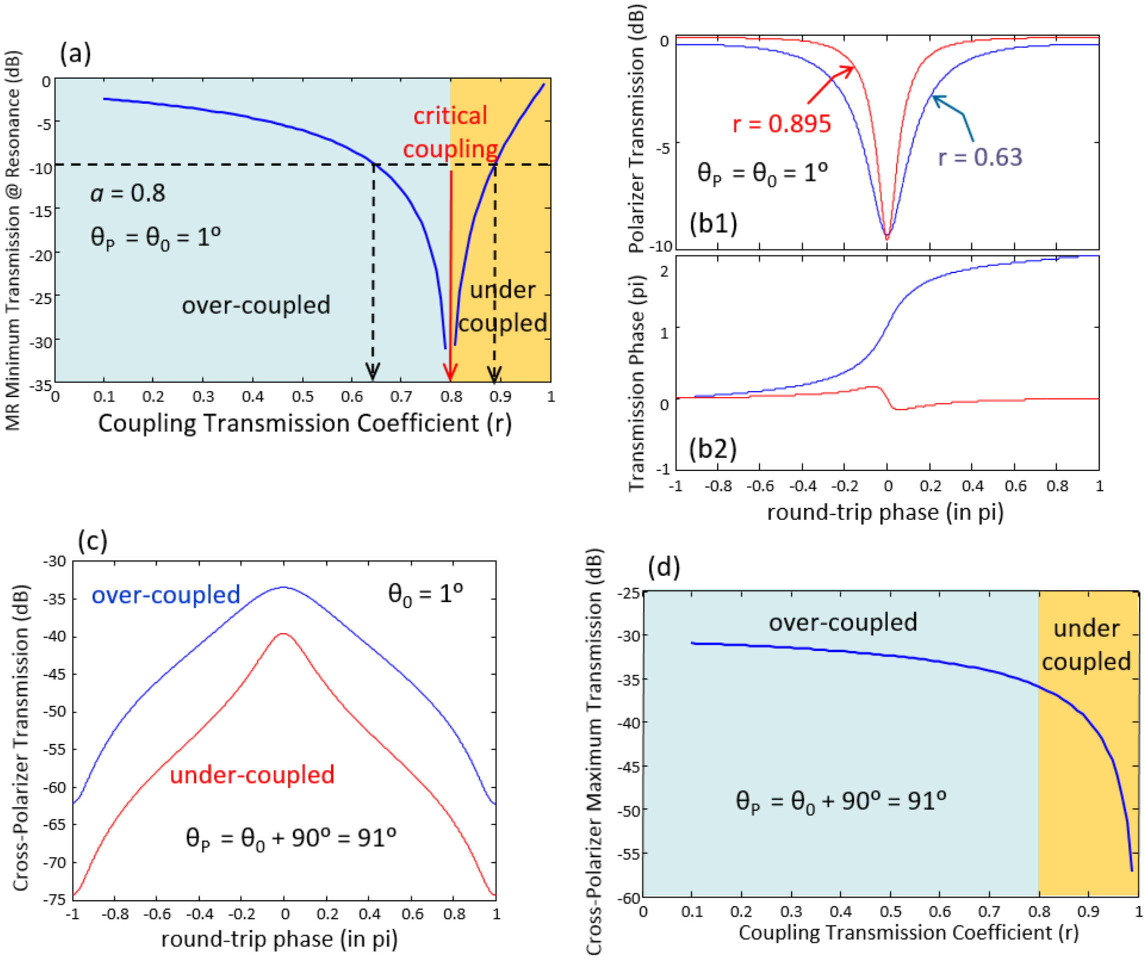

Figure 5.10 (a) the polarizer output intensity $\boldsymbol{I_P}$ as a function of the coupling transmission coefficient *r*, for resonator round-trip loss *a* = 0.8 and input polarisation angle $\theta_0 = 1°$ and $\varphi_0 = 0°$ (linearly polarized light). The output polarizer angle is $\theta_P = \theta_0$. (b1) variation of the transmission through the polarizer $(\theta_P = \theta_0)$ and (b2) the resonance transmission phase as a function of the round-trip phase, for coupling transmission coefficient *r* = 0.895 and 0.63. (c) cross-polarizer transmission $(\theta_P = \theta_0 + 90°)$, as a function of the coupling transmission coefficient *r*, for resonator round-trip loss *a* = 0.8 and input polarisation angle $\theta_0 = 1°$ and $\varphi_0 = 0°$. (d) cross-polarizer transmission maximum (PXC peak) as a function of the coupling transmission coefficient (*r*).

Figure 5.10 (c) plots the cross-polarizer transmission $(\theta_P = \theta_0 + 90°)$ as a function of the coupling transmission coefficient *r*, for resonator round-trip loss *a* = 0.8 and input polarisation angle $\theta_0 = 1°$ and $\varphi_0 = 0°$. It is shown that the cross-polariser transmission is maximum at resonance (round-trip phase shift $\Delta\varphi = 0$), both for the over-coupled and under-coupled resonances. Figure 5.10 (d) plots the cross-polarizer transmission maximum (PXC peak) as a function of the coupling transmission coefficient (*r*). It is shown that the cross-polarizer transmission maximum (PXC peak) increases with decreasing coupling transmission coefficient (*r*), and therefore, it is larger for over-coupled resonances.

Figure 5.10 (c) shows that the cross-polarizer transmission (polarization cross-coupling - PXC) for linearly polarized input light is symmetric with respect to resonant wavelength (round-trip phase shift $\Delta\varphi = 0$) This is in sharp contrast with the experimental observations discussed in figure 5.8.

Figure 5.11 plots (a) the polarizer output intensity I_P $(\theta_P = \theta_0)$ and (b) the cross-polarizer output intensity I_P $(\theta_P = \theta_0 + 90°)$ as a function of the round-trip phase shift $\Delta\varphi$ for resonator round-trip loss $a = 0.8$, coupling transmission coefficient $r = 0.895$ (under-coupled) and input polarization angle $\theta_0 = 1°$ and $\varphi_0 = 0°$ to $90°$ (elliptically polarized light). It is observed that the cross-polarizer output intensity (polarization cross-coupling – PXC) shows progressively more pronounced asymmetric behaviour with the round-trip phase shift $\Delta\varphi$ (or equivalently the wavelength shift) as the input light ellipticity increases. Figure 5.11 also plots (c) the polarizer output intensity I_P $(\theta_P = \theta_0)$ and (d) the cross-polariser output intensity I_P $(\theta_P = \theta_0 + 90°)$ as a function of the round-trip phase shift $\Delta\varphi$ for an under-coupled $(r = 0.895)$ and over-coupled $(r = 0.63)$ resonance for input polarization angle $\theta_0 = 1°$ and $\varphi_0 = 9°$. It is shown that the over-coupled resonance produces larger and more asymmetric PXC.

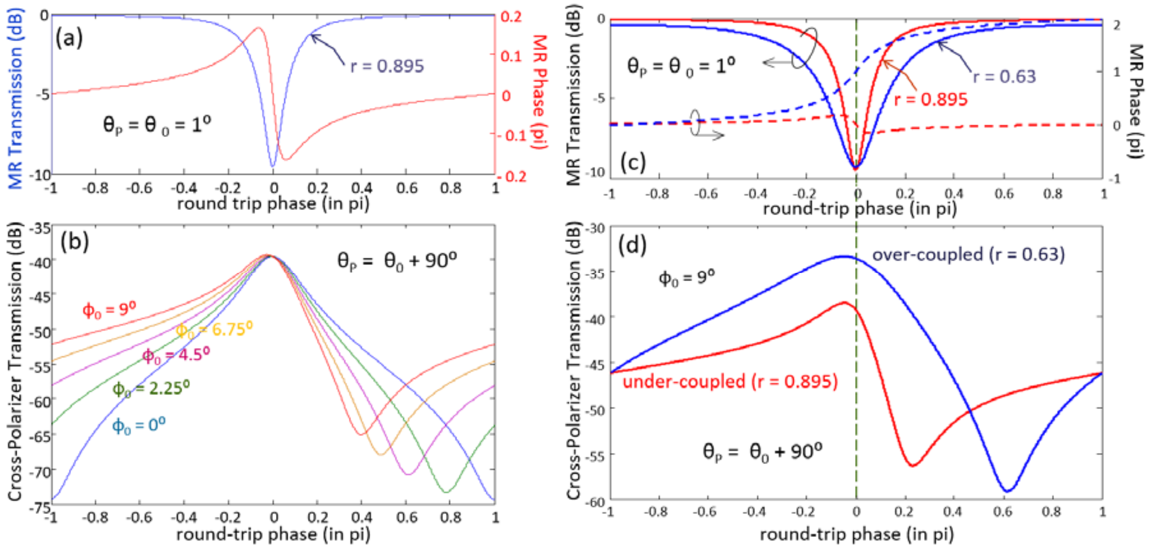

Figure 5.11 (a) polarizer output intensity $\boldsymbol{I}_P$ $(\theta_P = \theta_0)$ and (b) the cross-polarizer output intensity $\boldsymbol{I}_P$ $(\theta_P = \theta_0 + 90°)$ as a function of the round-trip phase shift $\Delta\varphi$ for resonator round-trip loss a = 0.8, coupling transmission coefficient r = 0.895 (under-coupled) and input polarization angle $\theta_0 = 1°$ and $\varphi_0 = 9°$ (elliptically polarized light), (c) the polarizer output intensity $\boldsymbol{I}_P$ $(\theta_P = \theta_0)$ and (d) the cross-polarizer output intensity $\boldsymbol{I}_P$ $(\theta_P = \theta_0 + 90°)$ as a function of the round-trip phase shift $\Delta\varphi$, for an under-coupled (r = 0.895) and over-coupled (r = 0.63) resonance for input polarization angle $\theta_0 = 1°$ and $\varphi_0 = 9°$.

Comparing the experimental results in figure 5.8 with the theoretical predictions in figure 5.11 it was realized that the observed PXC asymmetries around the WGM resonances are mainly due to the residual ellipticity of the input polarization. All-fibre polarization controllers, based on fibre loops, are known to have bend-induced birefringence and cannot provide endlessly- and perfectly-controlled polarization. In addition, the degree of polarization control is wavelength dependent. The measured PXC asymmetry can be used to assess the degree of linear polarization provided by the polarization controllers. Furthermore, the relative PXC level can be used to determine whether equally strong WGM resonances are over-coupled or under-coupled.

Figure 5.12 plots the PXC peak as a function of the input polarization angle θ_0, for under-coupled ($r = 0.895$) and over-coupled ($r = 0.63$) WGM resonances. It was observed that PXC is symmetric around $\theta_0 = 0°$, with the minimum PXC taking place at $\theta_0 = 0°$. PXC maxima, on the other hand, occurred at $\pm 45°$. It was also noticed that PXC for over-coupled resonances is higher than for the under-coupled resonances, through all input polarization angles. Comparing the experimental results in figure 5.6 and 5.7 with the theoretical results in figure 5.12, it was observed that although the theory reproduces accurately the shape of the PXC variation with input polarization angle, it does not predict the observed shift the central PXC dip from $\theta_0 = 0°$.

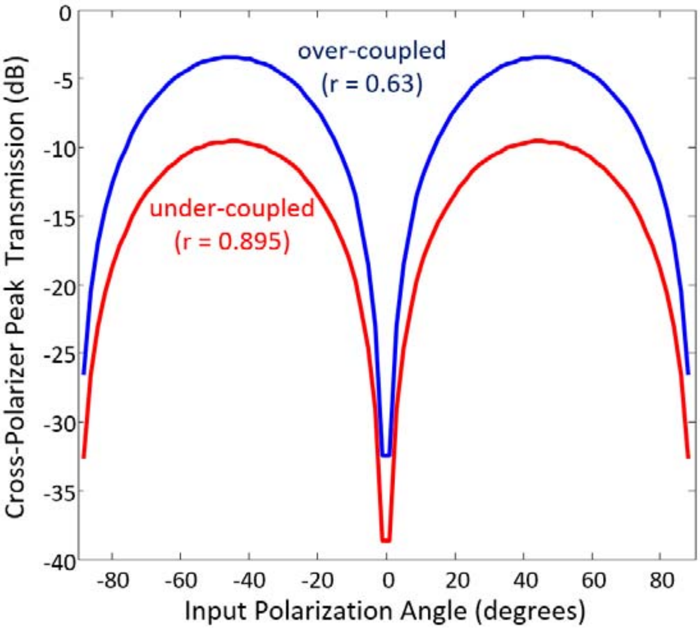

Figure 5.12 PXC peak as a function of the input polarisation angle θ₀, for under-coupled ($r = 0.63$) and over-coupled ($r = 0.895$) WGM resonances.

So far, in developing the theoretical model it had been assumed that the tapered fibre is uniform with no preferential polarization axes. However, it is known that micro-taper fibres of small diameters show a sizeable birefringence, due to small deviations from waist circularity [16]. In addition, small residual stresses can result in elliptical birefringence. Micro-taper fibres also known to be easily twisted, due to their small cross-section. To account for the residual birefringence and twist of the output part of the tapered fibre, an equivalent rotated retarder was added between the microresonator and the output polarizer, as illustrated in figure 5.13.

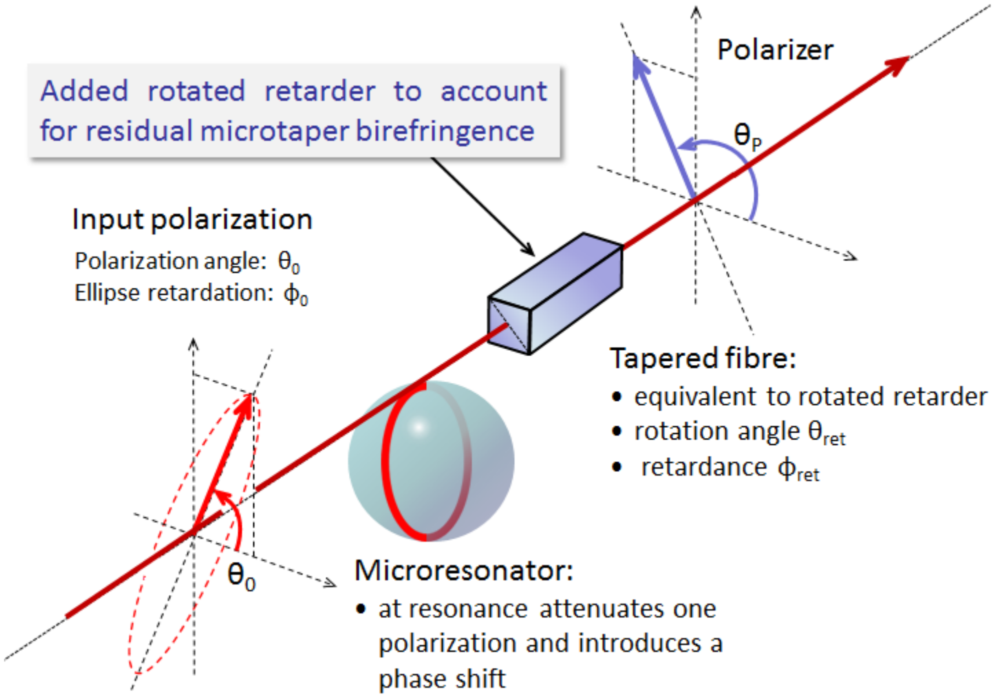

Figure 5.13 Schematic of the transmission and polarization cross-coupling measurement set-up, with a rotated retarder added between the microresonator and the output polarizer.

The added rotated retarder is characterised by a rotation angle θ_{RET} and φ_{RET}. The corresponding Jones matrix is given by:

$$\boldsymbol{R}_{RET} = \begin{bmatrix} p_{11} & p_{12} \\ p_{21} & p_{22} \end{bmatrix} \tag{5.10}$$

where

$$\begin{aligned} p_{11} &= \cos(\varphi_{RET}/2) + i\sin(\varphi_{RET}/2)\cos 2\theta_{RET} \\ p_{12} &= i\sin(\varphi_{RET}/2)\cos(2\theta_{RET}) \\ p_{21} &= i\sin(\varphi_{RET}/2)\cos(2\theta_{RET}) \\ p_{22} &= \cos(\varphi_{RET}/2) - i\sin(\varphi_{RET}/2)\cos(2\theta_{RET}) \end{aligned}$$

In this case the polarization state of electric field at the output of the polarizer for TE polarised WGM resonances is given by:

$$\boldsymbol{E}_P = \begin{bmatrix} E_{Px} \\ E_{Py} \end{bmatrix} = \boldsymbol{P}(\theta_P)\boldsymbol{R}_{RET}\boldsymbol{R}_{TE}\boldsymbol{E}_0 \tag{5.11}$$

with $\boldsymbol{R}_{TE}$ given by equation (5.2). For TM polarized WGM resonances, $\boldsymbol{R}_{TE}$ in equation (5.11) is replaced by $\boldsymbol{R}_{TM}$, given by equation (5.3). The polarizer output intensity I_P is given by equation (5.6).

Figure 5.14 (a) plots the PXC peak as a function of the input polarization angle $\theta_0 = 0°$, for under-coupled ($r = 0.895$) WGM resonance, for a retarder rotation $\theta_{RET} = +9°$ and retardence

$\varphi_{RET} = 18°,\ 36°, 54°$ and $72°$. The curve without the retarder is also included for comparison. It could be observed that after the introduction of the retarder, the PXC variation with input polarization angle θ_0 is no longer symmetric around angle $\theta_0 = 0°$. It was also observed that increasing the retardation results in larger shifts of the central PXC dip, in close agreement with the experimental results. Figure 5.14 (b) plots the PXC peak as a function of the input polarization angle θ_0 for under-coupled ($r = 0.895$) WGM resonance, for a retardence $\varphi_{RET} = +72°$ and retarder rotation $\theta_{RET} = +9°$ and $-9°$. It could be observed that for a given retardance, the sign of the retarder rotation angle defines the direction of the central PXC dip shift.

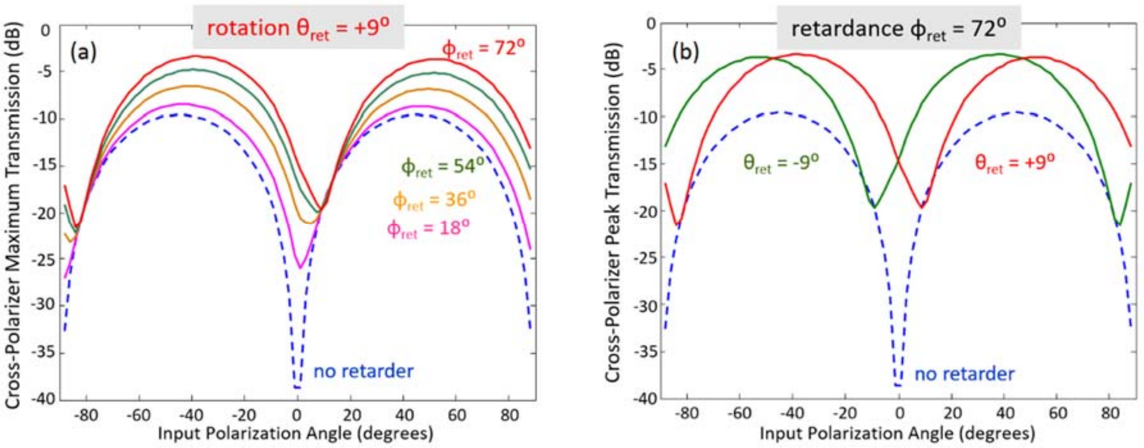

Figure 5.14 PXC peak as a function of the input polarization angle θ_0, for under-coupled ($r = 0.895$) WGM resonances for (a) retarder rotation $\theta_{RET} = +9°$ and retardence $\varphi_{RET} = 18°,\ 36°, 54°$ and $72°$ (and without retarder for comparison), and (b) for retardence $\varphi_{RET} = 72°$ and retarder rotation $\theta_{RET} = +9°$ and $\theta_{RET} = -9°$.

Figure 5.15 plots the variation of the transmission dip (a) & (d), PXC peak (b) & (e) and scattered peak power (c) & (f) as a function of the polarizer and input polarization angle θ_0 for TE-polarized WGM resonance ((a), (b), (c)), and TM-polarized WGM resonances ((d), (e), (f)). The resonances are characterized by a resonator round-trip loss $a = 0.8$ and coupling transmission $r = 0.895$. We consider the case with an equivalent retarder with parameters $\theta_{RET} = -18°$ and $\varphi_{RET} = 36°$ (blue lines). The case without additional retarder ($\theta_{RET} = 0°$ and $\varphi_{RET} = 0°$) is also included for comparison (red lines). The transmission dip and PXC peak is calculated from equations (5.11) and (5.6) with $\theta_P = \theta_0$ and $\theta_P = \theta_0 + 36°$, respectively, and equation (5.2) and (5.3) for TE- and TM-polarized WGM resonances, respectively. The scattered peak power is proportional to the maximum internal intensity, stored inside the microresonator cavity, which is calculated by equation (5.9).

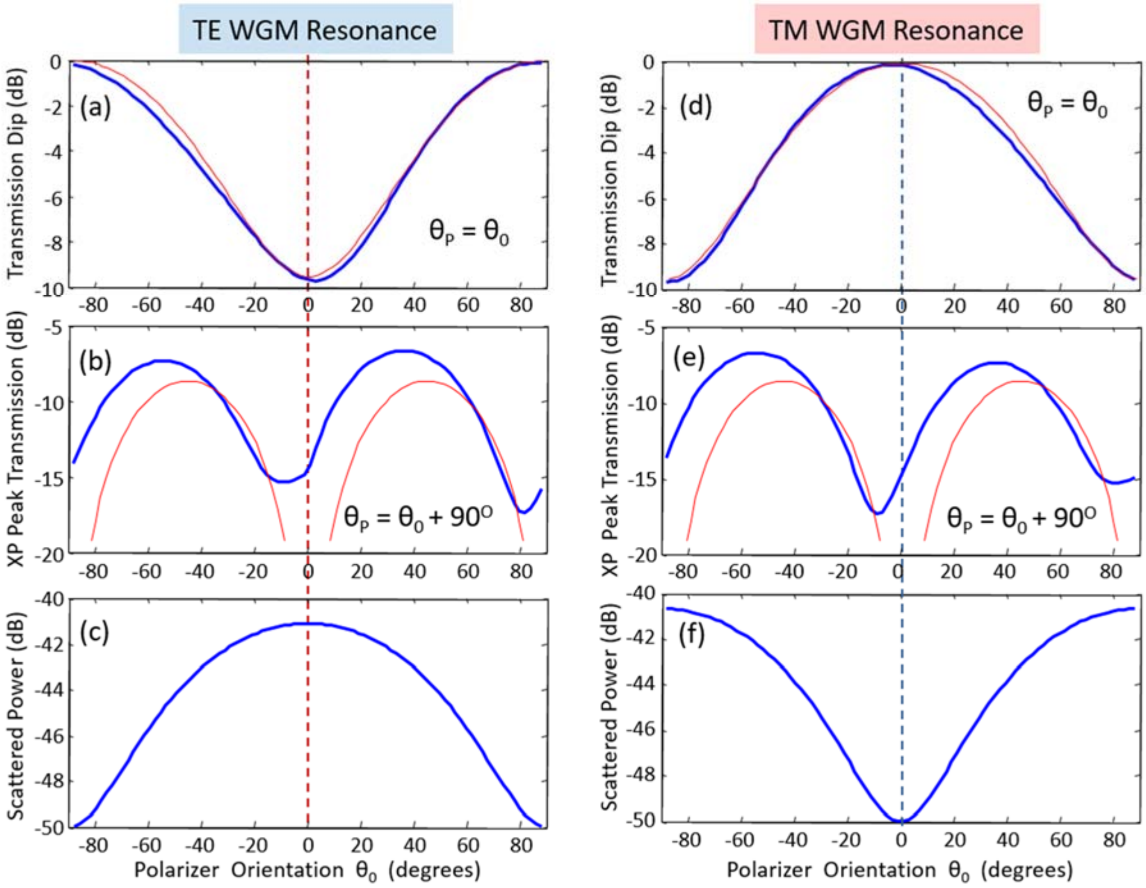

Figure 5.15 Variation of (a) & (d) transmission dip, (b) & (e) PXC peak, and (c) & (f) scattered peak power as a function of the polarizer and input polarization angle θ_0. TE-polarized WGM resonance ((a), (b), (c)), and TM-polarized WGM resonances ((d), (e), (f)). The resonance was characterized by resonator round-trip loss $a = 0.8$, and coupling coefficient transmission $r = 0.895$. The equivalent retarder parameters are $\theta_{RET} = -18°$ and $\varphi_{RET} = -36°$ (blue lines). The case without an additional retarder is included for comparison (re lines).

By comparing the experimental results in figure 5.5 and theoretical calculations in figure 5.15 it shows that the addition of the retarder fully accounts for the observed dependencies of the transmission dip, PXC peak and scattered peak power on the polarizer and input polarization angle. It is shown that the transmission dip and PXC peak minima are shifted from $\theta_0 = 0°$ due to additional retardation introduced by the output part of the micro-taper. However, because this part of the micro-taper follows the microresonator and does not affect scattering out process, the scattered power curves with and without retarder overlap with each other. In addition, scattered power extrema are not shifted with respect to $\theta_0 = 0°$. From these results, it is deduced that since scattered power is not affected by the additional birefringence the output micro-taper, it can be used for accurate polarization alignment.

5.7 Summary

Optical microresonators are characterized by distinctive families of TE- and TM-polarized WGM resonances. The polarization state of the evanescently launched lights affects the number, type and strength of each resonance. In this chapter a polarimetric set-up was utilized to investigate the evolution of the transmission dips, PXC peaks and scattered light as the input polarization is changed. The polarization was aligned by using wavelengths outside the WGM resonances. Four different MRs were tested, namely, a microsphere, a cylindrical MR, a milled MR and a scarred-MBR. It is shown that the transmission dip and PXC minima are shifted with respect to the ideally expected input polarization angle. A theoretical model based on Jones matrix calculus was also developed which have attributed the observed shifts to the residual birefringence of the output part of the micro-taper fibre, used for evanescent launching into the MRs. The model demonstrated that the scattered light is not affected by this residual birefringence and therefore it is a better metric to ensure accurate TE or TM polarization launching.

It was also observed that microresonators with tighter axial power confinement, such as MBRs and micro-milled resonators, show larger cross-polarization coupling efficiencies and they should be preferred as polarization converters. In the case of micro-cylinder resonators, the lack of axial mode confinement results in the smallest and almost polarization independent cross-polarization coupling. Additionally, it is also shown that utilizing the TE WGM resonances results in superior cross-polarization performance.

Finally, it was observed that by using on-resonance wavelengths for the purpose of polarization alignment did not provide any fine tuning and resulted in much inferior alignment results (the results not included in this thesis).

5.8 References

[1] K. J. Vahala, “Optical microcavities,” *Nature* **424**, 839 (2003).

[2] V. Lefèvre-Seguin, “Whispering-gallery mode lasers with doped silica microspheres,” *Optical Materials* **11**, 153 (1999).

[3] D. K. Armani, T. J. Kippenberg, S. M. Spillane, and K. J. Vahala, “Ultra-high-Q toroid microcavity on a chip,” *Nature* **421**, 925 (2003).

[4] G. S. Murugan, J. S. Wilkinson, and M. N. Zervas, “Optical microdiscus resonators by flattening microspheres,” *Applied Physics Letters* **101**, 071106 (2012).

[5] G. S. Murugan, J. S. Wilkinson, and M. N. Zervas, "Selective excitation of whispering gallery modes in a novel bottle microresonator," *Optics Express* **17**, 11916-11925 (2009).

[6] M. Sumetsky, Y. Dulashko, and R. S. Windeler, “Optical microbubble resonator,” *Optics Letters* **35**, 898 (2010).

[7] G. Guan and F. Vollmer, “Polarized transmission spectra of the fiber-microsphere system,” *Applied Physics Letters* **86**, 121115 (2005).

[8] B. E. Little and S. T. Chu, "Theory of polarization rotation and conversion in vertically coupled microresonators," *IEEE Photonics Technology Letters* **12**, 401 (2000).

[9] P. Bianucci, C. R. Fietz, J. W. Robertson, G. Shvets, and C.-K. Shih, "Whispering gallery mode microresonators as polarization converters," *Optics Letters* **32**, 2224 (2007).

[10] P. Bianucci, C. R. Fietz, J. W. Robertson, G. Shvets, and C.-K. Shih, "Polarization conversion in a silica microsphere," *Optics Express* **15**, 7000 (2007).

[11] D. R. Rowland and J. D. Love, "Evanescent wave coupling of whispering gallery modes of a dielectric cylinder," *IEE Proceedings J – Optoelectronics* **140**, 177 (1993).

[12] S. Bakhtiari Gorajoobi, G. Senthil Murugan, and M. N. Zervas, "Yb^{3+}-doped Silica WGM Milled Microrod laser," *CLEO: 2015*, OSA Technical Digest, paper SF1H.7 (2015).

[13] M. Ding, G. S. Murugan, G. Brambilla, and M. N. Zervas, “Whispering gallery mode selection in optical bottle microresonators,” *Applied Physics Letters* **100**, 081108 (2012).

[14] http://scienceworld.wolfram.com/physics/JonesMatrix.html

[15] A. Yariv, "Universal relations for coupling of optical power between microresonators and dielectric waveguides," *Electronics Letters* **36**, 321-322, (2000).

[16] H. Xuan, J. Ju, and W. Jin, "Highly birefringent optical microfibers," *Optics Express* **18**, 3828 (2010).

Chapter 6: Hybrid whispering-gallery mode plasmonics microbottle resonator

6.1 Introduction

While dielectric cavities have been demonstrated to perform efficiently on the micro-scale region through the incorporation of whispering-gallery resonators [1], surface plasmons (SPs) cavities have mostly been demonstrated in the subwavelength scale with *Q*-factor values much lower than the theoretical limit [2]. SPs are transverse-magnetic (TM) in character and requires electric fields normal to the surface of the conductor (usually metal) in order to generate the surface charge. Light waves which are "trapped" would cause the free electrons on the surface of the conductor to oscillate in resonance with them. The cause which limits the performance of SP devices are primarily due to their intrinsic loss elements – owing mainly to the ohmic loss in metals. Numerous approaches have been investigated in enhancing the performance of SP cavities with slight accomplishments achieved in the nanoscale region through the incorporation of whispering-gallery modes (WGMs) cavity structures [3 -5]. In the microscale region, it has been demonstrated that plasmonics cavity with *Q*-values near theoretical limit could be realized with the utilization of a high-*Q* WGM silica microdisc resonator [6]. The top of the microdisc was coated with a thin layer of silver for surface plasmon waves (SPWs) generation with the entire excitation process took place at the dielectric part of the disc. *Q*-factor value of WGM cavity which supports SPP in the range of 1400 was successfully demonstrated. The enhancement cavities which support SPPs through the incorporation of dielectric structure were explored further with other types of established WGM optical resonators such as microtoroid [7], microcylinder [8], microsphere [9], and microbottle [10].

To date, all of the reported hybrid-plasmonics cavities which incorporated optical WGM devices had been demonstrated with uniform thickness of thin metal-film for SPP generation. In this chapter, we report the performance of a hybrid whispering-gallery plasmonics microbottle (MBR) resonator with varying thin metal-film thickness. Fabrication of the plasmonics-MBR and the experimental set-up utilized to characterize the resonator performance are presented in section 6.2. Section 6.3 presents detailed study of the measured transmitted spectra with various polarization input light and MBR axial excitation. Study of the hybrid plasmonics-MBR with different tapered fibre coupling arrangement relative to the position of the thin metal-film are shown in detail in section 6.4. For additional insight, section 6.5 discusses FDTD simulation results of a WGM microdisc resonator with varying thickness of thin metal-film on its surface for SPPs generation.

6.2 Fabrication of hybrid whispering-gallery mode plasmonics microbottle resonator and polarization resolved experimental set-up

The optical MBR utilized for the hybrid-plasmonics device was fabricated through the "soften-and-compress" technique [11] using a conventional single-mode fibre (SMF). The MBR fabricated attained maximum bottle diameter of $D_b = 181\ \mu\mathrm{m}$ and neck-to-neck length of $L_b = 400\ \mu\mathrm{m}$. The MBR shape fit a harmonic-oscillator parabolic profile with its WGM numbers being defined by *m* (azimuthal), *p* (radial) and *q* (axial) order [12,13]. For SPP generation, a thin gold (Au) film was deposited on one side of the MBR surface through metal-evaporation process. Due to surface curvature of the MBR, the thin metal-film only covers half of the resonator surface with a meniscus profile and 30 nm maximum thickness. The meniscus metal film profile creates appropriately tapered edges on the two sides of the MBR that would facilitate the low-loss adiabatic transformation of the MBR-WGMs to SPPs, and vice versa. Figure 6.1 shows the fabricated plasmonics-MBR imaged at (a) 0 nm and (b) 30 nm thick gold. The schematic cross-section of the plasmonics-MBR with the meniscus thin gold film on its surface is shown in (c).

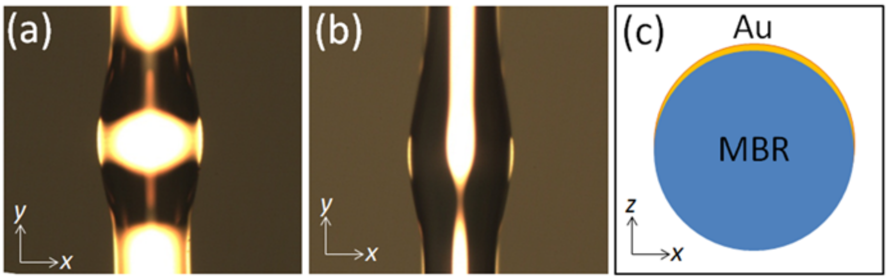

Figure 6.1 Plasmonics-MBR surface with (a) 0 nm and (b) 30 nm thick gold. (c) Schematic cross-section of the plasmonics MBR with meniscus thin metal-film profile.

For distinguishing TE- and TM-excited whispering-gallery mode resonances, a polarization resolved set-up is required to fully characterize the performance of the hybrid resonator. Figure 6.2 (a) illustrates the schematic of the polarization-resolved set-up utilized in the experiment with an adiabatic tapered optical fibre utilized to couple light evanescently into the cavity of the micoresonator [14]. To control the polarization of input the light launched from a tuneable laser source (TLS), a standard SMF linked to a series of polarization controllers (PCs) was set in the system. The other end of the SMF was spliced to an adiabatic tapered fibre that was cleaved at its 2 μm waist region. The plasmonics-MBR was positioned below and in physical contact with the tapered fibre at the dielectric part of the resonator (0 nm thick gold) for efficient evanescent light coupling into the microcavity [6]. The output transmitted light from the cleaved tapered fibre was collimated by an objective lens of 0.65 NA (*L1*) and was guided in free-space to pass through a highly discriminating polarizer (> 45 dB). The polarizer was set in a way where it can be freely rotated to any angle and move in and out of the system indefinitely. Another objective lens (*L2*) was positioned after the polarizer in order to focus the transmitted light down into a multimode fibre (MMF). The other MMF end was connected to a high range InGaAs optical power meter (+10 to -80 dBm) for accurate transmitted power measurements. The efficiency of the proposed polarization-resolved system in discriminating TE and TM light was characterized to be > 20 dB, comparable to the performance of an advanced polarization-maintaining optical microfibre [15]. Figure 6.2 (b) shows light scattering by the plasmonics-MBR under test when the tapered fibre was connected to a He-Ne laser source during pre-alignment process of the polarization-resolved system.

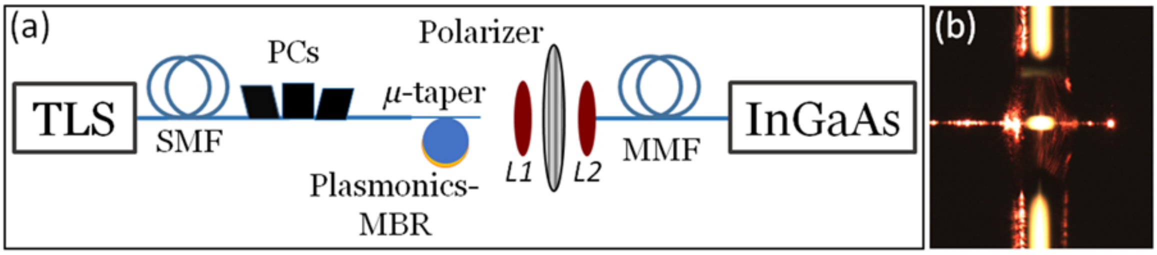

Figure 6.2 (a) Schematic of the polarization-resolved experimental set-up. (b) Light scattering by the plasmonics-MBR under test with the tapered fibre input-end connected to a He-Ne laser source.

6.3 Excitation of hybrid plasmonics microbottle resonator whispering-gallery modes

The tapered optical fibre was arranged to couple light to the plasmonics-MBR central axial position. Polarization of the input light from the TLS was set to various polarization angle by tuning the polarization controllers and monitoring the throughput power value after it has passed the highly discriminating polarizer of a set rotation angle. Narrow-linewidth laser (~ 100 kHz) from the TLS was swept over a broad range (20 nm) with the output transmission being recorded by the InGaAs power meter at 1.0 pm resolution. Figure 6.3 shows transmitted spectra of the hybrid plasmonics-MBR at various input light polarization θ_P coupled through the 0 nm thick-gold-section. At 0° polarization, the coupled light into the cavity of the hybrid plasmonics-MBR was purely TM. A maximum whispering-gallery transmission dip of 5 dB (~ 70% coupling efficiency) was generated with free spectral range (FSR) of ~ 3 nm. The TM resonance was calculated to attain a Q-factor value ($Q = \lambda/\Delta\lambda$) in the range of 850. Tuning the input polarization of light to $10°$ and $20°$ did not change the profile of the transmitted spectra much. However, at $30°$ polarization orientation, the transmitted spectra started to pick-up additional resonance dips with decreasing overall transmission dip. Tuning the polarization angle further revealed that the additional resonance dips are actually TE resonance modes and they became dominant at $50°$. Starting from $70°$ to $90°$, TM resonance modes diminish with higher transmission dips of the TE resonance modes. With pure TE input light polarization, resonance dips which do not correspond to TM resonance wavelengths are generated. A maximum resonance transmission dip of ~ 18 dB (~ 90% coupling efficiency) was generated with a FSR of ~ 3 nm. The higher WGM excitation strengths generated by TE resonances are expected since input TE light interact less with the thin metal-film and are confined within the dielectric part of the plasmonics-MBR. As such, the *Q*-factor value of TE resonances are also higher reaching 2100. With TM polarized light, the coupled light would penetrate and interact more with the thin-metal film as it resonates on the surface of the hybrid resonator, yielding higher loss. This would force the electric field to be normal to the surface of the meniscus thin gold-film for SPPs generation on the surface of the metal (gold).

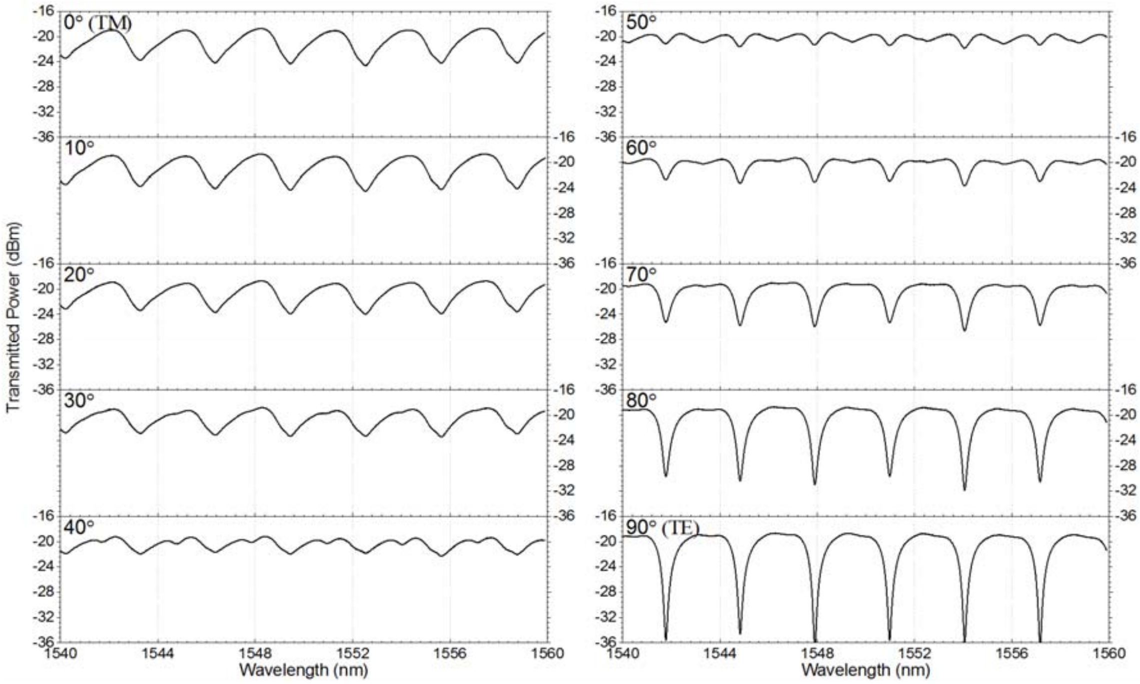

Figure 6.3 Transformation of the plasmonics-MBR transmitted spectra excited at the centre position with input light polarization tuned from 0° (TM) to 90° (TE).

Due to the fact that WGM MBRs are able to support high number of modes, Lorentzian fittings were performed on the measured transmitted spectra in order to identify individual whispering-gallery resonance modes. Figure 6.4 shows the Lorentzian fitting and *Q*-factor values of individual TE excited resonances ($\theta_P = 90°$) over the 1542 – 1558 nm wavelength span. The Lorentzian fitting was performed in a manner where the cumulative fit peak (combination of each individual resonances) would best fit the measured data. In this case, the cumulative fit peak traces the measured data almost perfectly making the two of them nearly identical. The insertion loss (difference in baseline between the measured and Lorentzian fitted data) was calculated to be ~ 0.4 dB. It was observed that each measured resonance dip (family group-mode) actually comprises of two main overlapping WGM dips (orange and purple lines) with ~ 3 nm FSR. While the composite *Q*-factor value of the measured data is in the range of 2100, the Lorentzian-fitted individual resonance *Q*-factor values are much higher, reaching 2900.

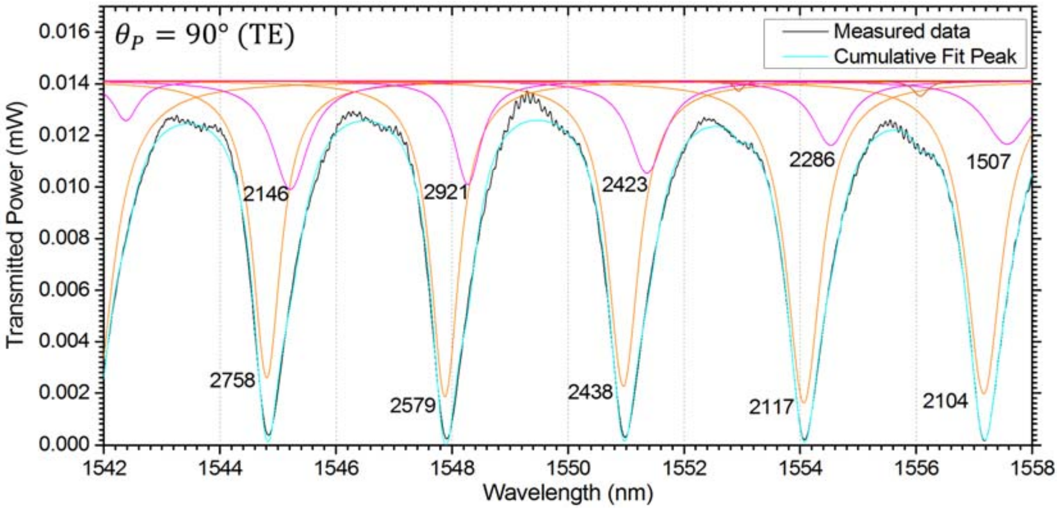

Figure 6.4 Measured TE transmission of the plasmonics-MBR excited at the centre (black line), Lorentzian fittings and their *Q*-factor values (orange & purple lines), and cumulative fit peak of the Lorentzian fittings (light blue line).

Since SPPs are transverse-magnetic in character, only TM-polarized light coupled into the hybrid plasmonics-MBR cavity would excite electron density oscillations on the surface of the gold (metal-air interface). Figure 6.5 shows the Lorentzian fitting and *Q*-factor of individual TM excited resonances ($\theta_P = 0°$) over the 1542 – 1558 nm wavelength span. Accurate Lorentzian fitting was again performed so that the cumulative fit peak would best fit to the whole broad range of the measured transmitted data. Based from the Lorentzian fitting, each of the measured resonance dip (family group-mode) comprises of three overlapping resonances (red, blue and green lines) with a FSR of ~ 3 nm. Baseline drop of the Lorentzian fitting and the measured data is ~ 1.5 dB. The three resonances composite *Q*-factor measured directly from the measured data was in the range of 850. However, as shown in the figure, the *Q*-factor values of the individual resonances are much higher. The highest *Q*-factor calculated was in the range of 2500, corresponding to the resonance centred at 1549.5 nm.

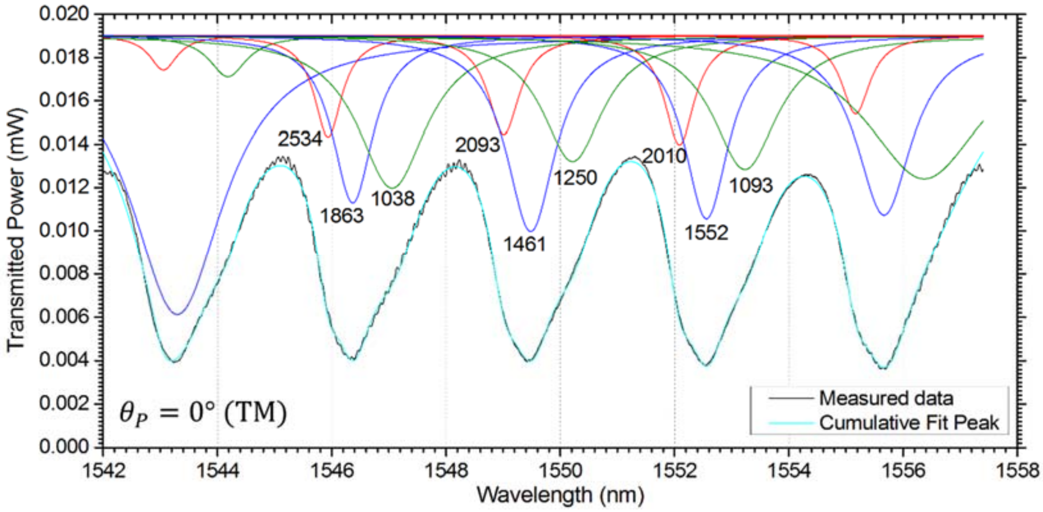

Figure 6.5 Measured TM transmission of the plasmonics-MBR excited at the centre (black line), Lorentzian fittings and their *Q*-factor values (red, blue & green lines), and cumulative fit peak of the Lorentzian fittings (light blue line).

A Lorentzian fitting was also performed on the measured data when the coupled polarization light was aligned at $\theta_P = 45°$ (equal TE- and TM-polarized light). As shown in figure 6.6, the fitting consists of both TE-excited (orange and purple lines) and TM-excited (red, blue and green lines) WGM resonances, resulting to a more complex and dense spectrum. Baseline drop of the Lorentzian fitting and the measured data is ~ 1.5 dB.

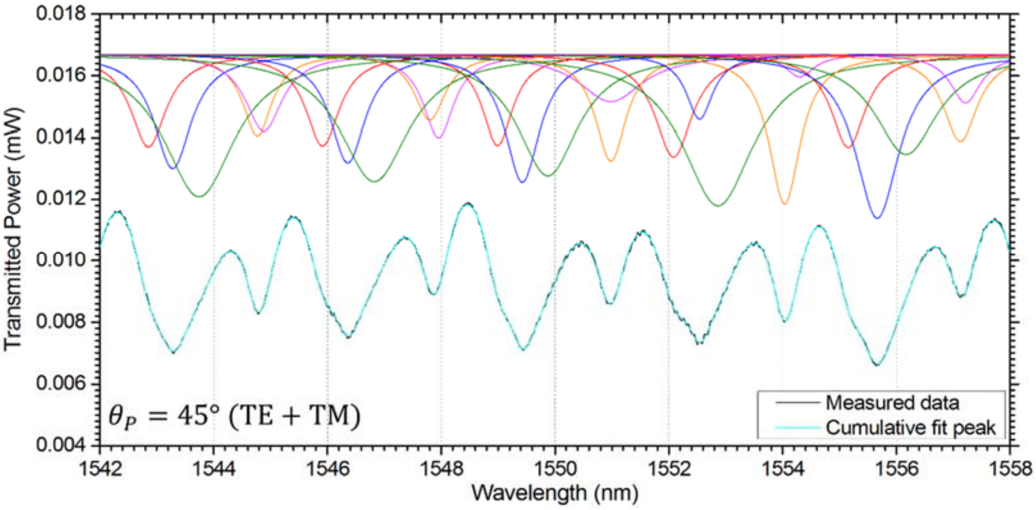

Figure 6.6 Measured transmission of the plasmonics-MBR excited at the centre (black line) with input polarization aligned at $\theta_P = 45°$ (equal TE and TM polarized light). Lorentzian fittings of the measured data correspond to TE- (orange & purple lines) and TM-WGM resonances (red, blue & green lines), and cumulative fit peak of the Lorentzian fittings (light blue lines).

The performance of the plasmonics-MBR was also studied with various tapered fibre excitation arrangements. The tapered fibre was coupled at different positions along the axial path of the plasmonics-MBR away from the centre with TE- and TM-polarized input light. Figure 6.7 shows the transmitted resonance spectra of the plasmonics-MBR when the tapered fibre was coupled at (a) & (e) centre, (b) & (f) 1 μm-off centre, (c) & (g) 2 μm-off centre, and (d) & (h) 28 μm-off centre over the 1540 – 1560 nm wavelength range. Figure 6.7 (a) shows that launching TE-polarized light at the plasmonics-MBR centre position excites six distinguishable fundamental WGM transmission dips with a high excitation strength of > 20 dB. Additional WGM transmission dips with ~ 2 dB excitation strength were observed through the transmitted spectrum when the tapered fibre was placed 1 μm-off centre, as in Figure 6.7 (b). This corresponds to the hybrid-MBR higher axial *q*-order WGMs. The generation of these higher order *q*-modes caused the excitation strengths of the six fundamental WGMs to decrease significantly to < 12 dB. In figure 6.7 (c), with excitation arrangement 2 μm-off MBR centre, excitation strengths for both of the fundamental and higher *q*-order WGMs attain almost equal strength, in the range of 5 dB. Coupling the tapered fibre further away from the MBR centre did not change the transmitted spectrum much except for higher loss in the strengths of the excited WGM resonances. In some of the transmitted resonance spectra (i.e. figure 6.7 (d)), noticeable shifts on the resonance wavelengths occurred due to minor MBR refractive index change caused by self-heating of the high resonating power [16] and/or change in the ambient temperature.

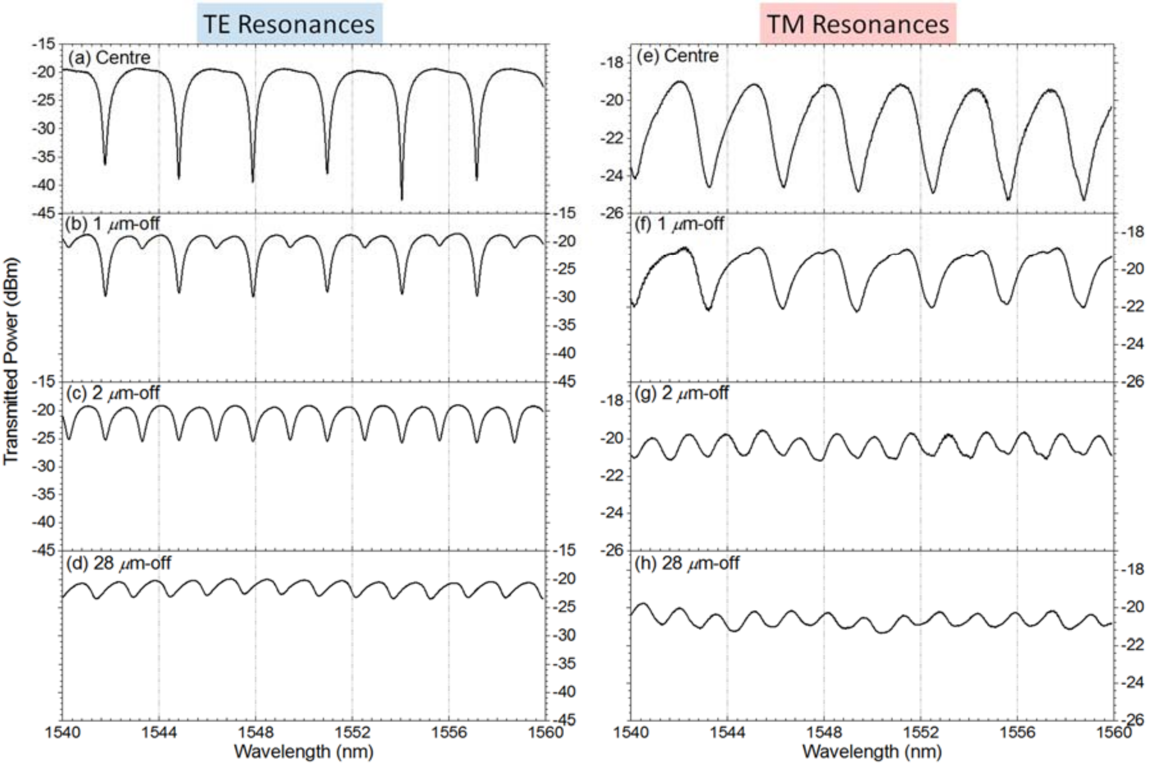

Figure 6.7 Transmitted spectra of plasmonics-MBR WGMs with TE- and TM-polarization input light and tapered fibre excitation arrangement at (a) & (e) centre axial position, (b) & (f) 1 μm-off centre, (c) & (g) 2 μm-off centre, and (d) & (h) 28 μm-off centre.

The same trend was observed with TM-polarized light coupled into the cavity of plasmonics-MBR where the seven distinguishable fundamental WGM transmission dips decreased from 5 dB (figure 6.7 (e)) to 3 dB (figure 6.7 (f)) with the appearance of higher order axial *q*-modes. In figure 6.7 (g), exciting the plasmonics-MBR 2 μm-off centre dramatically decreased the strength of the fundamental modes to ~ 1 dB and they appeared to be almost identical to the higher excited *q*-order modes. Coupling the tapered fibre further away from the centre also did not change the transmitted profile much (i.e. figure 6.7 (h)) except for higher losses and minor WGM resonance wavelength shifts.

6.4 Coupling positions and thin metal-film thickness

In this section, the excitation of the hybrid plasmonics-MBR was studied on various coupling conditions relative to the position of the thin metal-film in order to understand the effect of the gold presence on the excited WGMs. The study was performed by fixing the position of the tapered fibre in the system and rotating the plasmonics-MBR on its *x*-axis. The same experimental set-up as in figure 6.2 (a) was applied with the exception of the tapered fibre utilized, where it was cleaved after the up-taper transition region at its full 125 μm diameter-end, and clamped on top of a rigid mount for practical experimental handling. With the tapered fibre fixed on top a rigid mount, the total experimental set-up system-loss (tapered fibre loss + loss of light through the collimating lens + loss of light in free-space + light coupling loss into MMF + etc..) was first determined. With TE/TM polarized light of -5.0 dBm power launched through the tapered fibre (and without coupling it to any resonator), the recorded data shows a flat transmission profile of -13.6 dBm throughput over the 1540 – 1560 nm wavelength span. For such experimental set-up, the 8.6 dB total system-loss was considered to be acceptable.

The angle of MBR rotation (θ_{MBR}) was controlled by inserting one of the resonator stem through a high-precision fibre-rotator. The fibre rotator was placed on top of an accurate-positioning three-axis stage for precise MBR-tapered fibre excitation arrangement. On each coupling arrangement, the TE- and TM-polarized light was launched through the tapered fibre in order to compare the dielectric and plasmonics WGMs spectra. The hybrid plasmonics-MBR was accurately brought in contact with the 2 μm diameter tapered fibre and coupled to the MBR centre as precisely as possible. Figure 6.8 shows the transmitted spectra of the hybrid plasmonics-MBR coupled with the TE- and TM-polarized input light and at various angles of MBR rotation (θ_{MBR}) relative to the position of the tapered fibre. As could be seen from figure 6.7 (b) & (f), positioning the tapered fibre slightly off the MBR centre even by 1 μm would excite higher order axial modes. For higher precision of *central* plasmonics-MBR excitation arrangement utilizing the tapered optical fibre, the transmitted spectra were monitored so that they would mostly attain fundamental WG family group-modes, as in figure 6.7 (a) & (e). In figure 6.8, four distinguishable WG family group-modes were observed over the 1542 – 1556 nm wavelength span. Schematics of the plasmonic-MBR cross-sections at various angles of MBR rotation (θ_{MBR}) and relative to the position of the tapered fibre are also shown for guidance. However, the schematic cross-sections do not reflect the actual cross-sections of the MBR under test as the fabricated bottle resonator might have some irregularities in its parabolic-profile shape.

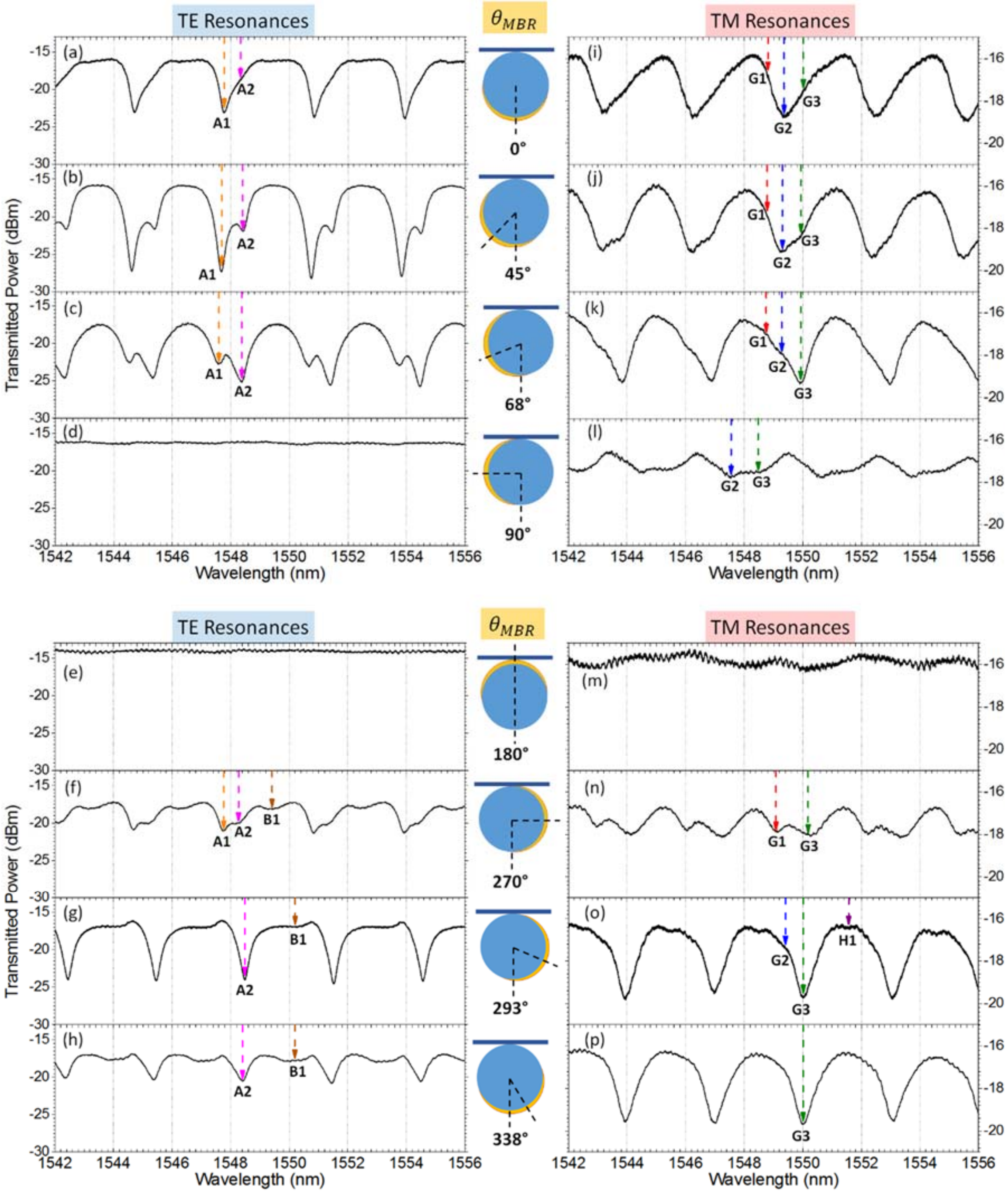

Figure 6.8 TE- and TM-WGM transmitted spectra of the hybrid plasmonics-MBR with various MBR rotation θ_{MBR} and tapered fibre coupling arrangements.

In the TE WGMs transmission spectra, two distinguishable resonances of the same family group-mode, A1 and A2, were monitored at various θ_{MBR} coupling arrangements. Initially, as in figure 6.8 (a), resonance A1 has higher excitation strength than A2 at $\theta_{MBR} = 0°$. The excitation strength of both resonances increased at $\theta_{MBR} = 45°$ (figure 6.8 (b)) with a sharp transmission dip of resonance A1 generated. At $\theta_{MBR} = 68°$, the excitation strength of both resonances dropped with greater resonance A2 excitation than A1. As in figure 6.8 (d), no TE WGM transmission dips were observed when the tapered fibre was coupled near the edge of the meniscus thin metal-film at $\theta_{MBR} = 90°$ and on top of the surface at other θ_{MBR} arrangements. The same situation was observed with $\theta_{MBR} = 180°$, however, throughput power of the recorded spectrum in figure 6.8 (e) was higher (≈ -14 dBm). This indicates that when the tapered fibre is coupled on top of the 40 nm thick-gold section, almost all of the TE launched power passes through the tapered fibre without resonating in the cavity. The TE WGMs were shifted for $\theta_{MBR} = 270°$, as in figure 6.8 (f). Self-heating of the cavity would likely to occur with such high lasing light power evanescently coupled near the thin-metal film. This in turn would slightly change the refractive index of the plasmonics-MBR cavity resulting in a shifted WGM spectrum. Resonance A1 and A2 were poorly excited along with a slight excitation of higher axial order-mode B1 (see figure 6.7 (b)). The resonance B1 was also observed to be slightly excited at $\theta_{MBR} = 293°$ and $338°$. However, as in figure 6.8 (g) and (h), only the fundamental resonance mode A2 was well excited with higher excitation observed through the former coupling arrangement of the two.

Plasmonics-whispering-gallery resonances excited by TM-polarized light also varied in their excitation strengths with different θ_{MBR} coupling arrangements. Three distinguishable resonances of the same family group-mode, G1, G2 and G3 were monitored at various θ_{MBR} coupling arrangements. The resonance G1 was observed to be weakly excited on most of the coupling arrangements through the whole experiment. The resonance G2 was the most highly excited at $\theta_{MBR} = 0°$ and $45°$. However, as shown through figures (i) – (k), the excitation strength of resonance G3 gradually increases with every change in θ_{MBR}. Comparing figure 6.8 (d) & (l), while there was no dielectric TE WGMs excited, the transmitted spectra still attain traces of shifted TM-plasmonics-WGMs under the same coupling arrangement of $\theta_{MBR} = 90°$. Additionally, while most of the TE-polarized light passes through the tapered fibre in figure 6.8 (e) yielding a -14 dBm throughput power, traces of weakly excited plasmonics-WGMs were recorded in figure 6.8 (m) at lower transmitted throughput power of -16 dBm when the tapered fibre was coupled on top of the 30 nm thick-gold. Resonance G1 and G3 were weakly and slightly excited when the tapered fibre was coupled on the other side of the thin metal-film meniscus edge at $\theta_{MBR} = 270°$ (figure 6.8 (n)). As in figure 6.8 (o), at $\theta_{MBR} = 293°$ the higher axial q-order mode H1 (see figure 6.7 (f)) is slightly excited with a weak excitation of resonance G2 and high excitation of resonance G3. Finally, at $\theta_{MBR} = 338°$, the recorded transmitted spectrum only shows a highly excited plasmonics-resonance G3 over the broad wavelength range span.

It can be summarized from the experiments that excitation strengths of individual TE dielectric-resonances and TM plasmonics-resonances in each family group-mode varies with the different tapered fibre excitation arrangement relative to the position of the meniscus thin metal-film. The distinctive SPPs generation demonstrated in this section with the proposed hybrid resonator would be greatly beneficial towards sensing applications meant for high Q-factor plasmonics devices.

6.5 FDTD simulation of hybrid whispering-gallery plasmonics-microdisc resonator with meniscus thin metal-film

For additional insight into the proposed hybrid whispering-gallery plasmonics-MBR, the simulation of a whispering-gallery microresonator with meniscus thin metal-film was performed by utilizing a finite-difference time-domain (FDTD) software package [17]. The simulation was executed in a 2-D environment with smaller component dimensions than the experiment in order to minimize the required memory size and computing run time. A waveguide with 0.7 μm width core was set to be in contact with a microdisc resonator of 7 μm radius for evanescent light coupling. The background refractive index value was set to 1.0 (air) and the waveguide and microdisc refractive index were set to 1.5 (dielectric). Half of the microdisc surface was covered with a meniscus shape thin gold-film of 40 nm maximum thickness. To calculate the transmission spectrum of the hybrid plasmonics structure, a TE-/TM-fundamental mode pulse of Gaussian shape centred at 1.55 μm and 1.0 power (of arbitrary unit) was launched from one end of the waveguide with a power monitor placed on the other. In order to avoid any back-reflections from the computed windows, perfectly-matched layers were set on the boundaries. The microdisc resonator was rotated to different angles θ_{MR} in order to study the effects of various waveguide coupling arrangements relative to the position of the thin gold-film.

Transmission spectra of the simulated hybrid plasmonics-microdisc resonator at various microresonator angle of rotation θ_{MR} are shown in figure 6.9. Two TE-WGM and two TM-WGM resonances denoted by R1 & R2 and S1 & S2, respectively, were monitored with different coupling arrangements. Calculated TE dielectric WGM resonances attained higher *Q*-factor values in the range of 900 with narrow and sharp linewidth transmission dips. On the contrary, TM plasmonics WGM resonances attained broad linewidth transmission dip features with a smaller *Q*-factor value in the range of 150: the same tendency observed as in the experimental data (figure 6.4 and 6.5). Excitation strengths of resonance R1, R2, S1 and S2 varied with different coupling arrangement. In some cases, while one of the two resonances was highly excited, the other only shows small or no excitation over the broad wavelength, as in figure 6.9 (f) for dielectric TE-WGMs with $\theta_{MR} = 113°$, and figure 6.9 (m) for plasmonics TM-WGMs with $\theta_{MR} = 90°$. The same single highly-excited WGM phenomenon was also observed with the plasmonics-MBR experimental study, as shown in figure 6.8 (g) & (p). Additionally, as in the experiment, coupling the waveguide on the metal part of the hybrid microdisc transmits most of the power through the waveguide with weak WGM coupling into the hybrid cavity (figure 6.9 (g) & (o) and (h) & (p)). When the waveguide was placed on top of the section with the thickest gold layer ($\theta_{MR} = 180°$), a similar trend as in the experimental results (figure 6.8 (e) & (m)) could be observed on the simulated results of figure 6.9 (h) & (p) where the

TE transmitted spectrum attained higher throughput power (close to input power value of 1.0) than the TM transmitted spectrum. Due to the perfect symmetry of the simulated plasmonics resonator, the other-half of the hybrid-microdisc transmitted spectra is exactly the same as the transmitted spectra studied in the first-half.

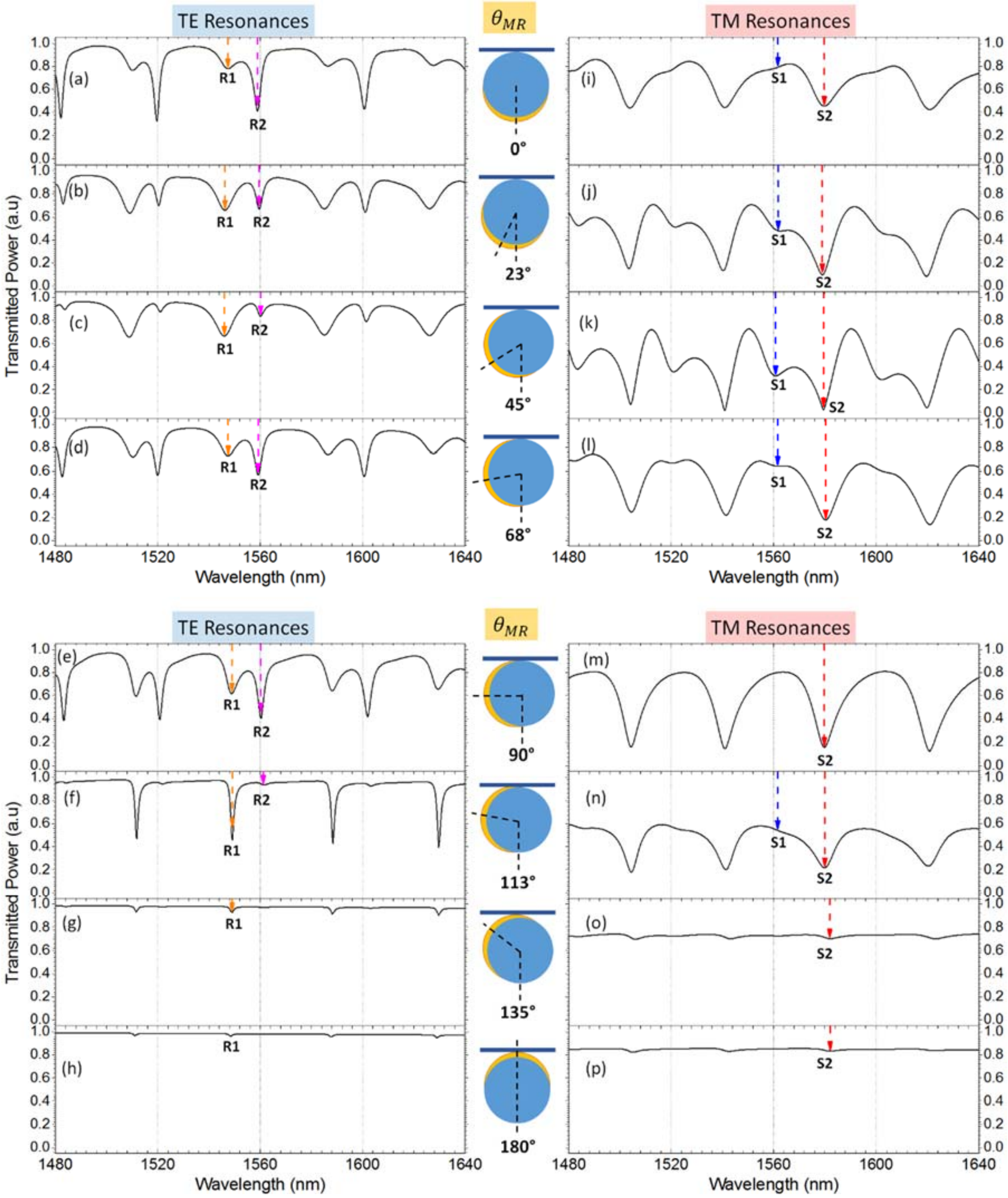

Figure 6.9 TE- and TM-WGM transmitted spectra of the hybrid plasmonics-microdisc resonator with various rotation θ_{MR} and waveguide coupling arrangements.

The steady-state field distribution of the microdisc was simulated with and without meniscus thin gold-film set on the surface of the resonator under TE and TM launched light conditions. Figure 6.10 summarizes the azimuthal m and radial p mode of the dielectric TE transmission dips where the WGMs were excited with their respective cw wavelengths (a) without and (b) with a meniscus thin metal-gold-film. The TE WGMs of the microdisc shifted by 23.5 nm to shorter wavelengths with the presence of the thin gold-film. An example of the wavelength shift is highlighted in the figure with mode number $(m, p) = (37{,}1)$.

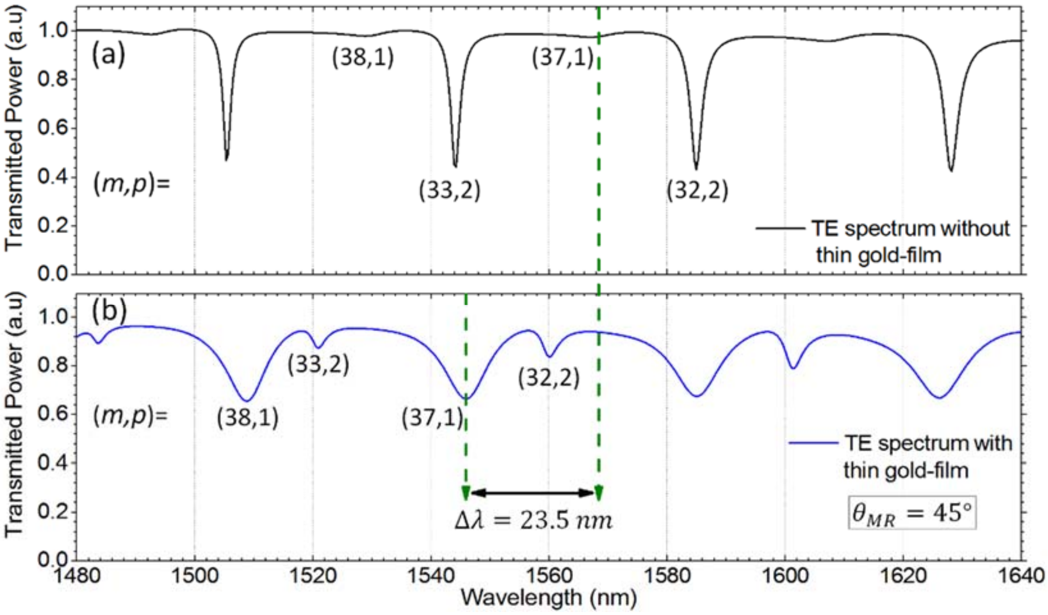

Figure 6.10 TE transmission spectra of the simulated WGM microdisc resonator and their azimuthal and radial mode numbers (m, p) (a) without and (b) with the meniscus thin metal-gold-film.

A plot of the microdisc electric **E**-field steady-state distribution is shown in figure 6.11 (a) at the microresonator angle of rotation $\theta_{MR} = 45°$. The meniscus thin metal-gold-film covers half of the microdisc resonator surface from point arrow-i clockwise to point arrow-ii. Launching TE-polarized cw light centred at 1545.92 nm through the waveguide excites an under-coupled WGM with mode number $(m, p) = (37{,}1)$. No surface plasmon polaritons (SPPs) were generated on the surface of the gold (metal-air interface). The electric field intensity $|\mathbf{E}|^2$ profile near the metal-air interface are shown in figure 6.11 (b) and (c) with a gold-film thickness of 10 nm and 40 nm, respectively. Light was intensely confined in the dielectric (glass) perimeter of the hybrid structure with ~zero intensity on the gold-air medium.

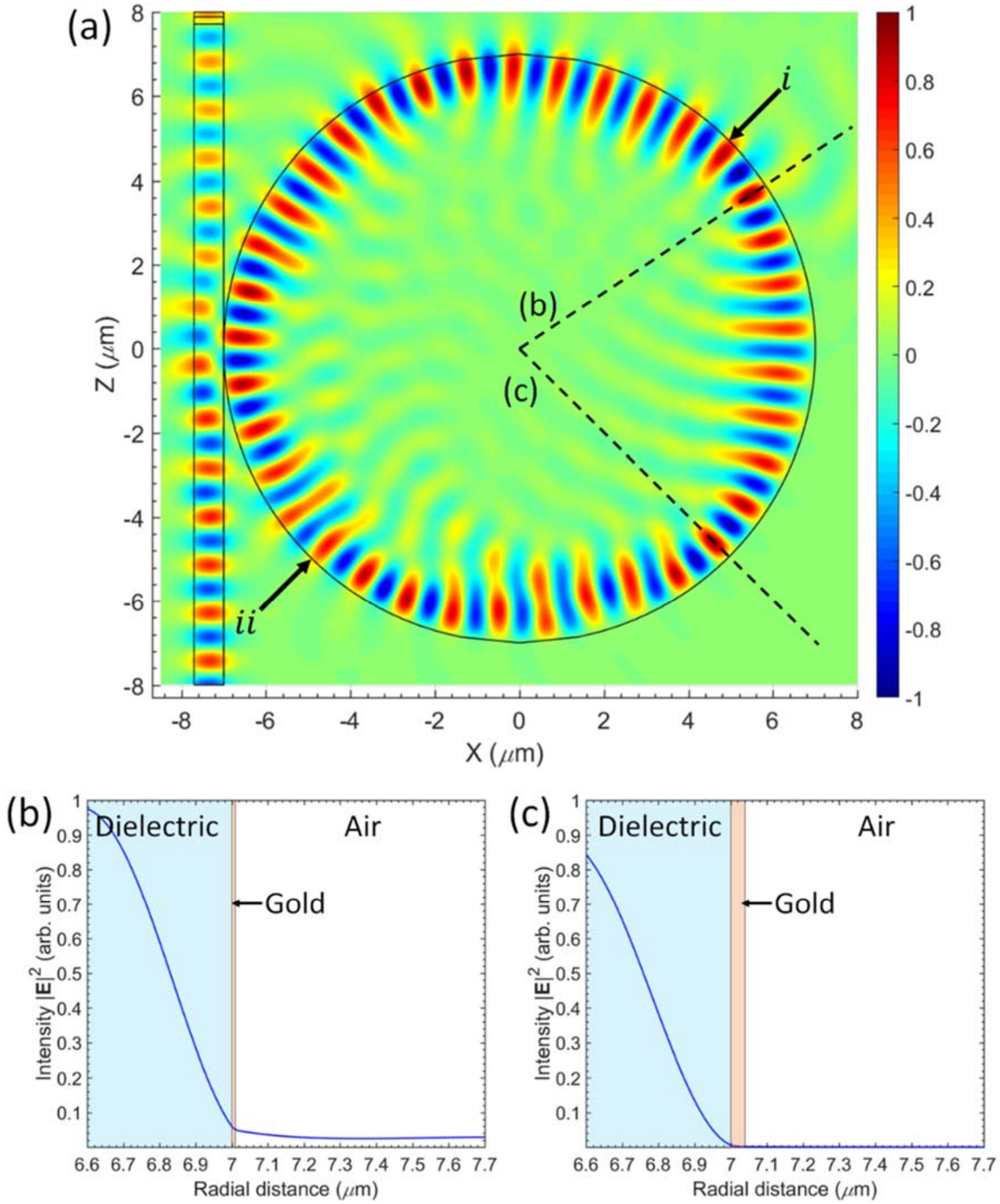

Figure 6.11 (a) $\mathbf{E}$-field steady-state distribution of the simulated hybrid microdisc resonator with microdisc rotation angle $\theta_{MR} = 45°$ and input TE cw light centred at 1545.92 nm. (b) Electric-field intensity $|\mathbf{E}|^2$ profile near the surface of the hybrid microdisc resonator across 10 nm, and (c) 40 nm thick gold.

Figure 6.12 summarizes the azimuthal m and radial p mode of the plasmonics TM transmission dips where the WGMs were excited with their respective cw wavelengths (a) without and (b) with meniscus the thin metal-gold-film. Compared to the TE WGMs, the TM WGMs of the microdisc resonator were shifted greater by more than 40 nm to shorter wavelengths with the presence of the thin gold-film. An example of the wavelength shift is highlighted in the figure with mode number $(m, p) = (36,1)$.

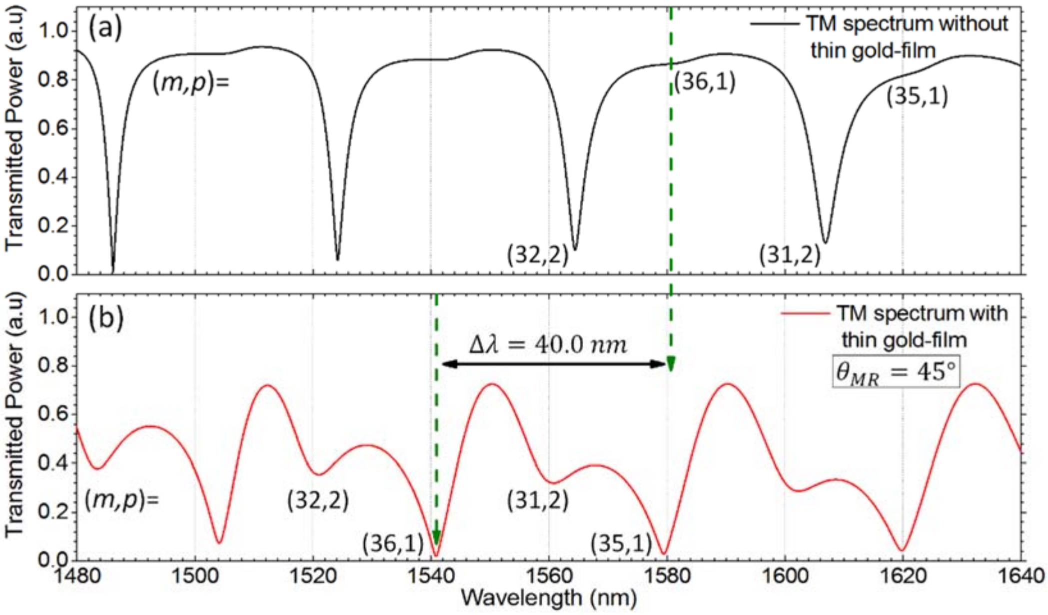

Figure 6.12 TM transmission spectra of the simulated WGM microdisc resonator and their azimuthal and radial mode numbers (m, p) (a) without and (b) with the meniscus thin metal-gold-film.

A plot of the microdisc magnetic **H**-field steady-state distribution is shown in figure 6.13 (a) at the microresonator angle of rotation $\theta_{MR} = 45°$. The meniscus thin metal-gold-film covers half of the microdisc resonator surface from point arrow-i clockwise to point arrow-ii. Critical-coupling of plasmonics WGMs with mode number $(m, p) = (35,1)$ was achieved with launched TM-polarized cw light centred at 1579.52 nm. “Additional” resonance modes were generated on the dielectric (glass)-metal interface, between point arrow-i to point arrow-ii (where thin-gold-film is present), and they “push” the main excited WGMs slightly inward into the microdisc. On the outer perimeter, surface plasmon polaritons (SPPs) were generated on the surface of the gold (metal-air interface). The SPP resonant modes propagated slower on the surface of the gold than the “additional” resonant modes which were confined in the glass-metal interface between point arrow-i to point arrow-ii. Upon the disappearance of the thin metal-film (at point arrow-ii), the “additional” resonant modes vanished and the SPP resonant modes combined back with the main dielectric WGMs. Clockwise from point arrow-ii to point arrow-i, the resonant WGMs were confined near the surface of the microdisc resonator.

Figure 6.13 (b) plots the magnetic field intensity $|\mathbf{H}|^2$ profile across the metal-air interface close to the starting-edge of the meniscus film with 20 nm thick-gold (denoted by black-dashed line (b) in figure 6.13 (a)). The intensity drops to zero inside the gold envelope. On the outer perimeter of the gold envelope, strong plasmonics mode profile decays exponentially into the air. Figure 6.13 (c) shows magnetic field intensity $|\mathbf{H}|^2$ profile across the 40 nm thick gold region (denoted by black-dashed line (c) in figure 6.13 (a)) attained weak plasmon resonant mode on the gold surface.

Nonetheless, as shown in the inset, the magnified plasmonics mode also decays exponentially into the air. From the simulation, it can be summarized that strong SPP resonance modes are generated close to the starting edge of the meniscus thin metal-film. This particular region of the hybrid-WGM structure would be highly advantageous for high-*Q* plasmonics sensing applications.

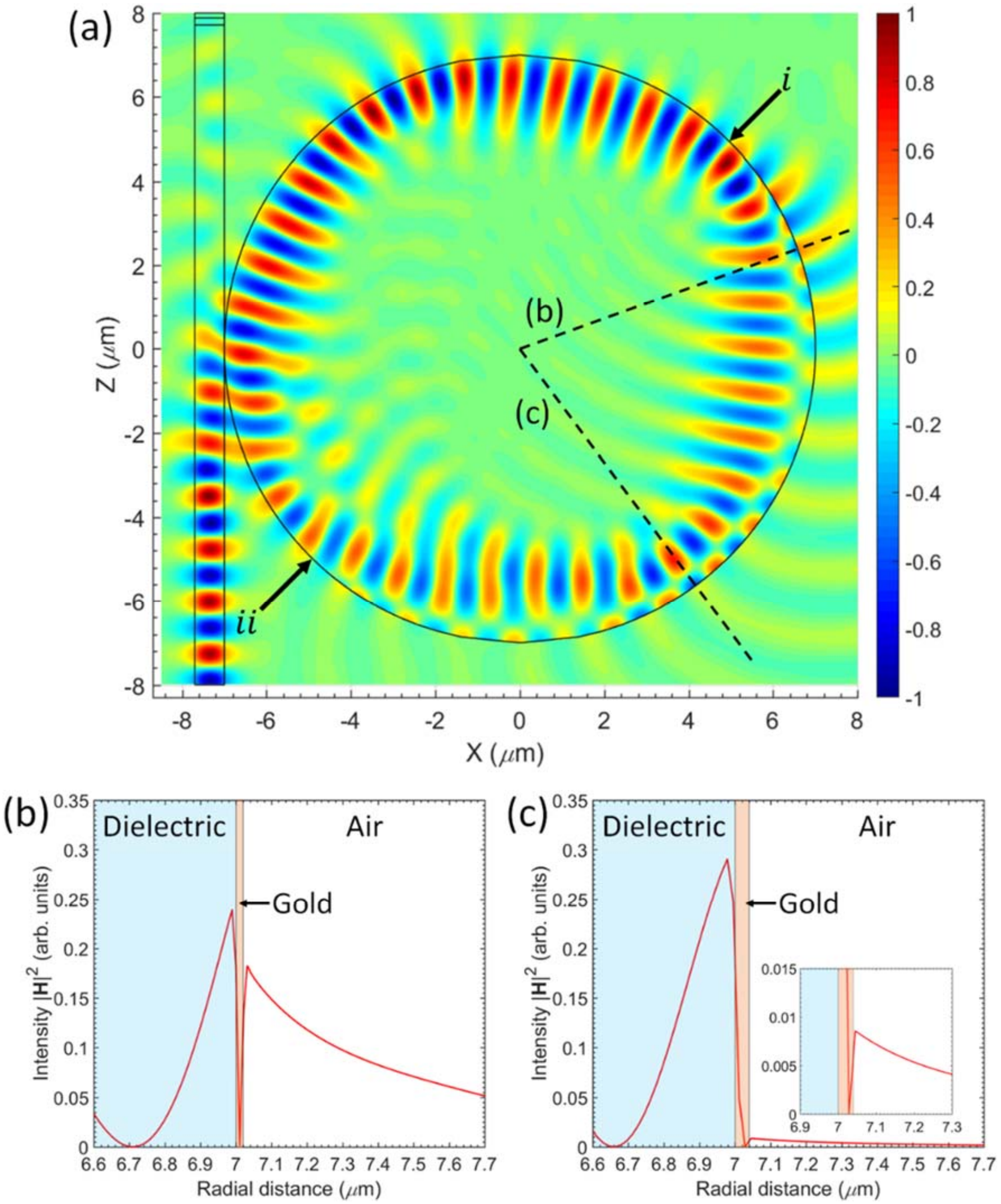

Figure 6.13 (a) **H**-field steady-state distribution of the simulated hybrid microdisc resonator at microdisc rotation angle $\theta_{MR} = 45°$ and input TM cw light centred at 1579.52 nm. (b) Magnetic-field intensity $|\mathbf{H}|^2$ profile near the surface of the hybrid microdisc resonator across 20 nm, and (c) 40 nm thick gold.

6.6 Summary

A hybrid WGM plasmonics-MBR has been successfully demonstrated with the deposition of a meniscus thin metal-gold-film on half of the surface of a standard MBR. TE and TM WGM resonances of the proposed hybrid resonator were studied with the utilization of a polarization-resolved experimental set-up. The calculated Q-factors of the TE and TM transmission dips were in the range of 2100 and 850, respectively. However, Lorentzian fitting performed on the measured data revealed that each TE/TM resonance dips are actually composite resonances comprising two/three partially overlapping WGMs with higher Q-factor values in access of 2900 and 2500, respectively. The excitation strength of each individual resonance mode varies with different tapered fibre coupling arrangement performed relative to the position the meniscus thin metal-gold-film. In some cases, the generation of a single resonance mode (either dielectric or plasmonics) within the family group-mode could be achieved with high excitation strength. This unique feature of the hybrid structure would be highly beneficial for surface plasmon sensing applications.

The FDTD simulation performed on a hybrid WGM plasmonics-microdisc resonator shows a similar trend of selective mode excitation with different waveguide coupling arrangement relative to the position of the meniscus thin gold-film. The generation of a single resonance mode (either dielectric or plasmonics) within a family group-mode is also achievable with certain coupling arrangements. TE transmission spectrum showed a higher throughput power than TM when light was coupled on the thickest gold section, in good agreement with the experimental observations. From the (m, p) mode numbers it was deduced that TM WGM resonances were shifted more than the TE WGM resonances when the meniscus thin metal-film are introduced on the surface of the microdisc. Coupling TM polarized light into the cavity of the hybrid plasmonics-microdisc structure generates “additional” modes along the glass-metal interface with SPP resonant modes being generated on the gold surface. The magnetic field intensity $|\mathbf{H}|^2$ profile of the simulated hybrid structure shows that plasmonics modes with high excitation strength are present close to the starting edge of the meniscus thin metal-film. This would be the particular region of interest should the proposed hybrid-plasmonics WG microresonator be utilized for plasmonics sensing applications.

6.7 References

[1] K. J. Vahala, “Optical microcavities,” *Nature* **424**, 839-846 (2003).

[2] W. L. Barnes, A. Dereux, and T. W. Ebbesen, “Surface plasmon subwavelength optics,” *Nature* **424**, 824-830 (2003).

[3] R. M. Cole, Y. Sugawara, J. J. Baumberg, S. Mahajan, M. Abdelsalam, and P. N. Bartlett, “Easily Coupled Whispering Gallery Plasmons in Dielectric Nanospheres Embedded in Gold Films,” *Physical Review Letters* **97**, 137401 (2006).

[4] M. A. Noginov, G. Zhu, A. M. Belgrave, R. Bakker, V. M. Shalaev, E. E. Narimanov, S. Stout, E. Herz, T. Suteewong, and U. Wiesner, “Demonstration of a spaser-based nanolaser,” *Nature* **460**, 1110-1112 (2009).

[5] M. P. Nezhad, A. Simic, O. Bondarenko, B. Slutsky, A. Mizrahi, L. Feng, V. Lomakin, and Y. Fainman, “Room-temperature subwavelength metallo-dielectric lasers,” *Nature* **4**, 395-399 (2010).

[6] B. Min, E. Ostby, V. Sorger, E. Ulin-Avila, L. Yang, X. Zhang, and K. Vahala, “High-*Q* surface-plasmon-polariton whispering-gallery microcavity,” *Nature* **457**, 455-458 (2008).

[7] Y-F. Xiao, C.-L. Zou, B.-B. Li, Y. Li, C.-H. Dong, Z.-F. Han, Q. Gong, “High-Q exterior whispering gallery modes in a metal-coated microresonator,” *Physical Review Letters* **105**, 153902 (2010).

[8] X. Zhang, Z. Ma, H. Yu, X. Guo, Y. Ma, and L. Tong, “Plasmonic resonance of whispering gallery modes in an Au cylinder,” *Optics Express* **19**, 3902–3907 (2011).

[9] M. A. Santiago-Cordoba, S. V. Boriskina, F. Vollmer, and M. C. Demirel, “Nanoparticle-based protein detection by optical shift of a resonant microcavity,” *Applied Physics Letters* **99**, 073701 (2011).

[10] A. Rottler, M. Harland, M. Bröll, M. Klingbeil, J. Ehlermann, and S. Mendach, “High-*Q* Hybrid Plasmon-Photon Modes in a Bottle Resonator Realized with a Silver-Coated Glass Fiber with a Varying Diameter,” *Physical Review Letters* **111**, 253901 (2013).

[11] G. S. Murugan, J. S. Wilkinson, and M. N. Zervas, "Selective excitation of whispering gallery modes in a novel bottle microresonator," *Optics Express* **17**, 11916-11925 (2009).

[12] M. Sumetsky, “Whispering-gallery-bottle-microcavities: the three dimensional etalon,” *Optics Letters* **29**, 8-10 (2004).

[13] G. S. Murugan, M. N. Petrovich, Y. Jung, J. S. Wilkinson, and M. N. Zervas, “Hollow-bottle optical microresonators,” *Optics Express* **19**, 20773-20784 (2011).

[14] J. C. Knight, G. Cheung, F. Jacques, and T. A. Birks, “Phase-matched excitation of whispering-gallery-mode resonances by a fiber taper,” *Optics Letters* **22**, 1129-1131 (1997).

[15] Y. Jung, G. Brambilla, and D. J. Richardson, "Polarization-maintaining optical microfiber," Optics Letters **35**, 2034-2036 (2010).

[16] T. Carmon, L. Yang, and K. J. Vahala, "Dynamical thermal behavior and thermal self-stability of microcavities," *Optics Express* **12**, 4742-4750 (2004).

[17] R Soft Design Group, Rsoft Inc., FullWAVE 6.0 (2008).

Chapter 7: Broadly tuneable solid microbottle resonator

7.1 Introduction

The nature of high *Q*-factor optical microresonators in confining light through whispering-gallery modes (WGMs) has shown significant applications in advanced photonics systems [1]. One of the many interesting features of optical microresonators includes their capability being made tuneable by some alteration to their physical system. For example, dielectric WGM microresonators could change in shape when being exposed to various surrounding conditions. This results in the change of the resonating light optical path length and could be observed through the resonance wavelength shift. By changing a microresonator surrounding temperature, WGM resonance shifts could be tuned to lower or higher wavelengths. Such tuning method had been tested on microspheres [2,3] and microtoroid resonators [4]. Another method reported in literature for tuning WGM resonances is through pressure control. The same concept applied where the change of pressure would change the shape of the microresonator under test. This could be done either by changing the external [5] or internal [6] pressure of the microresonators. Even though such techniques are beneficial to be applied towards highly sensitive optical sensing devices, it is still not preferable to be applied for WGM resonance tuning due to the limited accessible tuning range and complex structure required in controlling the temperature and pressure variations. Furthermore, certain area of studies, such as cavity-QED, would only benefit from a broad tuneable high-*Q* WGM resonances as strong optical coupling is required at specific wavelengths [1,7].

For broader ranges of WGM resonance tunability, great performances have been reported through mechanical tuning. Although mechanical tuning by squeezing a WGM microsphere is possible [8], it is much more practical to tune any whispering-gallery microresonator through strain as it provides a more robust and precise tuning mechanism. WGM strain tuning has been demonstrated on microcylinders [9] and microspheres [10] by pulling their two stems. Dense and complex WGM resonance strain tuning on spheroidal-shape dielectric resonator has shown a record tunability of ~ 2.2 free spectral ranges (FSRs) (~ 5.5 nm tuning range) on a microbubble resonator where its hollow structure enables maximizing the strain in the direction of the applied force [11]. To date, even though *solid* spheroidal WGM structure studied on microbottle resonators (MBRs) were calculated to attain tunability of a few FSRs [12], no such tuning performance has ever been reported. With the unique feature to selectively excite different axial WGM resonances on MBRs [13,14], it was proposed instead that resonance tuning to an arbitrary wavelength could be achieved by strain-tuning the near axial bottle mode [15].

In this chapter, the demonstration of a strain-tuneable solid WGM MBRs with high *Q*-factor values and simple spectral feature will be presented. Full FSR tunability could be performed to the excited WGM resonances without the need of selective axial mode excitation. For the purpose of mechanical tuning and strain sensing, it is desirable that the optical microresonator under test has an easily integratable robust structure, easily identifiable clean resonance spectra with high *Q*-factors, high coupling strengths, fixed polarization and broad tuning range to facilitate wavelength-shift monitoring. MBRs provide two stems on either side of the microresonator and offer themselves naturally for easy integration and mechanical tuning [12-15]. Previously mechanically-tuned WGM microresonators have not shown all the aforementioned attributes in a single monolithic design due to limitations in either their intrinsic performance and/or coupling efficiency [9,10]. In this chapter, demonstration of a highly robust monolithic MBRs with high *Q*-factor for WGM resonance tuning and optical strain sensing purposes are presented. Section 7.2 discusses the proposed MBR fabrication steps and the strain-tuning polarization-resolved experimental set-up utilized. Section 7.3 shows the transmitted WGMs spectral “clean-up” technique on the MBRs under test. In section 7.4, strain-tuning results of the “cleaned-up” TE- and TM-WGMs spectra are presented.

7.2 Fabrication of microbottle resonators and strain-polarization-resolved experimental set-up

The solid MBRs utilized for the strain-tuning experiment were fabricated by using commercial single mode fibres (SMFs) with 125 μm outer-diameter. The protective polymer coating on the SMFs were first removed with a mechanical fibre stripper and the fibres were cleaved with a high precision optical fibre cleaver. With the utilization of a semi-automatic fusion splicer, precise fibre alignment to control the parabolic profile on the SMF could be achieved. Since variation of fibre radius in the nano-scale is proficient enough for a quantum well to occur and trap excited WGMs [16], mode degeneracies would be broken in a highly spheroidal MBR resulting to a dense and complex WGM transmission spectra [13,14]. In order to minimize the number of supported WGMs, the MBRs fabricated in this study were fabricated with a relatively small bottle diameter. This was achieved by slightly increasing the overlap of two fibres (SMFs) during the arc-fusion process. Figure 7.1 shows the fabricated MBR imaged under polarized white light with (a) parallel and (b) orthogonal conditions. Maximum bottle diameter and length of the MBR were ~ 128 μm and ~ 500 μm, respectively.

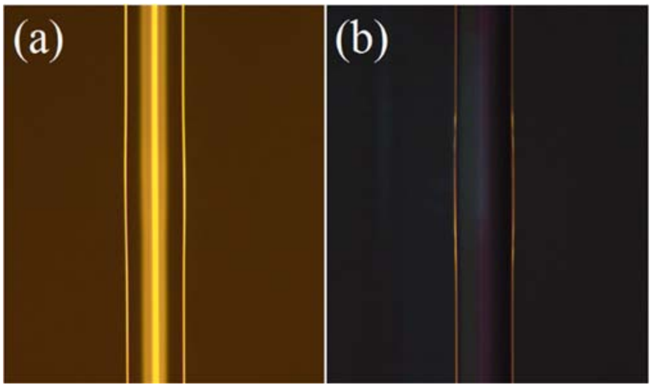

Figure 7.1 MBR imaged with polarized white light under (a) TE and (b) TM conditions.

To date, the study of TE- and TM-excited WGMs to applied strain had only been reported with the utilization of coupling prisms [9,10]. As higher coupling efficiencies could be achieved with the utilization of optical tapered fibres [17], a straightforward method to proficiently discriminate between excited TE- and TM-WGMs under strain was applied. A polarization resolved set-up as in figure 4.9 (discussed in section 4.4) was utilized for the strain-tuning experiment. In order to minimize any birefringence effect that may influence the polarization-resolved measurement, the tapered fibre was kept straight from the MBR coupling point up to the fibre cleaved point. The efficiency of the polarization-resolved system in discriminating TE and TM transmitted light was characterized to be > 20 dB, comparable to a polarization-maintaining optical microfiber [18].

7.3 Microbottle resonator spectral clean-up

As discussed in section 3.2, spectral “clean-up” of MBRs could be achieved through the utilization of optical tapered fibres with various waist diameters D_t. The same is also true should the resonator under test be coupled at different positions along the tapering region of a tapered fibre. Figure 7.2 shows (a) – (e) TE WGMs, and (f) – (j) TM WGMs resonance spectra of the MBR under test when excited at MBR centre position and various positions along the tapered fibre. Figure 7.2 (a) & (e) shows the transmitted when the MBR was coupled at $D_t = 2\ \mu m$. Even with a relatively small parabolic MBR profile, dense and complex WGM resonance spectra were observed when the micro-resonator was excited from the tapered fibre waist region. To “clean-up” and simplify the dense MBR spectrum, the MBR was evanescently coupled on the up-taper region instead with an approximated D_t of (b) & (f) 6 μm, (c) & (g) 8 μm, and (d) & (h) 10 μm. Progressively sparser and simpler WGM resonance spectra with reduced coupling efficiencies were generated when the MBR was coupled at larger diameter tapers.

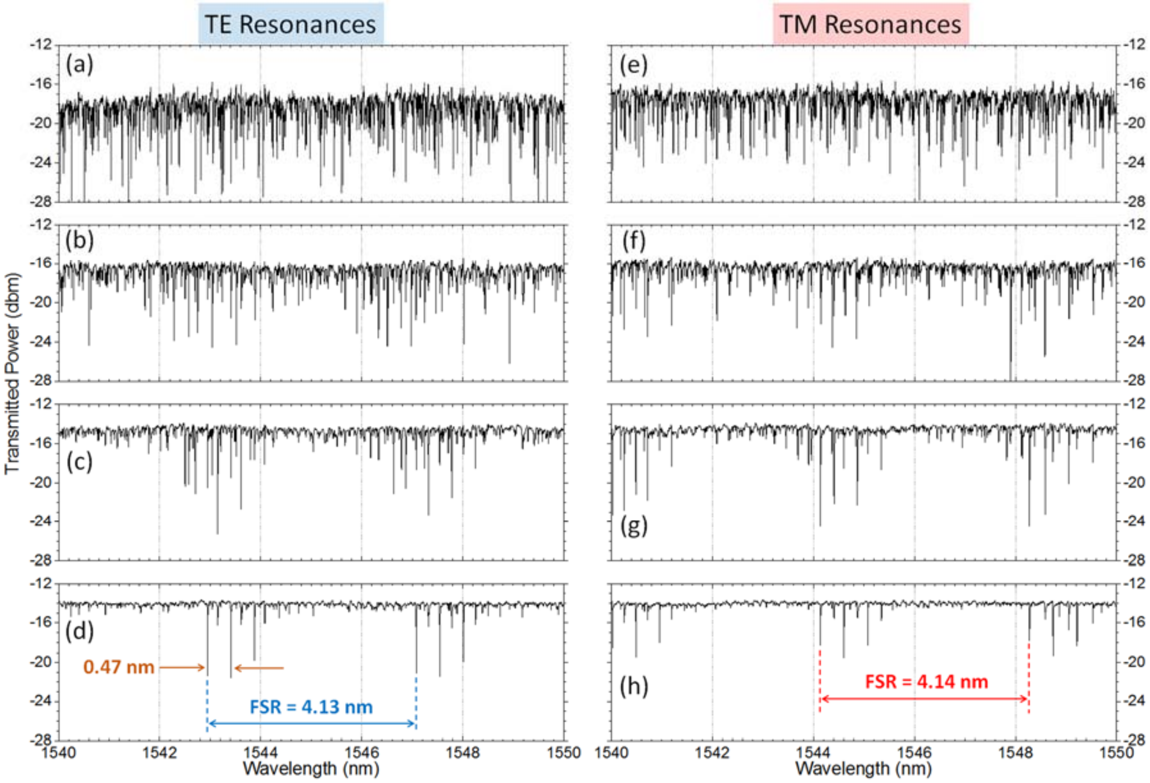

Figure 7.2 Transmitted TE and TM MBR-WGMs excited at different fibre tapering region of various D_t.

Figure 7.3 (a) shows the calculated effective indices for the TE WGMs supported by an MBR with dimensions equal to the experimentally fabricated ones. In the case of $D_t = 2\ \mu m$, the microtaper mode is strongly overlapping and phase matched with WGM families characterized by radial mode number $p = 1 \rightarrow 4$. This results in the strong excitation of multiple radial-order WGM families and a dense transmission spectrum [19]. On the contrary, in the case of $D_t = 10\ \mu m$, the microtaper mode shows reduced overlap and is mismatched with all WGM families. As a result, the transmission spectrum is weaker and much simpler, as it depends entirely on the excitation of WGMs with radial mode number $p = 1$. The resonances are strongest around $\lambda = 1544\ \mathrm{nm}$ (azimuthal mode number $m = 364$, axial mode number $p = 1 \rightarrow 4$) and $\lambda = 1548\ \mathrm{nm}$ ($m = 363$, $p = 1 \rightarrow 4$), in close agreement with the experimentally measured data. The calculated azimuthal and axial FSR are 4.1 nm and 0.45 nm, respectively, in close agreement with the experimental values (see figure 7.2 (d)).

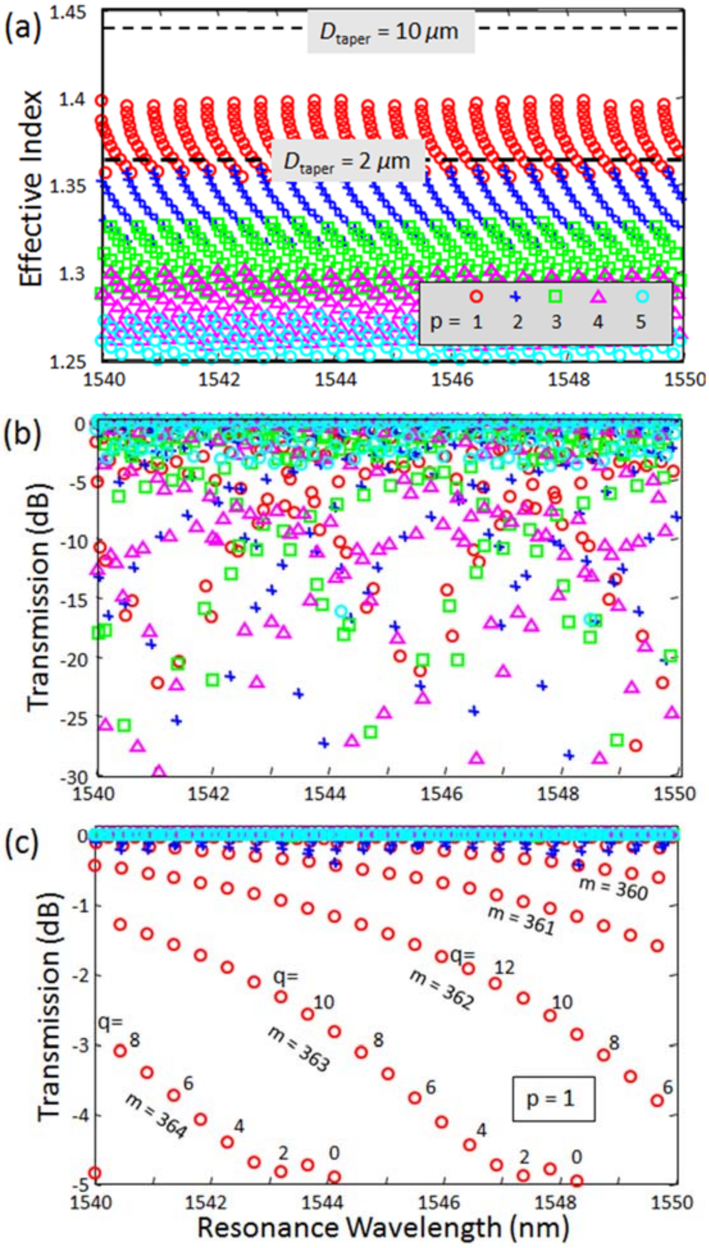

Figure 7.3 (a) Calculated MBR WGM and microtaper effective indices. Calculated transmission spectra with microtaper diameter (b) 2 μm and (c) 10 μm.

To calculate the MBR Q-factor value ($Q = \lambda/\Delta\lambda$), Lorentzian fittings were performed on the measured transmitted data in order to distinguish individual resonances among the composite overlapping excited modes. For accurate Lorentzian fittings, it is crucial that the cumulative-fitted peak trails the measured data over the selected fitting wavelength range. Figure 7.4 shows Lorentzian fitting and Q-factor values of two strongest coupled TM-excited resonances (red lines) over 1.2 nm wavelength span with a coupling arrangement of $D_t = 10\ \mu m$ (as in figure 7.2 (h)). Even with very strong coupling conditions introduced by the tapered fibre in direct physical contact to the MBR, the calculated Q-factor value of the microcavity reaches 10^5. Such tapered fibre arrangement also yields relatively high coupling efficiencies with ~ 77% achieved for TE resonances and ~ 68% for TM resonances.

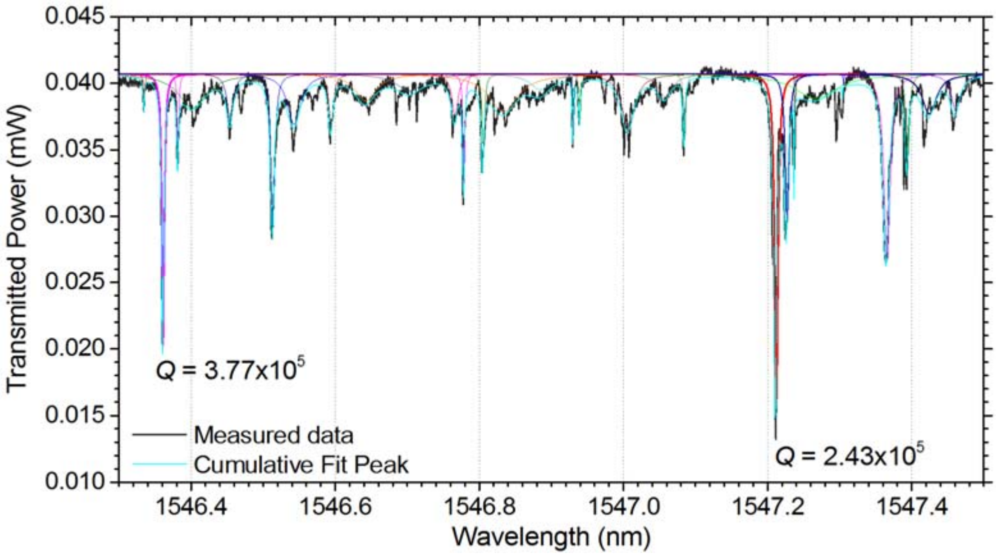

Figure 7.4 Measured TM transmission of the MBR excited at the centre with tapered fibre coupling arrangement $D_t = 10\,\mu m$ (black line), Lorentzian fittings with Q-factor values of the two strongest excited WGMs (red lines), and cumulative fit peak of all of the Lorentzian fittings (light blue line).

7.4 Strain-tuning of microbottle resonator whispering-gallery modes

To stretch the MBR with high precision, one of its stem was glued with epoxy on top of a fixed v-grooved fibre-holder stage. The other stem was glued on top of a high-resolution linear translation stage for the stretching procedure to commence. The linear stage was precisely withdrawn away from the fixed end at constant increment. Stretching results in the MBR diameter reduction (defined by the Poisson ratio) and refractive change (due to stress-optic effect). The former is polarization insensitive, while the latter depends on polarization [9,10]. As strain is an anisotropy process, forced elongation along the optical fibre/MBR would result in different index change towards the fibre/MBR axial and lateral directions. The combined effect results in different blue-shifts for the TE- and TM-polarized MBR WGM resonances. Tapered fibre with coupling arrangement as in figure 7.2 (d) & (h) were selected for strain-tuning experiment.

7.4.1 MBR1 whispering-gallery modes resonance strain-tuning

For MBR1, the two glued points on the resonator stems L were 0.8 cm apart. Figure 7.5 illustrates the wavelength shift vs. the applied strain $(\varepsilon = \Delta L/L)$ of MBR1 TE-WGM centered at ~ 1549.7 nm and TM-WGM centered at ~ 1547.2 nm. Since the linear translation stage utilized was manually controlled, no electrical feedback was available to monitor the exact displacement-position of the translation stage cross-roller-bearing. In situations where the cross-roller-bearing encountered an unspecific amount of backlash, the monitored-trace WGM would be observed as a slip; resulting in the MBR-WGM resonance shift to be not perfectly linear. At a strain of 25 mϵ, the traced TE-WGM resonance shifted by 2.18 nm. However, the traced TM-WGM resonance was observed to shift by 3.71 nm, corresponding to ~ 0.9 FSR. The calculated slope ratio of the TM-TE wavelength shift is 1.67, a close approximation to a perfect microcylinder TM-TE wavelength shift ratio of 1.75 [9,10].

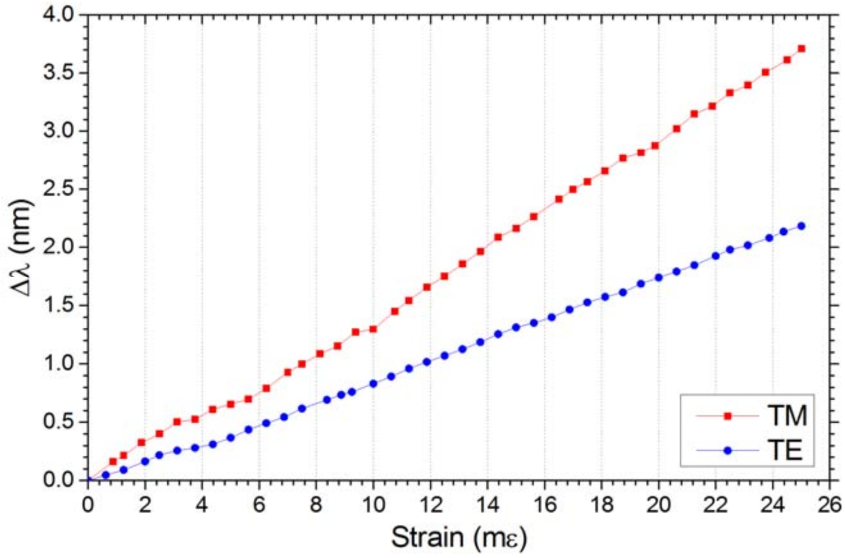

Figure 7.5 Summary of MBR1 TE and TM wavelength shift vs. applied strain.

Figure 7.6 shows the actual transmitted measured data of MBR1 TE- and TM-WGMs with various amount of applied strain. Since the change in refractive index are larger for TM polarization in a strained optical WGM microresonator (due to stress-optic effect) [9, 10], MBR1 TM-WGMs were shifted more with the same amount of strain applied than TE-WGMs. With the “cleaned-up” spectra, the highly-excited WGMs were easily distinguishable and traced over the broad wavelength range.

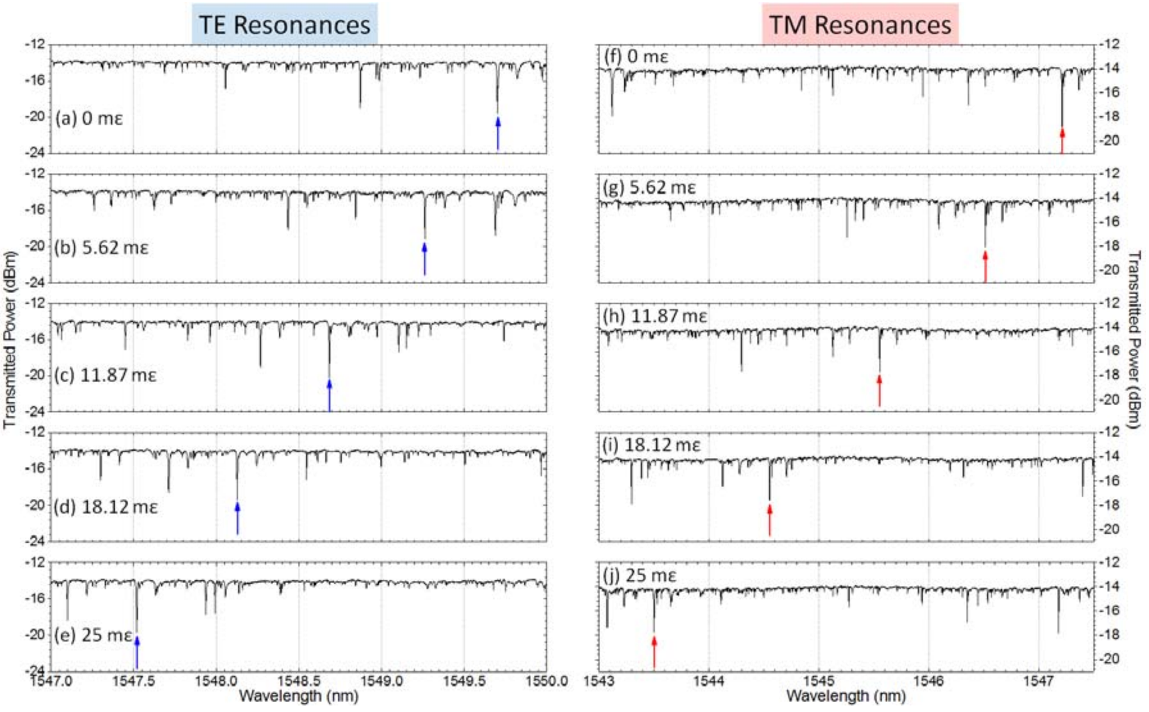

Figure 7.6 MBR1 TE- and TM-WGM wavelength resonance shift with various applied strain.

7.4.2 MBR2 whispering-gallery modes resonance strain-tuning

A destructive strain-tuning test was performed on another bottle resonator, MBR2, with the same polarization-resolved experimental set-up. To prevent the primary MBR micro-stretching, the protective polymer coating of the fibre utilized was removed with a chemical stripper instead of a mechanical fibre stripper, prior to the fusion-splicing process. The two MBR stems were glued 1.1 cm apart on a fixed v-grooved fibre-holder and on the linear translation stage. Only TM-polarized light was coupled into the MBR cavity in order to see the maximum achievable tuning range before the fibre fractures/breaks. Figure 7.7 summarizes the wavelength shift of MBR2 TM-WGMs centred at ~ 1547.1 nm with various applied strains. Despite clear signs of fibre slippage, a maximum tuning range of ~ 4.1 nm could be achieved corresponding to full FSR tunability; the highest demonstrated on a high-*Q* *solid*-glass optical microresontor structure. Straining the MBR further resulted in fracture on one of the resonator stems.

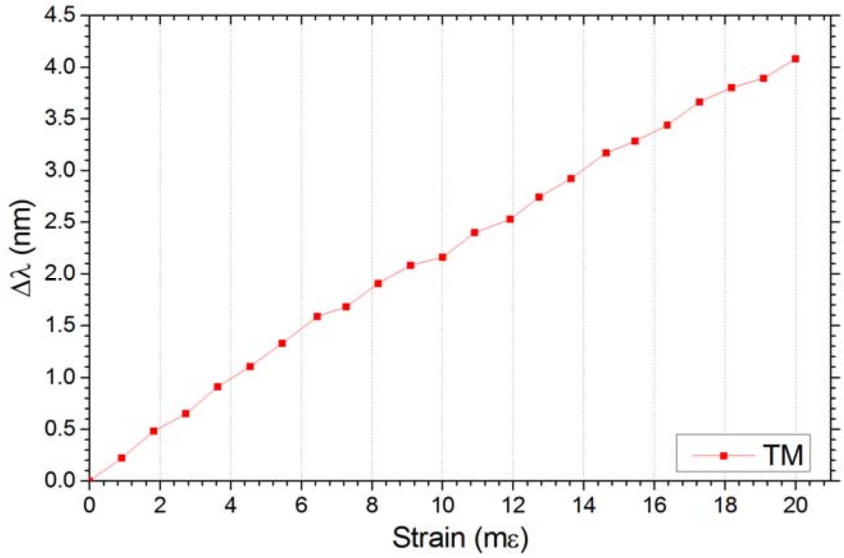

Figure 7.7 Summary of MBR2 TM-WGMs full FSR tunability wavelength shift vs. applied strain.

Figure 7.8 shows the transmitted spectra of the traced TM-WGM resonance wavelength shift with various applied strains. The simple and cleaned-up MBR spectrum is of great advantage for the wavelength shift monitoring process should the MBR be utilized as an optical strain sensor. Additionally, high excitations of the WGMs achieved by tapered fibre evanescent coupling is advantageous in tracing a single WGM along the whole FSR without the need to cautiously rely on another in the event of weak power couplings [20].

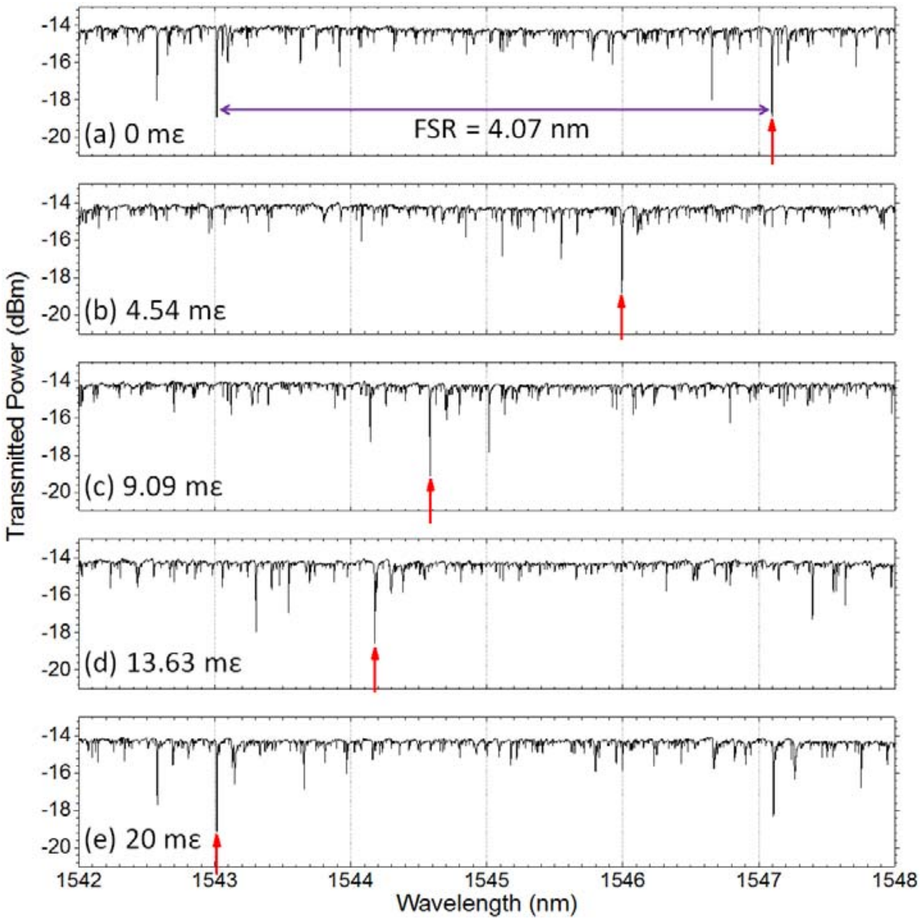

Figure 7.8 MBR2 TM-WGM wavelength resonance shift with various applied strain.

7.5 Summary

A highly tuneable WGM MBR has been successfully demonstrated by slightly overlapping two standard optical fibres during an arc-fusion-splicing process. The solid MBRs are not only simple to fabricate, but also attain a highly robust structure with high *Q*-factors reaching 10^5. Simplification to the dense and complex MBR spectral feature was established by efficiently exciting the WGMs via the up-taper region of an optical tapered fibre. TE- and TM-WGM resonance shifts corresponding to applied mechanical strain were investigated for the first time with the utilization of tapered optical fibres. Polarization resolved measurements have resulted in a TM-WGM shift over an entire FSR and a TM-/TE-WGM resonance shift ratio of 1.67. The demonstrated high mechanical tunability of the MBR-WGM resonances (≥ FSR) is greatly beneficial towards specific WGM excitation for cavity-QED studies and optical strain sensor applications.

7.6 References

[1] K. J. Vahala, "Optical microcavities," *Nature* **424**, 839-846 (2003).

[2] Q. Ma, T. Rossmann, and Z. Guo, "Whispering-gallery mode silica microsensors for cryogenic to room temperature measurement," *Measurement Science and Technology* **21**, 025310 (2010).

[3] A. Chiba, H. Fujiwara, J. -I. Hotta, S. Takeuchi, and K. Sasaki, "Resonant Frequency Control of a Microspherical Cavity by Temperature Adjustment," *Japanese Journal of Applied Physics* **43**, 6138-6141 (2004).

[4] D. Armani, B. Min, A. Martin and K. J. Vahala, "Electrical thermo-optic tuning of ultrahigh-*Q* microtoroid resonators," *Applied Physics Lett*ers **85**, 5439-5441 (2004).

[5] T. Ioppolo and M. V. Ötügen, "Pressure tuning of whispering gallery mode resonators," *Journal of Optical Society America B* **24**, 2721-2726 (2007).

[6] R. Henze, T. Seifert, J. Ward, and O. Benson, "Tuning whispering gallery modes using internal aerostatic pressure," *Optics Letters* **36**, 4536-4538 (2011).

[7] R. v. Klitzing, R. Long, V. S. Ilchenko, J. Hare, and V. Lefèvre-Seguin, "Tunable whispering gallery modes for spectroscopy and CQED experiments," *New Journal of Physics* **31**, 14.1-14.4 (2001).

[8] T. Ioppolo, M. K., V. Stepaniuk, M. V. Ötügen, and V. Sheverev, "Micro-optical force sensor concept based on whispering gallery mode resonators," *Applied Optics* **47**, 3009-3014 (2008).

[9] A. L. Huston and J. D. Eversole, "Strain-sensitive elastic scattering from cylinders," *Optics Letters* **18**, 1104-1106 (1993).

[10] W. von Klitzing, R. Long, V. S. Ilchenko, J. Hare, and V. Lefèvre-Seguin, "Frequency tuning of the whispering-gallery modes of silica microspheres for cavity quantum electrodynamics and spectroscopy," *Optics Letters* **26**, 166-168 (2001).

[11] M. Sumetsky, Y. Dulashko, and R. S. Windeler, "Super free spectral range tunable optical microbubble resonator," *Optics Letters* **35**, 1866-1868 (2010).

[12] Y. Louyer, D. Meschede, and A. Rauschenbeutel, "Tunable whispering-gallery-mode resonators for cavity quantum electrodynamics," *Physical Review A* **72**, 031801 (2005).

[13] M. Sumetsky, "Whispering-gallery-bottle-microcavities: the three dimensional etalon," *Optics Letters* **29**, 8-10 (2004).

[14] G. S. Murugan, J. S. Wilkinson, and M. N. Zervas, "Selective excitation of whispering gallery modes in a novel bottle microresonator," *Optics Express* **17**, 11916-11925 (2009).

[15] M. Pöllinger, D. O'Shea, F. Warken, and A. Rauschenbeutel, "Ultrahigh-*Q* Tunable Whispering-Gallery-Mode Microresonator," *Physical Review Letters* **103**, 053901 (2009).

[16] M. Sumetsky and J. M. Fini, "Surface nanoscale axial photonics," *Optics Express* **19**, 26470-26485 (2011).

[17] J. C. Knight, G. Cheung, F. Jacques, and T. A. Birks, "Phase-matched excitation of whispering-gallery-mode resonances by a fiber taper," *Optics Letters* **22**, 1129-1131 (1997).

[18] Y. Jung, G. Brambilla, and D. J. Richardson, "Polarization-maintaining optical microfiber," Optics Letters **35**, 2034-2036 (2010).

[19] M. N. Zervas, "Transmission resonance modelling in microbottle resonators," manuscript under preparation.

[20] R. Madugani, Y. Yang, J. M. Ward, J. D. Riordan, S. Coppola, V. Vespini, S. Grilli, A. Finizio, P. Ferraro, and S. N. Chormaic, "Terahertz tuning of whispering gallery modes in a PDMS stand-alone, stretchable microsphere," *Optics Letters* **37**, 4762-4764 (2012).

Chapter 8: Conclusion and future work

8.1 Conclusion

WGM optical microresonators have great potential for a wide range of applications as they are able to confine light in small volumes with low loss and high *Q*-factors. MBRs have also attracted much attention recently because of their straightforward fabrication method, easy handling and 3D light confinement. The work presented in this thesis, focused on the development of WGM MBRs for advanced sensing applications, is split broadly into two main parts. The first part of this thesis focused on simplifying the dense and complex spectral features of MBRs that includes the manipulation of the excitation source, micro-scars inscription on MBRs, and precise polarization measurement of WGM microresonators. The second part covers the performance of MBRs for applications towards a plasmonics sensor and strain sensor/tuneable optical WGM source.

Chapter 3 presents a systematic study on the effects of the microtaper diameter (D_t) on the MBR transmission characteristics. Increasing D_t from 2 μm to 10 μm yields progressively cleaner and simpler WGM transmission spectra while retaining *Q*-factor values in access of 10^6. With relatively larger microtaper waist diameters utilized (> 6 μm), simpler WGM spectra were generated with increased transmission power due to excitation of lower-radial-order modes at the cost of reduced transmission strength. Mode transformation of light coupling from MBR back to microtaper were also studied experimentally by monitoring near-field images transmitted from the microtaper output end. Conversion of the LP_{01} microtaper fibre mode into LP_{11} were observed to commence on a number of strong transmission resonances in the case of 2 μm taper waist diameter. Modal transformation was observed to be not as frequent in the case of the microtaper with 8 μm waist diameter despite that it supports much larger modality. Based on developed calculations, it was understood that modal phase-matching between WGMs and microtaper LP modes are the ones that actually defines the degree of modal transformations in an evanescently coupled microresonator, rather than the number of LP modes supported by a microtaper. FDTD simulations carried out on a microdisc resonator also show a similar energy back-transfer trend to the waveguide across a strong WGM resonance. As a result, there is no major concern of coupling losses in utilizing microtaper with higher D_t for MBR spectral “clean-up” (since any power coupled to higher LP modes would be lost in the cladding during a microtaper transition back to SMFs). The simpler “cleaned-up” WGMs feature would be beneficial as indication markers should MBRs be used in sensing applications where tracing a specific WGM is required over a broad wavelength span.

In chapter 4, another method to simplify the dense and complex spectral transmission features of MBR WGMs was demonstrated by inscribing periodic micro-scars on the surface of MBRs through focused ion-beam milling. MBR1 was inscribed with 11 periodic micro-scars along its axial path and MBR2 was inscribed with 21 micro-scars along its azimuthal path in order to attenuate most of the excited modes. High *Q*-factors in access of 10^5 were also preserved by the MBRs even after the milling process. By utilizing a highly discriminating polarization resolved set-up, MBRs excited TE-/TM-WGMs and their resonance FSR were able to be clearly distinguished. Additionally, when the input light polarization tuned to 45°, the excited TE- and TM-WGMs throughput transmission could be filtered out of the optical system with equal power. The excitation arrangement near both of the MBRs neck with TE input polarization yields a highly excited and distinguishable WGM resonance dip over a broad spectral wavelength range. FDTD simulations performed on a microdisc with periodic micro-scars provides an additional insight to this unique phenomenon where, in some cases, the resonating modes are capable to beat together in order to circumvent the defect introduced by the micro-scars, resulting in a distinguishable and high-*Q* resonance confined near the surface of the WGM microresonator. The highly distinguishable resonance transmission dips by both of the “scarred”-MBRs are advantageous to be utilized as markers in WGM sensing applications.

As optical microresonators exhibit distinctive families of TE- and TM-polarized WGM resonances, each resonance type, strength and number are affected by the polarization state of the evanescently-coupled input light. Chapter 5 discussed experimental and theoretical analysis on the evolution of transmission dips, polarization cross-coupling (PXC) and scattered light in WGM microresonators as the input light polarization is changed under a polarimetric set-up. Four different types of optical microresonators were studied, which are an optical microsphere, cylindrical microresonator, milled microresonator and a “scarred”-MBR. Under detailed observation, it was shown that transmission dip and the PXC minima shifted with respect to the ideally expected input polarization angle. A theoretical model developed based on Jones matrix calculus attributed the observed shifts to the residual birefringence of the output part of the micro-taper fibre. Based on experimental work, the birefringence could have originated from microtaper twisting and/or pressure applied to the tapered fibre (due to clamping) after the coupling point. The theoretical model also demonstrates that since the light scattered-out of the microresonators are not affected by this residual birefringence, it is therefore a better metric to be monitored for accurate TE or TM polarization launching. Another observation made was microresonators with tighter axial power confinement, such as MBRs and micro-milled resonators, show larger cross-polarization coupling efficiencies, hence should be preferred as polarization converters. The lack of axial mode confinement in cylindrical microresonators results in the smallest and almost polarization independent cross-polarization coupling. The polarization-resolved experiment demonstrated in this chapter is an important reference for future optical microresonator work, especially those involving highly-discriminating and precise polarization measurement.

Chapter 6 reports the performance of MBR in supporting a hybrid WGM plasmonics cavity. A thin layer of gold-film was deposited on the surface of the MBR in order to excite surface plasmon polaritons (SPPs). The thin metal-film covers half of MBR's surface with a meniscus profile with 30 nm maximum thickness and created appropriately tapered edges on the two sides of the MBR. It facilitated to a low-loss adiabatic transformation of the MBR-WGMs to SPPs, and vice versa. The calculated Q-factor value of dielectric-TE and plasmonics-TM transmission dips were in the range of 2100 and 850, respectively. The performed Lorentzian fitting revealed that each TE/TM WGM resonance dip is actually composite resonances comprising of two/three partially overlapping WGMs with higher Q-factor values in access of 2900 (dielectric) and 2500 (plasmonics), respectively. Detailed measurements were taken with various tapered fibre coupling arrangements relative to the position of the meniscus thin metal-film by rotating the MBR. Excitation strengths of individual resonances from the same family-group mode varied with different coupling arrangement sets. In some arrangements, it is also possible to generate a single dielectric/plasmonics resonance of a family group-mode along with high excitation strength while supressing the others. The same trend was observed with FDTD simulation performed on a hybrid plasmonics microdisc with varying gold-film thickness of a meniscus profile and of 40 nm maximum thickness. Excitation strengths of the simulated WGMs varied with different coupling arrangements of the hybrid plasmonics-structure. Additionally, as in experimental observations, coupling the waveguide on the point with thickest gold does not transfer much power into the hybrid-cavity. Instead, most of the input power just transmitted through the waveguide, with TE-polarized light transmitting more than TM. Based on the simulated azimuthal and radial mode numbers (m, p), it was deduced that TM WGM resonances were shifted greater than TE resonances with the introduction of the meniscus thin metal-film on the surface of the microdisc. The microdisc's steady-state magnetic field $\mathbf{H}$ distribution showed that "additional" modes were generated along the glass-metal interface (where the meniscus thin-metal film is present) when TM-polarized light was coupled into the microcavity of the hybrid structure. At the same time, SPP resonant modes were generated on the surface of the gold. The unique feature of various WGM-plasmonics excitation strength with the proposed meniscus thin metal-film hybrid structure would be greatly beneficial for surface plasmon sensing applications. Additionally, from the simulated magnetic field intensity $|\mathbf{H}|^2$ profile, strong plasmonics excitation which decays exponentially into the air are generated close to the starting edge of the meniscus thin metal-film. This would be the particular region of interest to be exploited for surface plasmon sensing for any hybrid WGM-plasmonics microcavity structure incorporating a meniscus thin metal-film profile.

Finally, in chapter 7, demonstration of highly tuneable WGM MBRs which utilize a solid structure is presented. The MBRs were fabricated by slightly overlapping two standard optical fibres during an arc-fusion-splicing process. The dense and complex spectral feature of MBR WGMs were simplified by efficiently coupling the cavity on the up-taper region of an optical tapered fibre. Even though the technique overloads the cavity and reduces the resonator's overall *Q*-factor value, accurate Lorentzian fitting performed on the measured data revealed that the fabricated MBRs still support high *Q*-factor values in the range of 10^5. Simplification of the dense MBR WGMs transmission features and the incorporation of a highly discriminating polarization-resolved set-up enables TE- and TM-excited modes to be clearly distinguished for WGM tuning study. TE- and TM-WGM resonance shifts corresponding to applied mechanical strain were investigated for the first time with the utilization of optical tapered fibres. Polarization-resolved measurements on the fabricated MBRs yield TM-/TE-WGM resonance shift ratio of 1.67. Destructive strain-tuning test performed on one of the fabricated MBRs resulted in TM-WGM shift of over an entire FSR (~ 4.1 nm), the highest ever demonstrated on a *solid* WGM microresonator structure. The proposed MBRs attain highly robust structure, easily identifiable resonance spectra and high coupling strengths all in a single monolithic design. The demonstrated high mechanical tunability of the MBR WGMs (≥ FSR) with high *Q*-factors would not only be beneficial for strain-sensing applications, but also practical to be applied in cavity-QED studies.

8.2 Future work

Microbottle resonators (MBRs) have shown great performances as a high-*Q* WGM optical resonator. For better MBRs performance, different size and shape of micro-scars inscribed on its surface can be explored. For sensing purposes, survival of a single WGM with high-*Q* and excitation strength would be desirable for broad wavelength-shift tracing. The performance of the proposed hybrid plasmonics-MBR should also be further explored primarily on its precision on surface-plasmon sensing. Additionally, various dimension of MBRs along with different thickness/types of noble metal (i.e. silver) and coupling arrangement can be optimized for best performance of surface plasmon sensing. Succeeding to the proposed highly tuneable MBR by mechanical strain, spectral MBR WGM tuning is also possible for other types of mechanically induced refractive index change. A good example for another type of MBR WGM tuning is by mechanical twist. The applied twist to the MBR can slightly change its cavity dimension, and produce stress induced birefringence which in turn would change its refractive index value. This would be of great advantage for an all-fibre twist sensing applications.

Following the work presented in this thesis, it would be very useful for the proposed MBRs to be packaged in a robust design which allows protection and easy handling of the resonators. As refractive index of WGM optical microresonators would slightly change with heat (internal and/or external factor), packaging would also allow the MBRs to be utilized as a temperature sensor. With high requirements of single-device applications nowadays, research work towards MBRs on-chip integration should also be considered. This would involve fabrication of a low-loss waveguides which can evanescently couple light into the cavity of MBRs with high efficiency. On-chip integration would also require optimization on the design of the waveguide to practically support the MBRs so that external factors which could affect the performance of the MBRs (such as vibration, pressure, etc.) would be minimized.

List of publications

Journals

1. **Mohd Narizee Mohd Nasir**, G. Senthil Murugan, and Michalis N. Zervas, “Spectral cleaning and output modal transformation in whispering-gallery-mode microresonators,” *Journal of the Optical Society America B* **33**, 1963-1970 (2016).

Conferences

1. **M. N. Mohd Nasir**, M. Ding, G. S. Murugan, and M. N. Zervas, “Microtaper fibre excitation effects in bottle microresonators,” *Proceedings of the SPIE* **8600**, 860020, Photonics West, San Francisco, California (2013).
2. **M. N. Mohd Nasir**, M. Ding, G. S. Murugan, and M. N. Zervas, “High-*Q* plasmonics microbottle resonators,” *Proceedings of the SPIE* **8960**, 8600M, Photonics West, San Francisco, California (2014).
3. **M. N. Mohd Nasir**, M. Ding, G. S. Murugan, and M. N. Zervas, “Microgrooved bottle microresonators,” *Conference on Lasers and Electro Optics (CLEO)*, paper STU3M.1, San Jose, California (2014).
4. **M. N. Mohd Nasir**, S. B. Gorajoobi, G. S. Murugan, and M. N. Zervas, “Polarisation effects in optical microresonators,” *2015 IEEE Photonics Conference (IPC)*, Reston, Virginia, 365-366 (2015).
5. **M. N. Mohd Nasir**, G. S. Murugan, and M. N. Zervas, “Broadly tunable solid microbottle resonator,” *accepted to 2016 IEEE Photonics Conference (IPC)*, Waikoloa, Hawaii (2016).